2018

SURFACE FUNCTIONALIZATION VIA PHOTOINITIATED RADICAL POLYMERIZATION FOR RARE CELL ISOLATION AND MECHANICAL PROTECTION

Calvin Frank Cahall
University of Kentucky, calvin.cahall@uky.edu
Author ORCID Identifier:
https://orcid.org/0000-0001-7558-4221
Digital Object Identifier: https://doi.org/10.13023/etd.2018.512

STUDENT AGREEMENT:

I represent that my thesis or dissertation and abstract are my original work. Proper attribution has been given to all outside sources. I understand that I am solely responsible for obtaining any needed copyright permissions. I have obtained needed written permission statement(s) from the owner(s) of each third-party copyrighted matter to be included in my work, allowing electronic distribution (if such use is not permitted by the fair use doctrine) which will be submitted to UKnowledge as Additional File.

I hereby grant to The University of Kentucky and its agents the irrevocable, non-exclusive, and royalty-free license to archive and make accessible my work in whole or in part in all forms of media, now or hereafter known. I agree that the document mentioned above may be made available immediately for worldwide access unless an embargo applies.

I retain all other ownership rights to the copyright of my work. I also retain the right to use in future works (such as articles or books) all or part of my work. I understand that I am free to register the copyright to my work.

REVIEW, APPROVAL AND ACCEPTANCE

The document mentioned above has been reviewed and accepted by the student's advisor, on behalf of the advisory committee, and by the Director of Graduate Studies (DGS), on behalf of the program; we verify that this is the final, approved version of the student's thesis including all changes required by the advisory committee. The undersigned agree to abide by the statements above.

Calvin Frank Cahall, Student

Dr. Bradley J. Berron, Major Professor

Dr. Stephen Rankin, Director of Graduate Studies

SURFACE FUNCTIONALIZATION VIA PHOTOINITIATED RADICAL POLYMERIZATION FOR RARE CELL ISOLATION AND MECHANICAL PROTECTION

DISSERTATION

A dissertation submitted in partial fulfillment of the
requirements for the degree of Doctor of Philosophy in the
College of Engineering
at the University of Kentucky

By

Calvin F Cahall

Lexington, Kentucky

Director: Dr. Bradley J. Berron, Professor of Chemical Engineering

Lexington, Kentucky

2018

https://orcid.org/0000-0001-7558-4221

ABSTRACT OF DISSERTATION

SURFACE FUNCTIONALIZATION VIA PHOTOINITIATED RADICAL POLYMERIZATION FOR RARE CELL ISOLATION AND MECHANICAL PROTECTION

Surface functionalization of living cells for cell therapeutics has gained substantial momentum in the last two decades. From encapsulating islets of Langerhans, to cell laden gels for tissue scaffolds, to individual cell encapsulation in thin hydrogels, to surface adhesives and inert surface camouflage, modification of living cell surfaces has a wide array of important applications. Here we use hydrogel encapsulation of individual cells as a mode of protection from mechanical forces for high throughput cell printing, and chemical stimuli for the isolation of rare cells in blood.

In the first study, we review methods of surface functionalization and establish a metric of potential target biomarkers for circulating tumor cell (CTC) isolation. For extended applications in cancer detection through a fluid biopsy, common surface antigen densities were quantitatively assessed in relation to peripheral blood mononuclear cells (PBMCs) for potential targets of cell specific encapsulation. We then look to commercialization of our process after considering biopsy volumes and cell therapy dose sizes. Undesired batch-to-batch variation in our in-house synthesized photo-initiator could be eliminated by the use of fluorescein, a commercial fluorochrome of similar initiating power to our current eosin initiating system. Fluorescence and hydrogel generation were compared indicating a fluorescein conjugate has comparable power to that of our in-house conjugated eosin. Parameters involving the number of cells and fluid volumes processed were then analyzed systematically. Key parameters were studied to determine optimal equipment and protocol for clinically relevant batch sizes. The final study looks at the mechanical protection provided by thin hydrogel encapsulation. With growing interests in 3D bioprinting and goals of viable whole organ printing for transplant, high resolution and high throughput printing is a growing need. 3D bioprinting presents intense mechanical stimuli in the process that cells must endure. Here we analyze how hydrogel encapsulation reinforces the cellular membrane allowing cells to withstand the damaging forces associated with bioprinting.

KEYWORDS: cell encapsulation, bioprinting, photopolymerization, surface polymerization, isolation.

Calvin Frank Cahall

11/01/2018

Date

SURFACE FUNCTIONALIZATION VIA PHOTOINITIATED RADICAL POLYMERIZATION FOR RARE CELL ISOLATION AND MECHANICAL PROTECTION

By
Calvin Frank Cahall

Dr. Bradley J. Berron
Director of Dissertation

Dr. Stephen Rankin
Director of Graduate Studies

11/01/2018
Date

DEDICATION

To Leslie, Roland, and Clinton Cahall, who have supported me in every way possible to help me get to where I am today. Their love and support through my educational career have been amazing and I could not have done it without them.

ACKNOWLEDGEMENTS

I would first like to thank my advisor, Dr. Brad Berron for being a great mentor and excellent motivator. His passion for science is contagious and it has been a pleasure working for him the past few years. I would also like to thank Dr. Ahmed Abdel-Latif for serving as a co-mentor to me in the Halcomb Fellowship in Medicine and Engineering. His insights from a clinician point of view proved extremely valuable. Finally, I would like to thank Dr. Zach Hilt, Dr. Thomas Dziubla, Dr. Ahmed Abdel-Latif, and Dr. Robert Yokel for being a part of my dissertation committee and outside examiner, respectively.

For out of lab matters and logistical assistance I would like to give a special thanks to Marlene Spurlock. She is an extremely hardworking woman and was always very willing to help with any matters.

Lastly, I want to thank my friends and family for all of their support. My parents, Leslie and Roland Cahall, my brother Clinton Cahall and his wife Bekah, my girlfriend Rebecca Garrison, and countless others that have helped me along the way. Your support means the world to me and I am very greatful.

TABLE OF CONTENTS

LIST OF TABLES

LIST OF FIGURES

LIST OF ABREVIATIONS

AC	Acryloyl Chloride
ASL	Antigen specific lysis
bBSA	Biotinylated bovine serum albumin
BSA	Bovine serum albumin
CTC	Circulating tumor cell
DCM	Dichloromethane
DIW	Deionized water
DMEM	Dulbeco's modified eagle medium
DMSO	Dimethyl sulfoxide
ECM	Extracellular matrix
EGFR	Epidermal growth factor receptor
EITC	Eosin-5-isothicyanate
EL	Elongation
EMT	Epithelial to mesenchymal transition
EpCAM	Epithelial cellular adhesion molecule
ER	Estrogen receptor
EthD-1	Ethidium homodimer-1
FACS	Fluorescent activeated cell sorting
FBS	Fetal Bovine Serum
FITC	Fluorescein isothiocyanate
FSC	Forward scatter
gelMA	Gelatin methacryloyl
HER-2	Human epidermal growth factor receptor-2
ICAM1	Intercellular adhesion molecule-1
IgG	Immunoglobulin
LED	Light emitting diode
MACS	Magnetic activated cell sorting

MNBC	Mononuclear blood cell
MTT	3-(4,5-dimethylthiazol-2-ly)-2,5-diphenyltetrazolium bromide
NHS	N-hydroxy-succinimide
OPTN	Organ Procurement and Transplantation Network
PBA	Polymerization based amplification
PBS	Phosphate buffered saline
PBSA	PBS supplemented with BSA
PE	Phycoerythrin
PEG	Polyethylene glycol
PEGDA	Polyethylene glycol diacrylate
PEGMA	Polyethylene glycol monoacrylate
PBMC	Peripheral blood mononuclear cell
PR	Progesterone receptor
RBC	Red blood cell
RPMI	Roswell Park Memorial Institute medium
SA	Streptavidin
SDS	Sodium dodecyl sulfate
SSC	Side scatter
TA	Triethylamine
TEA	Triethanolamine
TEMPO	(2,2,6,6-tetramethyl-1-piperidinyl)oxy
TX	Triton X-100
UTS	Ultimate tensile strength
VP	Vinyl pyrrolidinone

CHAPTER 1. INTRODUCTION

1.1 Introduction

Cell surface modifications are on the forefront in engineering in medicine because of the numerous applications and potential benefits they enable. The surface engineering of living cells is being applied in fields that range from drug delivery for specific diseases, to immuno-camouflage for transplantations and transfusions, to cyto-protection from chemical and mechanical insults. These modifications are achieved through a number of pathways depending on the desired goal or application. Pathways include covalent coupling, electrostatic interactions, antibody/antigen binding, hydrophobic insertion, enzymatic reactions and more. Each of these pathways possess advantages and disadvantages that may be better suited for a specific application over another. For example, hydrophobic insertion is a technique that is fast and has the ability to insert a large abundance of desired fluorochromes or functional groups to the cell surface. However, this technique lacks the specificity that may be desired when dealing with a heterogeneous population or when trying to isolate a specific cell phenotype.

Specificity is especially important in applications of viable cell sorting. The two most common methods of isolation are magnetic activated cell sorting (MACS) and fluorescent activated cell sorting (FACS). Both of these methods rely on surface binding of phenotypic antigens to distinguish target cells from the rest of the population. MACS uses magnetic micro beads functionalized with antibodies to bind with target cells. The population is then subjected to a magnetic field in which bound target cells are retained while antigen negative cells pass freely through the field. FACS is similar in its antibody specificity but instead uses fluorochromes. With the help of flow cytometry, cells are

analyzed individually for a specified fluorescence channel intensity to determine antigen positive events from negative events. These methods are both limited by the abundance of the target antibodies at the cell surface. MACS binding must be strong enough to immobilize target cells while allowing negative cells to pass through. FACS must bind sufficient fluorochromes to amplify fluorescent intensity much beyond that of autofluorescence and non-specific adsorption. Low availability of target surface antigens greatly decreases the sensitivity of these sorting techniques. While magnetic sorting has the ability of high cell throughput, it is accompanied with relatively poor isolation purity when compared to FACS and requires moderately expensive reagents (biorecognition magnetic beads). Isolation purity is very high for FACS, but at a cost of slow processing and very expensive equipment. High purity isolation with fast processing time and inexpensive equipment is greatly needed.

Our lab has developed a novel surface modification strategy in which cells are able to be individually encapsulated in a thin hydrogel using visible light photoinitiated free radical polymerization for high purity and high throughput isolation with common laboratory materials. Hydrogel encapsulation is achieved through the immobilization of a photoinitiator on the surface of living cells through antigen/antibody recognition. In the presence of 530 nm initiating light, local polymerization occurs near the surface of target cells encompassing them in a thin hydrogel while leaving non-target cells unaltered. This hydrogel acts as a protective barrier to chemical and mechanical stimuli allowing this technology to have a wide array of applications including cell isolation, or membrane reinforcement for high throughput cell printing. This technology has the specificity of antibody/antigen binding with high throughput processing making it a powerful tool in a

clinical setting. The system is very easily adapted to fit nearly any desired specification. Immobilization of the photoinitiator on the surface of the cell can be achieved by antigen/antibody binding, covalent coupling, or hydrophobic insertion making this a very versatile technique. Polymer properties are also easily modified to obtain very specific mechanical properties of the encapsulating hydrogel. Biodegradable moieties, degradation kinetics, and modulus are all very easily adjusted within this system.

Here, multiple applications of individual cell encapsulation are evaluated, including rare cell isolation for early cancer detection of circulating tumor cells, and mechanical protection for high resolution 3D bioprinting. We first review the current methods of cell surface modification and highlight the major applications of each technique as well as the potential disadvantages of each within our applications. Then, we looked into isolation of the highly sought after and rarely occurring circulating tumor cells (CTCs) for the potential of a fluid biopsy for cancer screening. Major challenges of isolating viable and functional CTCs are addressed, while also quantifying surface antigens of common cancer cell lines to find potential targets for isolation strategies. Commonly, surface biomarkers are either reported as positive/negative, as upregulated or downregulated expression levels. With the most common types of cell sorting methods relying on surface expression levels of phenotypic biomarkers, we quantify known metastatic markers in more translatable units of molecules/μm^2, and fold over mononuclear blood cells (MNBCs) as opposed to 'high or low' as commonly reported. As detection of CTCs would depend on distinguishability of positive events from whole blood, markers must be chosen appropriately as to limit staining of MNBCs.

For the greatest efficacy in clinical applications, processing must be highly standardized and of sufficient scale to handle the volumes of blood and number of cells in such a fluid biopsy. To address the standardization of the polymerization process, we look to commercially available fluorescein. Fluorescein isothiocyanate (FITC) is a commonly used fluorochrome that is found commercially conjugated to a wide array of biorecognition molecules. Fluorescein belongs to the same family of xanthene dyes as the currently used initiator, eosin-5-isothiocyantate (EITC). We assess the potential polymerization power of using FITC vs EITC in both cellular studies as well as hydrogel film generation on micro array slides which model the cell surface. In order to ensure that this technology can handle the necessary volumes and cell numbers associated with clinical applications, we systematically analyze each parameter associated with the polymerization process. Parameters such as fluid volume/depth, variation in observed light intensity, chamber material, meniscus effects, and more were studied to determine what aspects of the process play the largest roles. This data may allow us to scale the process one to two orders of magnitude to very feasibly handle the fluid volumes associated with a fluid biopsy.

We assess different applications of this same technology. Individual cell encapsulation provides membrane reinforcement protecting the cell from mechanical stimuli associated with fluid flow similar to that observed in high resolution 3D printing. With ultimate goals of printing viable organs for transplantation, high print rates are necessary to print on a feasible time scale while single cell resolutions are key to incorporating vasculature for sustainable viability. Pairing these two requirements drastically increases the shear forces observed with fluid flow through a pipe which can mechanically lyse cells hindering the viability of a printed structure. We study a range of

monomer formulations that result in polymer coatings that have vastly different mechanical properties. Coated and uncoated cells are subject to intense mechanical forces as they are extruded through a 50 μm diameter capillary at flow rates well above what is currently used in 3D bioprinting. We then correlate the protection potential of each of these polymer coatings with the observed mechanical properties of bulk hydrogels as well as the viability of cells upon extrusion. In the growing field of regenerative medicine, protection from inherent mechanical stimuli during the printing process is invaluable.

The wide range of applications and standardized processing of single cell encapsulation makes this technology highly desired. Adaptation of the monomer coating for controlled biodegradation, or enhanced surface functionalization of the outer coating ensures that this technology is dynamic to the needs of future applications as the world of engineering and medicine evolve around us.

CHAPTER 2. BACKGROUND

2.1 Protection

Interest in cell surface modification primarily began in the 1980s with focus on harnessing pancreatic islets and their function for treating diabetes[1-3]. In cell therapeutics like islet transplantation, as well as any sort of allo- or xenographic transplant, immune response is a major concern. Upon injection of foreign cells, immune response of the host can eliminate injected cells through antibody recognition and macrophage recruitment which limits the efficacy of such treatments. T-lymphocytes or T-cells play a major role in cell-mediated immune response of foreign tissue through the recognition of major histocompatibility complex molecules found on the surface of nucleated cells. Currently, treatments to minimize host rejection are through drug mediated T-cell suppression. These drugs have major drawbacks including numerous side effects and chronic toxicity. As a physical alternative to immuno-suppressive drugs, research is being conducted in immunoisolation or immunocamouflage to accomplish similar goals [4, 5]. This concept was reported early on with the observation of continued functionality with polymer protected pancreatic islets [1, 2]. Modification or encapsulation of cells within a relatively bioinert material can protect the cells from a host immune response [5]. Polymeric networks with tuned mesh sizes can sterically prohibit large molecule permeability, such as antibodies, while still allowing small molecules such as oxygen and glucose to pass freely [1, 3, 6]. This allows the cells to remain viable and function normally while remaining hidden from natural immune responses of the host [3].

Since the initial focus on the transplantation of pancreatic islets, interest in surface modification has spread to many different cell types [7]. This concept of immunoisolation

has been thought to be a potential source for a universal blood 'type' or rather allowing any blood type to be received no matter the recipient's type. The engraftment of bioinert molecules on the surface of red blood cells sterically blocks the host from recognizing the ABO antigens initiating an immune response against the donor blood [4]. A schematic of this concept is illustrated in Figure 2.1. In the early studies, cells were reacted with one end of long or bulky polymer chains. This was accomplished through covalent attachment of methoxypolyethylene glycol [5] or hyperbranched polyglycerols [8] with the commonly used N-hydroxy-succidimidyl ester (NHS). NHS reacts readily with primary amines found on proteins forming a covalent link.

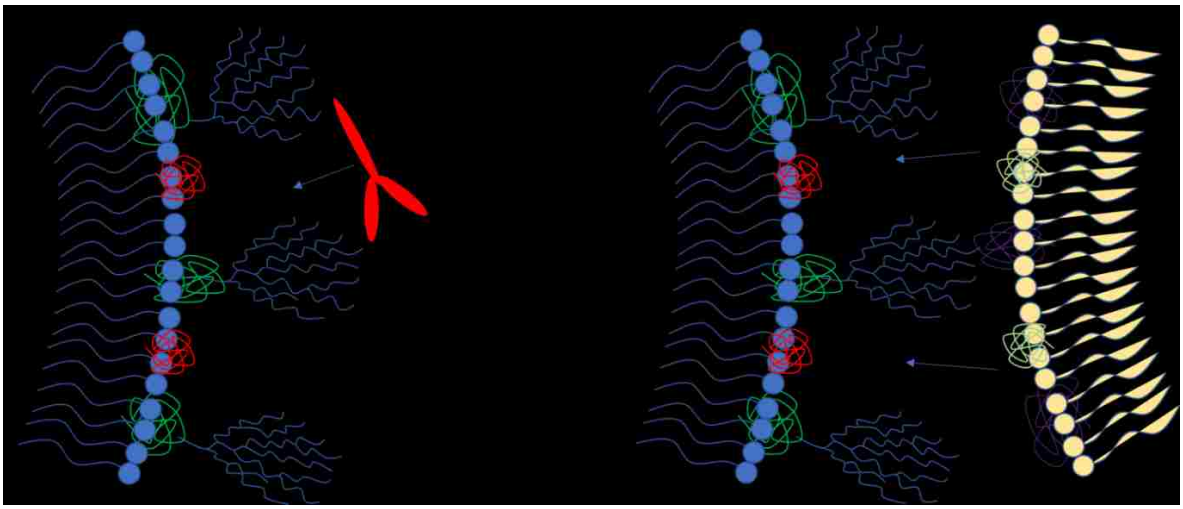

Figure 2.1: Schematic of immunoprotection by physical barrier from covalently bound hypderbranched polyglycerols to the cell surface from (a) antibody recognition, (b) immune cell interaction.

Many other types of surface modifications, including inorganic coatings, have been studied for their potential to protect the cell from harmful environments. Due to the lack of a structurally rigid cell wall, mammalian cells are far more susceptible to toxins and biological stimuli than many other cell types. Coatings have been developed to protect

these vulnerable cells from harsh stimuli such as oxidative stresses, enzymatic attack, and other cytotoxic molecules. In a similar manner to covalent immunoisolation, physiochemically adsorbed silica has been used to form a protective barrier on mammalian cells to protect them from enzymatic attack by trypsin and the cytotoxic agent poly(allylamine) hydrochloride [9]. An inorganic-organic hybrid coating has also shown protective potential of mammalian cells. Tannic acid binding to the surface of the cell followed by complexation with Fe^{III} has shown protection from the cytotoxic agent polyethyleneimine, again through a physically formed barrier. This coating also provides protection from UV-C radiation due to the ability of tannic acid to absorb UV rays [10]. Surface modifications also have applications for protection against chemical stimuli by using reactive moieties in contrast to inert steric barriers. By functionalizing the surface of red blood cells with a known radical scavenger, (2,2,6,6-tetramethyl-1-piperidinyl)oxy (TEMPO), these cells were protected from oxidative damage in an in vitro model [11]. These red blood cells were functionalized with TEMPO through covalent coupling of NHS to primary amines of lysine groups found on the surface proteins of erythrocytes.

2.2 Drug Delivery

Functionalization of cellular surfaces extends from cell protection to drug delivery as well. The vast majority of drugs are currently delivered to target sites by passive transport through air ways and the circulatory system. With developments in nanoparticle systems, drug delivery has made great strides in recent years. However, passive transport is often accompanied by minimal targeting, short circulation time, and undesired systemic effects [12]. By harnessing the mobility and homing ability of living cells, drugs can be delivered more effectively through active transport increasing targeting ability and

retention time within the body [12, 13]. In this concept, the therapeutic agent is attached to the surface of cells by a degradable or diffusive polymer where it is carried directly to the site of interest for release, or is maintained in circulation for controlled release.

As with applications in cell protection, the cell surface provides a range of biomolecules and functional groups to which nanoparticles or patches can be attached. The simplest method for cells to become drug carriers is through nanoparticle adsorption. Adsorption can be dominated by electrostatic interaction, hydrophobic interaction, and van der Waal forces depending on the particle being attached [7, 14, 15]. Living cells have a largely negative charge on the surface due to charged functional groups that make up the cell membrane. This negative charge creates a simple electrostatic attraction when using a cationic nanoparticle or polyelectrolyte multilayer patches [16]. The lipid bilayer of the cell presents a hydrophobic site within an aqueous environment for hydrophobic functional groups to favorably interact. Each of these functionalization methods are non-specific to cell phenotype. Through non-specific binding, polystyrene nanoparticles have shown greater retention times while attached to red blood cells (RBCs) than nanoparticles alone *in vivo* [14]. Non-specific adhesion to RBC surfaces has one advantage of allowing the surface of the nanoparticle to be functionalized with other delivery applications instead of purely for cell binding motifs. Nanoparticles for potential drug loading have also been covalently attached to red blood cells (RBCs) with minimal effects on clearance times and immunogenic pathways [8]. Hyperbranched polyglycerol (HPG) nanoparticles have similar biocompatibility as PEG due to their molecular similarities but do not have the potential recognition by PEG antibodies [17] found in some healthy patients. This is especially important for applications with goals of extended drug circulation time; antibody

recognition would clear functionalized RBCs at a much faster rate than unmodified or unrecognized cells.

For a greater target specificity than is possible by passive transport, surface modification of homing cells is attracting significant attention [7, 18]. Cellular patches can be attached to the surface of living cells in similar ways to that of nanoparticles. Hydrogel patches have been successfully attached to the surface of living cells through localized photopolymerization [19]. Using initiator functionalized cells and a photomask, very small sections of cells can be exposed to radiation resulting in extremely localized hydrogel formation [19]. These patches have the potential to be loaded with small molecule drugs and carried to target sites by the mobility of cells. Homing cells such as macrophages and T cells are prime targets for drug vehicles [18, 20].

2.3 Isolation

Surface modifications for high purity cell separation and isolation are more efficient when compared to specific culturing or density gradient centrifugation as they yield higher purities than gradient centrifugation and are completed in much less time than specific culturing. High purity cell isolation is a desired process in many applications including stem cell therapies, cellular function studies, and circulating tumor cell (CTC) isolation.

Of all surface modification strategies, antibody/antigen binding is the most common and most effective method of initial binding in applications of cell sorting from a heterogeneous population. Surface proteins and expression levels on cells vary drastically depending on species, phenotype, maturity and the surrounding environment [7, 21, 22]. The heterogeneity and large number of surface markers introduces the ability to distinguish subtypes of cells within a mixed population through the highly specific binding of an

antibody to a particular surface antigen. Distinguishability of subtypes or rare populations becomes very difficult when the distinguishing antigen is expressed in low surface densities. Initial studies in our lab have shown that the stem cell marker CD34 on stem cells isolated from human cord blood can be as low as on the order of 10 molecules/μm^2, while other phenotypic antigens such as epithelial cell adhesion molecule (EpCAM) on epithelial cells can have expression levels on the order of 10^3 molecules/μm^2 [21]. When targeting cancer cells in peripheral blood, typically markers that are characteristic to the epithelial phenotype are chosen, such as EpCAM. However, tumor cells are believed to enter into circulation in part through a phenomenon known as the epithelial to mesenchymal transition (EMT). In addition to EMT, tumor cells are also believed to spill into leaky vasculature to create CTCs, which then often results in metastatic disease[23, 24]. In applications of CTC isolation, efforts to better understand EMT are underway.[23-28] In EMT, tumor cells go through a reversible process where they lose many of their adhesive epithelial traits and take on a more invasive mesenchymal phenotype. Whether this happens before entering circulation or once in the peripheral blood, the expression of the commonly targeted surface markers is decreased. The rarity of these cells paired with the change in surface antigen expression has made the enumeration, isolation, and functional study of these highly impactful cells very difficult.

The two most common types of cell sorting methods currently being used are magnetic activated cell sorting (MACS) and fluorescent activated cell sorting (FACS). Antibody recognition is used for both of these sorting techniques to distinguish cell types in a mixed population. Each of these methods have their own advantages and disadvantages making them better suited for different applications. MACS has the primary advantage of high

sorting speed. Magnetic micro beads are functionalized with biorecognition molecules which are typically either a generic species' secondary antibody or streptavidin. The mixed cell population is first treated with a normal primary or a biotinylated primary antibody that is specific to only the target cell type. Once the primary has bound to the target cells, the magnetic microbeads are introduced to the system. Through the highly energetically favorable binding of primary to secondary antibodies, or biotin to streptavidin, magnetic microparticles bind to the surface of the cells creating a cell-bead complex of target cells that is susceptible to magnetic fields. Separation is then accomplished by passing the cell suspension through a column that is within in a strong magnetic field. Non-complexed cells pass through the column into a collection container, while antigen positive cells are retained at the wall of the column within the magnetic field. Finally, the column is removed from the magnetic field where antigen positive cells are washed from the column and collected. FACS uses the same type of antibody labeling to initially distinguish between target and non-target cells. Surface markers are labeled with fluorochromes rather than magnetic beads. Cell separation is achieved through the use of a flow cytometer. The flow cytometer uses microfluidic alignment of the cells to pass them through an excitation laser and analyze each cell individually for a range of fluorescent markers. After cells pass by the fluorescent detectors the microfluidic stream is then aerosolized into droplets containing individual cells. Droplets containing positive fluorescence are then electronically charged. The stream of droplets is passed through an electric field where droplets are diverted into separate containers based on their charge. The individual cell analysis and aerosolization for separation limits throughput of FACS. The initial labeling of the target antigen with its antibody is identical for each process. However, the sensitivity

and specificity, along with the overall processing time are vastly different. MACS has a much lower specificity than that of FACS. Magnetic separation has the risk of physically trapping non-target cells within clusters of target cells and magnetic beads. FACS has the ability to adjust the sensitivity and specificity of sorted cells. In flow cytometry, it is up to the user's discretion to determine the cutoff of what fluorescent intensity is considered positive or negative. MACS has much less control. Sensitivity in magnetic separation is governed by the cell's ability to remain bound to the magnetic bead as the beads are pulled toward the wall of the column and antigen negative cells pass through. This can become a major problem if the surface expression of the target antigen is low. Since FACS uses fluorochromes to detect antigen positive vs. negative cells FACS is not limited to surface antigens. If cell viability is not desired, fixation followed by permeation and fluorescent labeling allows for a wider range of intracellular phenotypic biomarkers to be used as potential targets. In practice, the majority of cell sorting applications require cell viability to be preserved for use or functional study of the target cells.

CellSeach is currently the only FDA approved method for clinical enumeration of CTCs. This system combines the MACS with flow cytometric analysis in order to enumerate CTCs for prognostic information in some cancers. Metastatic breast, prostate, and colorectal cancers have been shown to display poorer prognosis in patients that exhibit a CTC concentration above a given threshold. CTC concentrations >5 cells per 7.5 mL of blood for breast [29] and prostate [30] cancer, and >3 cells per 7.5 mL of blood for colorectal cancer [31] has been show to indicate a less favorable prognoses for these metastatic cancers. Along with the significance in CTC presence, the lack of CTC's among healthy or non-metastatic patients highlights the fact that CTC specific to metastatic

disease, and supports the need for continued research of CTC behavior. Only 0.3% of healthy patients exhibit CTC concentration ≥2 CTCs in 7.5 mL of blood [32]. CellSearch first uses MACS as a pre-enrichment step. Magnetic micro beads functionalized with the antibody against EpCAM are used to positively select cells possessing characteristics of the epithelial phenotype. The collected cells following MACS are then fixed, permeabilized and intracellularly stained for cytokeratin and leukocyte common antigen (CD45). Cell analysis is achieved through the use of a Celltracks Analyzer II to identify cells that are positively fluorescent for cytokeratin, and are also negative for CD45. The Celltracks Analyzer II is an automated fluorescent imaging machine in which images of all positive events are obtained for confirmation by the operator. Pre-enrichment using MACS decreases the analysis time by reducing the number of cells to be analyzed by flow cytometry as well as visually, but it is still a limitation in the event that the process be scaled to larger batches. However, the largest problem with CellSearch is the lack of viable cells following isolation. Although this is a powerful tool for prognosis, it sheds no light on the functional properties of CTCs. This system serves its purpose of enumeration relatively well, but has no translation into further applications due to cell fixation. Pairing the statistical data of poor prognosis with the presence of CTCs and the absence of epithelial cells circulating in healthy patients, with the still uncertain mechanism of metastatic progression and EMT illustrates a need for an isolation technique that results in viable CTCs for further investigation as well as prognosis.

2.4 Antigen Specific Lysis

A novel cell isolation method has been developed in our lab that combines the benefits of MACS sorting speed, and FACS high purity sorting, called antigen specific

lysis (ASL) [33]. ASL uses surface initiated photopolymerization to encapsulate and protect specific cells from chemical lysis in the presence of harsh surfactants. Through the same utilization of primary antibody recognition, ASL preserves the same specificity as that of FACS for immobilization of a visual light photoinitiator onto the surface of target cells. Suspending the cell population in an acryloyl monomer solution containing a tertiary amine co-initiator followed by irradiation with 530 nm initiating light, results in rapid local polymerization fully encapsulating target cells. Once target cells are protected, the cells are subjected to harsh environments such as hypotonic conditions or surfactants that effectively lyse all antigen negative cells. This leaves behind essentially a 100% pure population of target cells. ASL provides the high throughput advantages of magnetic sorting and the same purity of fluorescent sorting all with relatively inexpensive materials. These traits make this technology highly desired in clinical applications of many sorts. The versatility of ASL is governed largely by cytocompatibility of the monomer solution. As regenerative engineering and cellular therapies continue to be highly researched, the choice of cytocompatible monomers is much less of a challenge than in previous years. PEG based monoacrylates and diacrylates (PEGMA and PEGDA) of many molecular weights, gelatin methacryloyl, alginate, poly(lactic acid), and more have been successfully used with living cells while maintaining cell viability [34-36]. A wide variety of monomer materials available for use with cells means that polymer properties can be highly tuned to desired specifications. Whether polymer mesh size, degradability, or hydrogel mechanical properties need to be tuned, simple adjustments in monomer formula can be made without significantly effecting processing time or targeting specificity.

The use of a visible light photoinitiator eliminates the possibility of UV mediated damage [37] to cell DNA. Eosin Y is a type II, photoinitiator that is excited by light that is 530 nm; well out of the UV range. It is a member of a class of dyes derived from xanthene [38]. Apart from operating in the range of visible wavelengths, eosin is extremely powerful due to its ability to generate a large number of initiating radicals per fluorophore [39-41]. Type I photoinitiators are photocleavable molecules that degrade into two radical species [42] effectively limiting the molecule to a maximum of two initiated polymer chains. Once these radicals are terminated, polymerization ceases. Eosin however, has the ability to regenerate. Type II photoinitiators require a co-initiator to produce an active radical and allow the molecule return to its ground state without degradation[41]. A proposed initiating mechanism for eosin is first through the absorption of a photon electronically exciting the dye. The molecule undergoes a phenomenon called intersystem crossing from the singlet excited state to a triplet excited state. Here the initiator reacts with a co-initiator, commonly a tertiary amine, to yield radical species. It is believed that electron transfer from the tertiary amine to the excited eosin molecule followed by proton abstraction from the amine to the eosin results in two neutral radical species, a radical amine and an eosin radical [40]. Of these two, the radical amine is much more reactive to acrylate groups than that of the eosin radical and therefore is primarily responsible for the initiation of propagating chains [38, 41]. Once initiation of a chain is achieved, propagation and termination proceed as normal free radical polymerization reactions. As the active chains propagate, the excited eosin radicals then return to the ground state where they can be excited to generate more amine radicals. Initiation will continue as long as irradiation continues and there are sufficient co-initiator molecules in solution, until all eosin molecules are photobleached. While the eosin

initiator is tethered to the surface of the cell, the amine which becomes the amine radical is not. Diffusion of active radical species, and therefore monomer molecular weight, away from the cell surface plays a critical role in film formation. The curvature of the cell in relation to the film thickness and monomer lengths permits for modeling using a planar surface. Primary diffusion concerns are unidirectional away from the cell surface. If diffusion of active radical species away from the cell surface occurs at higher rates than chain propagation, polymer or oligomer formation may occur without achieving full encapsulation. A typical characteristic of free radical polymerization is the high reaction rate due to the high reactivity of most radical species. In our applications, monomers have a functionality >2 which results in a covalently crosslinked network. At high monomer conversion, the crosslink density or pore size within the network is greatly governed by the molecular weight of the major monomer species. The crosslink density determines what molecules may diffuse through the hydrogel film and what is restricted, which is critical to protection from surfactants as well as immune response *in vivo*. Termination is achieved by a few possible reactions. Active radical chains can undergo combination reactions with other active chains, radical initiating species, or radicals that are a result of chain transfer reactions. Active radicals can also be quenched by residual oxygen within the system, which is why the polymerization is carried out under an inert nitrogen atmosphere.

This polymerization process and powerful initiating mechanism has proved very useful in sensitive detection of biomolecules on micro array slides. Polymerization based amplification (PBA) capitalizes on eosin's ability to continue to generate radicals while under irradiation to form polymer films entangled with fluorescent nanoparticles for easy detection [43-45]. It has been shown on micro array slides that biomolecules can be

recognized in surface densities <0.2 molecules/μm^2,and can amplify fluorescent signal by 100 fold over standard fluorescent methods [43].

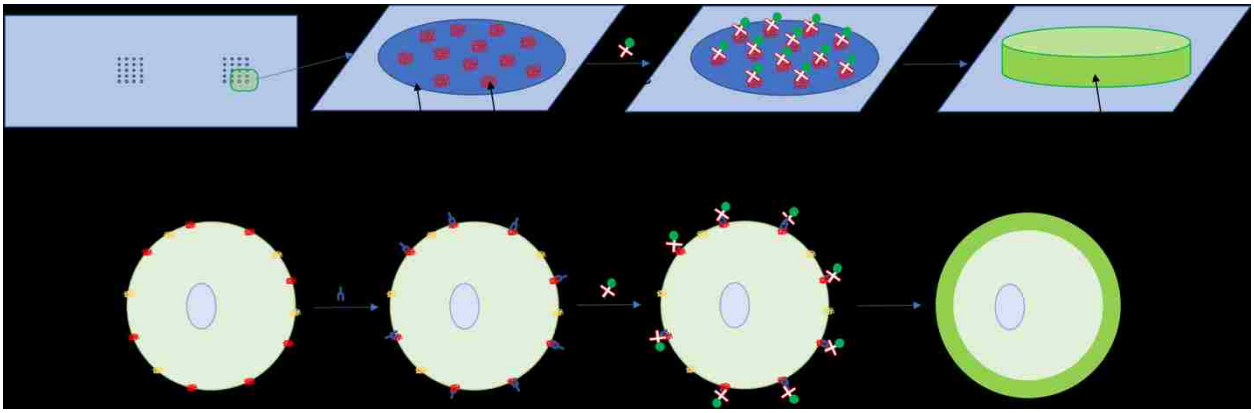

Figure 2.2: Schematic of the polymerization procedure for micro array and cell surface polymerization.

For cellular applications, this translates to improved biorecognition of low surface expression antigens. Figure 2.2 illustrates polymerization process on micro arrays as well as cellular surfaces. Achieving full encapsulation while targeting low expression molecules is essential in CTC and stem cell isolation. Low expression levels for MACS or FACS results in poor magnetic bead binding or weak fluorescent signal to distinguish between positive and negative populations. Using the PBA system in ASL, we can overcome the surface expression challenge by adjustments in irradiation time and monomer formula.

2.5 Mechanical Protection

ASL technology provides mechanical protection in applications of bioprinting as well. Three-dimensional printing has gained substantial momentum in the past few decades. 3D printing of anatomical structures has been used in the medical field to better help visualize and understand complex morphologies in ways that a 2D depiction could not

capture. In surgical planning, imaging and subsequently printing target organs or anomalies of surgical interest allow for a more well-planned surgical process [46, 47]. More recently 3D printing has been used with biomaterials to print cellular and acellular scaffolds for tissue engineering in regenerative medicine [48-54], 3D organ-on-a-chip platforms for in vitro drug screening [55, 56], and even functional prosthetics [57, 58]. As goals approach the printing of large scaffolds and whole organs, the need for high throughput and high-resolution printing is evident. Mechanical forces are inherent in fluid flow and become a much larger issue on the microfluidic level when dealing with live cell printing. Many commercial bioprinters are extrusion-based printers that use pressure driven or mechanically driven flow to push fluid through a small orifice or nozzle in a direct-write fashion [59]. Shear forces are the forces created by a radial velocity gradient of the fluid in laminar flow through a tube. These shear forces increase with higher flow rate and smaller nozzle diameter, both of which are desired for whole organ printing. These shear forces have the ability to damage the membrane or completely lyse cells as they pass through the nozzle during printing. This is the largest disadvantage to extrusion-based printers and poses a problem to large, functional organ printing. Commonly, 3D cell printing is done at resolutions much greater than that of a single cell (150-300 μm nozzle diameter; epithelial cell diameter ~10-20 μm) at flow rates that are typically on the order of 1-10 μL/min [60-63]. With these print rates it would take 10^2 days to print one large organ and still without achieving the necessary detail of high-resolution printing. To achieve the necessary detail involved with printing vasculature, single cell resolution is highly desired. Much work has been done to try to minimize shear forces experienced by cells such as altering print heads [64], using low viscosity bioinks [65] or using shear thinning fluids [63]. Printing

techniques have been able to print with high cell viability, but still with moderate resolution and relatively low throughput. More research must be done to achieve the resolution and throughput for plausible organ printing.

The same technology that provides protection against chemical stimuli for high purity isolation also has the ability to provide protection against mechanical forces. Through individual cell encapsulation, the hydrogel coating provides membrane reinforcement against mechanical stimuli. As cells travel through a narrow tube, the shear forces create a tensile strain on the cellular membrane. In high flow rates the tensile strain becomes more than the membrane can withstand causing cell lysis. Hydrogel coatings possessing the proper mechanical properties support the membrane allowing the cells to remain intact upon intense shear forces.

CHAPTER 3. MATERIALS AND METHODS

3.1 Poly(ethylene glycol) diacrylate synthesis

Synthesis of poly(ethylene glycol) diacrylate was performed as described previously [33]. For PEGDA 3400 25 g of poly-(ethylene glycol) (PEG; M_n ~3000-3600 Sigma) were added to a round bottom flask and purged with ultra-pure nitrogen for 10 min. Anhydrous dichloromethane (DCM; 75 mL) was added to the flask and PEG was allowed to dissolve under magnetic stirring for 5 min. A water bath was used as a heat sink for the round bottom flask while stirring continued. Triethylamine (TA; Sigma) and acryloyl chloride (AC; Sigma) were used with PEG in a 1:4:4 mole ratio of PEG:TA:AC. TA (4.25 mL) was added directly to the dissolved PEG under continuous stirring. AC (2.4 mL) was mixed with DCM (12.4 mL) and added to the top of the addition funnel by injection through a septum and purged with nitrogen for 15 min. AC/DCM was then added dropwise to the PEG/TA/DCM mixture at a rate of ~ 1 drop every five seconds under continuous stirring and nitrogen purging. Once all of the AC/DCM was added, the flask was sealed and covered with foil to react overnight under continuous stirring. The reaction mixture was then filtered through a Buchner funnel and washed with excess DCM to remove insoluble TA salts. Then 10-fold molar excess sodium carbonated was added to the mixture and stirred for 1 hour, followed by filtration through a Buchner funnel and washed with DCM removing any insoluble sodium carbonate. The solution was then passed through a bed of alumina (Sigma, ~ 3-5 cm thick) in a glass frit column and washed with DCM. The DCM was evaporated off using a rotary evaporator until ~ 50-100 mL of DCM remained. PEGDA was precipitated out using ~ 10 x the DCM solution volume of cold ether. Solution was kept at 4 ˚C for 1 h to ensure precipitation. Precipitated solids were collected by

filtration with a Buchner funnel and allowed to dry in the dark, under vacuum overnight. Precipitation in cold ether was repeated for further purification as needed. Polymer structure and acrylation was determine by H^1 NMR (DMSO). Acrylation was confirmed by the characteristic peaks for the three hydrogens bound to the carbon-carbon double bond of the acrylate functional group. PEGDA 1000 (PEG M_n ~950-1050; Sigma), and PEGDA 2000 (PEG M_n ~1900-2200; Sigma), were synthesized following this procedure using the same reagent equivalents.

3.2 Cell culture

All cell types were cultured in medium supplemented with 10% FBS (VWR) and 1% penicillin/streptomycin (VWR) at 37 ˚C and 5% CO_2. H9C2 (ATCC CRL-1446) rat cardiac myoblasts were cultured in Dulbecco modified eagle medium (DMEM, HyClone). Human non-small-cell-lung cancer lines (A549 and H358; ATCC CCL-185 and ATCC CRL-5807 respectively) and human breast cancer lines (T47-D, MCF-7, MDA-MB-231; ATCC HTB-133, ATCC HTB-22, ATCC HTB-26 respectively) were cultured in Roswell Park Memorial Institute (RPMI 1640) medium.

Cells were seeded in 75 cm^2 tissue culture flasks (VWR) for 24-72 h and were 80-95% confluent prior to use. Cells were harvested using 0.25% Trypsin-EDTA 1X (VWR) for 90 s. Then, cells were collected and washed with 5 mL medium to neutralize the trypsin. Cells were centrifuged at 4 ˚C and 400 x *g* for 3 min, supernatant was aspirated and cells resuspended in 1 mL PBS for one wash. Cells were washed twice and resuspended in PBS (HyClone) for processing.

3.3 Viability assays

Cell viability was assessed through multiple methods. Metabolic activity was assessed through the use of the MTT assay. The MTT assay is a colorimetric method used to measure mitochondrial activity within the cell giving information on viability and proliferation relative to a control group of unprocessed cells. 3-(4,5-dimethylthiazol-2-ly)-2,5-diphenyltetrazolium bromide (MTT; Thermo) is a water soluble dye that in the presence of active mitochondrial reductase is reduced into (E,Z)-5-(4,5-dimethylthiazol-2-ly)-1,3-diphenylformazan (formazan), a water insoluble dye. An equal number of cells (~10,000) from each sample were incubated in 200 μL of medium with 0.45 mg/mL MTT for 3-4 hours at 37 ˚C ($n \geq 3$ for each sample). All separate samples were measured in a 96 well plate (Celltreat). After incubation, the plate was centrifuged, wells were aspirated and well contents were solubilized in 200 μL of DMSO (Sigma). Absorbance of 570 nm light for each well was measured using a Biotek plate reader. Absorbances for each sample were averaged and normalized to control cells for relative viability.

Viability by membrane permeability was measured using ethidium homodimer-1 (EthD-1; Thermo Fisher). EthD-1 is a large, membrane impermeable dye that binds to nucleic acids. It is a red fluorescent dye that is weakly fluorescent until bound to the nucleus. Due to size of the molecule, the dye is only able to permeate the membrane of a dead or damaged cell. Healthy cells with complete membrane integrity will show little or no fluorescence. EthD-1 assays were conducted at a concentration of 2 μg/mL with cells in PBS at room temperature for 5 mins. Viability was assessed by fluorescent microscopy and flow cytometry.

3.4 Cell tracking

Syto 62 deep red nuclear stain was utilized for cell tracking through cell processing. The Syto dye is a membrane permeable nucleic acid stain which allowed for better accuracy during processes that involved cell membrane fragmentation. This stain was used at 1 μg/mL for 5 min on ice. Cells were then washed 2x in PBS before further processing.

3.5 Micro array printing

As a model of the cellular surface protein expression, biotin printed micro array slides were used. Biotinylated bovine serum albumin (bBSA; Thermo Fisher) was printed in serial dilutions of 1000, 400, 160, 64, 25.6, and 0 μg/mL. All dilutions were made with a 1000 μg/mL solution of bovine serum albumin (BSA; Sigma) in PBS (PBSA) in order to keep the total protein concentration constant at 1000 μg/mL. Micro arrays were printed using an Affymetrix 417 Arrayer, and Array It epoxy coated microscope slides at 60% humidity. Each micro array consisted of six columns of the different bBSA concentration, with each printed four times to make up a 4x6 array. Two arrays were printed on each slide to be centered within the wells of the Whatman chip clip slide holder. Once printed, slides were placed back in slide boxes away from light to dry for >12 hours under ambient conditions. One slide from each batch was analyzed using a streptavidin-Cy3 (SA-Cy3; Thermo Fisher) conjugate and micro array scanner. SA-Cy3 labeling was performed as described below for SA-EITC labeling with a working solution of 20 μg/mL SA-Cy3 in PBSA. Slides were scanned on a Affymetrix 428 Array Scanner using the 532 nm laser line and 570 nm absorbance. Fluorescent intensities were compared to a Cy3 calibration slide to ensure successful and consistent bBSA printed surface densities.

3.6 Micro array polymerization

Biotinylated BSA (bBSA) slides were placed in a Whatman chip clip side holder for processing. Each well of the micro array slide was processed one at a time to ensure no photo-bleaching of the photo-initiator. The well was first washed with 400 μL of 1 mg/mL BSA in PBS (PBSA) to remove any unreacted bBSA. A blocking step was then performed by incubation of 400 μL of PBSA for 40 min at room temperature, covered from light. bBSA printed arrays were functionalized with streptavidin-eosin isothiocyanate (SA-EITC) or streptavidin-fluorescein isothiocyanate (SA-FITC) by incubation with 400 μL of ~30 μg/mL SA-EITC or SA-FITC in PBSA for 30 min covered from light. Following initiator labeling, the well was washed 3x with PBS to remove any unreacted SA-EITC. PEGDA (M_n = 575, 700, 1000, 2000, 3400) monomer formulations were as follows: 25% wt/v PEGDA, 35 mM triethanol amine (TEA; Sigma), and 35 mM vinyl pyrrolidinone (VP; Sigma). PEGDA M_n 575 and 700 were purchased from Sigma, while M_n 1000, 2000, and 3400 were synthesized in house based on published protocols [33]. 350 μL of monomer solution were place in the chip clip well prior to irradiation. The chip clip was placed inside a polymerization chamber constructed of two petri dishes and purged with ultra-pure nitrogen for 5 min at 0.8 standard L/min. Nitrogen was bubbled through water prior to entering the purging chamber to decrease evaporation of the aqueous monomer solution. After purging, nitrogen flow rate was reduced to 0.2 standard L/min to further reduce evaporation of the sample. Irradiation was achieved using two possible sources, both at the same intensity of ~35 mW/cm^2, for 10 min. One lamp is a small, collimated LED (M530L3, Thorlabs) and the other is a large LED array lamp (Photon System Instruments). Both lamps are green LEDs centered near 530 nm. Following irradiation, slides were removed

from the chip clip, washed with DI water, and allowed to dry over-night before further analysis.

3.7 Profilometry

Profilometry gives topographical information in very fine resolution. Here we used it to measure step height of the film generated in localized polymerization in micro arrays on initiator labeled spots. Micro arrays were polymerized and allowed to dry for >12 hours before profilometry on a Daktek 6M Profilometer. Profilometer scans were done on all four spots for each individual bBSA print concentration. Profilometry uses optics to measure deflection angle of light from a cantilever in contact with the surface of the sample. Scans were done at 1 mg of force with a scan rate of ~40 μm/s. Scans were zeroed on both sides of each spot before measurement.

3.8 Streptavidin-fluorophore conjugation

The photoinitiator, eosin isothiocyanate (EITC), was conjugated to the biorecognition molecule, streptavidin (SA) as reported previously [66]. First, 0.1 M sodium bicarbonate (pH ~8.3) was mixed with 0.1 M sodium carbonate (pH ~11.3) to obtain a carbonate buffer of pH 10.2. Then 95 μL of 10 mg/mL SA in carbonate buffer was mixed with 9.5 μL of 10 mg/mL EITC in DMSO. The mixture was covered from light and placed at 4 ˚C for 8-12 h. The mixture was then diluted with 1 mL PBS before purification. The SA-EITC conjugate was purified by passing through a 7 kDa molecular weight cut off desalting column (Zeba Spin, Thermo Fisher). Conjugate ratio was determined using UV-VIS absorbances at 530 nm and 280 nm (NanoDrop 2000, Thermo Scientific). Using standard absorbance curves of SA and EITC alone, absorbance corrections were made and

ratios were calculated as described previously [66]. Typical SA-EITC ratios range from 4-6 EITC molecules per SA. Chapter 5 experiments containing SA-FITC and SA-Cy3 were processed identically measuring absorbances at 495 nm and 550 nm respectively.

3.9 Cell encapsulation

Cells were cultured and harvested as described above. The polymerization procedure was the same for all cell lines unless stated otherwise. Samples were split into 1.5 million cell aliquots for encapsulation. Biotin was covalently labelled to cell surface proteins using a biotin-succinimidyl ester conjugate (NHS-biotin; EZ-link Sulfo-NHS-LC-Biotin, Thermo Fisher). Cells were incubated in 250 μL of 0.55 mg/mL NHS-biotin for 40 min on ice, then washed 3x in PBS. Eosin was then conjugated to the cells using an in-house synthesized streptavidin (Thermo Fisher)-eosin isothiocyanate (EITC, Sigma) conjugate (SA-EITC, as described above). Cells were incubated in a PBS solution of ~30 μg/mL SA-EITC for 30 min on ice covered from light. The sample was then washed 3x in PBS before introduction to the monomer solution. After the final wash in PBS, cells were pelletized, aspirated, and resuspended in 350 μL of monomer solution. PEG based monomer solutions were all the same as described for micro array polymerization above. Gelatin methacryloyl (gelMA) monomer formulations contained 3% wt/v gelMA, 1 % wt/v PEGDA 3400, 35 mM TEA, and 35 mM VP. All monomer formulations were adjusted to pH 7.3-7.5 for use with living cells. This monomer/cell suspension was transferred to a chip clip (Whatman) containing a glass slide and placed in a chamber constructed of two 150 mm clear polypropylene tissue culture dishes. This chamber was purged with nitrogen with a water bubbler for 5 mins at 0.8 standard L/min before irradiation. During irradiation, nitrogen was reduced to 0.2 standard L/min to reduce evaporation of the sample. Cells were

irradiated with a 530 nm collimated LED lamp (Thorlabs) at 35 mW/cm^2 for 10 min for the surface polymerization reaction. After polymerization, cells were removed by pipette and the chip clip was washed 2x with 500 µL PBS. The glass slide was then removed and scraped with a cell scraper to ensure maximum cell recovery. Cells were washed 2x in PBS and strained with a 40 µm cell strainer (VWR) to remove any cell aggregates and bulk polymer particles prior to further processing.

3.10 Hypotonic Challenge

Hypotonic challenge was performed on cells for proof of encapsulation. Cells without membrane reinforcement will swell and burst in the presence of pure water, while fully coated cells will remain intact. Cells were centrifuged and aspirated, then resuspended in DI water at ~ 20,000 cells/mL. Cells remained in DI water for 10 mins at room temperature. Tonicity balance was restored using 10x PBS before flow cytometry or viability analysis.

3.11 Surfactant Challenge

Surfactant challenged cells were suspended in PBS prior to introduction of Sodium dodecyl sulfate (SDS) or Triton-X (TX) 100 (both Sigma). A 10% wt/v solution of SDS, and a 5 mM solution of TX in PBS were made as stock solutions. Surfactants were introduced to the suspended cells in a 1:2 dilution. Cells observed surfactant concentration was 5% wt/v for SDS and 2.5 mM for TX, which are 20x and 10x the concentration of the critical micelle concentration respectively. Cells were incubated in a particular surfactant solution for 10 min at room temperature. Cells were then centrifuged, aspirated and washed with PBS before flow cytometry or viability analysis.

3.12 Extrusion

High throughput, high-resolution cell printing was simulated by extrusion of a cell suspension through a 5 cm long, 50 μm diameter capillary (IDEX Health and Science). Protection potential of each monomer formulation was determined by percentage of intact cells following extrusion through the capillary. The capillary was fixed to a luer lock by compression fitting and attached to a 1 mL syringe (BD Biosciences). The syringe was loaded with 0.5-1 million cells in 1 mL of PBS, placed in a syringe pump (Harvard Apparatus) and turned upright so that the syringe was held vertically. The syringe pump extruded the contents of the syringe at 4.8 μL/s into an open microcentrifuge tube (VWR). Following extrusion, cells were analyzed by flow cytometry (Accuri C6) using forward scatter and side scatter gating to determine whole vs. lysed cells both before and after extrusion, as well as all viability assays mentioned above.

3.13 Shear without pressure change

To observe the effect of shear forces on coated and uncoated cells in the absence of a pressure drop, a parallel disc viscometer was used (DHR2, TA Instruments). Cell suspensions were loaded onto the bottom disc of the viscometer and the top disc lowered. Viscometer studies were performed at a 30 μm gap and a 300 rad/s angular velocity, with an exposure time of 10 s. Shear stress was measured by the instrument at ~110 Pa during each run. Cells were then collected and analyzed by flow cytometry and EthD-1 viability and MTT assays to determine the protective potential for each monomer solution against uncoated cells.

3.14 Rapid Pressure Drop

Cells were subject to high pressures and rapid decompression simulating the pressure changes extruded cells experienced in the absence of shear forces. Suspended cells were placed in micro centrifuge tube at similar concentrations to extruded solutions. The open centrifuge tube was placed inside a pressure chamber (Parr Instrument Company) and charged with nitrogen to pressures above and below those experienced during the extrusion process (8-25 bar), followed by sudden decompression back to atmospheric pressure. Pressure was held constant for two separate lengths of time. First, cells were exposed to these high pressures for ~2 min to simulate similar time scales of the extrusion process above. Separate samples were then held at high pressures for ~10 min to determine if longer exposure times would affect cell viability. Cells were then analyzed through flow cytometry to determine whole vs. lysed cells, as well as all viability assays mentioned above.

3.15 Mechanical properties

The swelling ratio of each polymer was determined in deionized water (DIW). Monomer formulations were supplemented with 1 mM EITC in DMSO at a 1:10 dilution for a final EITC concentration of 0.1 mM. Each sample was subjected to the same nitrogen and irradiation conditions as cell coating experiments above. Bulk gels were formed in a chip clip on a glass slide using a 16 well clip. 75 μL of monomer solution were placed in a well for polymerization. The chip clip containing the monomer solution was then irradiated with 530 nm light for 10 minutes. Upon the formation of bulk hydrogel, the gel was placed in 4 mL of DIW for 4-8 hours on a rocker table to allow for complete saturation. Gels were

removed from water, patted to remove excess water and weighed in their swollen state. All gels were then placed under vacuum for ~24 h and weighed again in their dry state.

Unidirectional tensile testing was also performed on each polymer type. Films were generated in 9 x 9 cm square tissue culture dish at ~1 mm thickness. Gels were placed in water for 24 h prior to testing. Test samples were stamped out of the film in a 'dog bone' shape (5 mm width at center) and each end glued to glass slides with cyanoacrylate super glue (HDX). PEGDAs 700, 1000, 2000, and 3400 were tested on an Instron tensile tester. GelMA/3400 was too soft for the limits of the commercial tensile tester and therefore was tested using an in house designed tensile tester composed of a step motor (Oriental Motor Co.) and 10 g load cell (Transducer Techniques). Initial length and film thickness were measured by digital calipers before force was applied. Tensile strength was measured as the film was stretched at a rate of 4 mm/min until failure. Stress/strain curves were generated and modulus, ultimate tensile strength, and percent elongation at failure were calculated.

3.16 Flow cytometry

Flow cytometry analyses were done on an Acuri C6 table top cell analyzer. Flow cytometry was used to observe cell size, morphology, and fluorescent characteristics of cellular events. With this machine light scattering properties as well as fluorescent properties from four different wavelengths are recorded for each individual event analyzed. Cells suspended in PBS are pulled up into the machine by a sip and peristaltic pump. Micro fluidic channels then funnel the sample down using a sheath fluid to pass the cells one-by-one through the laser. Optical detectors are placed directly in line with the incident light on the opposite side of the fluid sample and perpendicular laterally to the laser. Size and

morphology information is obtained from forward scattered light (FSC) to the inline detector and side scattered light (SSC) to the perpendicular detector respectively. Four light detectors with different optical filters collect information regarding fluorescent intensity of the specific wavelength. All optical information is recorded for each event processed. This powerful tool gives quantitative information regarding cell viability when using the fluorescent viability assays mentioned above. EthD-1 and Calcein dyes are easily analyzed quantitatively through the use flow cytometry and fluorescent filters. Intact cellular events were determined by FSC and SSC values compared to control samples before particular processes.

CHAPTER 4. QUANTITATIVE ANALYSIS OF SURFACE MARKERS FOR CTCS AND CURRENT ISOLATION STRATEGIES

4.1 Introduction

Metastatic cancers are by far the most deadly form of malignant tumor, attributing to more than 90% of cancer related deaths [26, 67]. Metastasis occurs when cells from the primary tumor make their way into circulation before reaching and colonizing distant tumor sites [67]. These circulating tumor cells (CTCs) have been intensely studied since the first observation in 1869 [68]. The presence of these CTCs in cancer patients introduces the potential of a fluid biopsy for cancer screening. Such a biopsy comes with major advantages of minimally invasive acquisition, early diagnosis, and greater depth of prognostic information. Solid tumor biopsies can be painful and have associated risks of invasive procedures. A fluid biopsy that could be achieved through a standard peripheral blood draw would have great clinical utility. Early diagnosis and treatment of cancer patients has been shown to greatly increase the treatment efficacy and survival rates [69, 70]. CTC presence is believed to occur at very early stages of cancer. By the time that a solid tumor is large enough to be observed on a scan, the patient may have had CTCs for >10 years [71]. Rare cell isolation techniques are an area of intense study due to multiple applications in CTC isolation, stem cell isolation, and the ability for functional characterization of these highly impactful populations. The extreme rarity of these CTCs along with evidence that suggests multiple, distinct populations can arise from a single tumor primary with variable phenotypic profiles [72-74], greatly hinders current isolation strategies from accurately isolating functional cells.

4.1.1 Current Isolation Strategies

Viable cell sorting is highly desired in clinical settings as well as for cell biology research. Many current methods are affinity based and use specific cell surface molecules to distinguish rare populations or subtypes from the rest of the sample [75]. These methods are considered passive strategies. Separation is achieved by immobilization or deflection of target cells away from the general flow within microfluidic devices. Nagrath et al developed a CTC isolation chip that immobilizes CTCs without the need of any pre-labeling or processing of cells [76]. This microfluidic chip contains micro posts coated with antibodies against epithelial cell adhesion molecules (EpCAM), a commonly targeted antigen for CTCs. Whole blood flows through the chip at controlled laminar conditions where cells expressing EpCAM are bound and then collected by elution [76]. Another label free microfluidic device uses molecule specific affinity in 'deterministic cell rolling' to isolate target cells [77]. Antibody or protein functionalized grooves initiate cell rolling with a slightly orthogonal trajectory to the fluid flow, separating positive cells from the rest of the population where they are collected. This method has been shown to isolate a number of cell types from a heterogenous population with high purity (>90%) [77] . Deterministic cell rolling has shown promise of high purity but has not been used for CTC isolation. While many of the affinity based microfluidic methods are able to achieve relatively high purity, it comes at the expense of processing speed. Many of these devices operate on the order of 10 μL/min [75-77].

Magnetic activated cell sorting (MACS) relies on cell surface functionalization with magnetic micro beads. Magnetic beads coated with biorecognition molecules, commonly antibodies, are incubated with heterogenous the heterogenous cell population.

Antigen positive cells bind with these particles making them susceptible to a magnetic field. The entire population is then passed through a column in the presence of a strong magnetic field. Antigen positive cells are retained at the walls of the column while all other cells pass through freely. The magnetic field is then removed to collect the antigen positive population. While MACS offers a great advantage of high throughput processing up to 10^{11} cells in 30 min [75], the isolation purity is much lower than that of alternate strategies. The product purity of MACS is highly dependent on the abundance of the target cell in the original population [78]. It has been shown that target cell populations of 1% have yielded only 37% purity following MACS [79]. For this reason, MACS is often used as a pre-enrichment step before processing with another isolation method. Depending on the application of the sorted cells, removal of the magnetic micro beads may also be required.

Fluorescent activated cell sorting (FACS) has been widely used in cell separations due to its high purity sorting abilities. FACS uses fluorescent labeling in much the same way as MACS uses magnetic labeling. Fluorochromes are bound to cells by target cell specific antibodies. Using microfluidics, the cell suspension is funneled down to a single cell stream where it passes through excitation lasers and optical detectors to determine fluorescently labeled cells. The cell stream is then aerosolized and droplets are charged based on their fluorescent characteristics. Droplets are passes through an electric field where they are directed to different containers based on their charge and therefore their fluorescent properties. In viable cell sorting with FACS surface antigens are used for fluorochrome labeling, as opposed to intracellular staining. The surface expression of the target antigen is a critical factor in cell sorting ability.

CellSearch is currently the only FDA approved technique for CTC enumeration. CTC abundance in peripheral blood has been shown to have significant impact on prognosis for some cancers [29-31]. This method combines the high throughput enrichment of MACS with fluorescent labeling of characteristic markers for distinguishability of CTCs. MACS enriched populations are fixed and permeabilized for intracellular staining of the nucleus and cytokeratin, while also staining for leukocyte common antigen, CD 45. Events are considered positive when nucleated, positive for cytokeratin and negative for CD 45. While this method is a powerful tool for CTC enumeration, it does not yield viable cells and therefore has little translation to functional CTC analysis or rare cell isolation applications where viability is necessary.

As many these methods may possess the potential for viable CTC isolation in a clinically relevant fluid biopsy, surface expression of target cells greatly dictates efficacy of antibody based techniques. Low surface expression, or more quantitatively, surface density of target markers decreases the binding of fluorochromes or magnetic beads over non-specific binding hindering the distinction between positive and negative events. For passive isolation techniques, low molecule surface density translates to lower binding affinity leading to decreased retention or rolling initiation of target cells. Currently, the literature contains very little quantitative information regarding surface expression. Most reports for common metastatic markers are given as positive/negative or upregulated/downregulated. Quantitative reports by enzyme immunoassay and enzyme-linked immunosorbent assay are in units of mass of protein per mass of cell lysate. These assays measure total antigen presence of lysed and homogenized cells which include intracellular expression. While this information may be valuable in alternative applications,

viable isolation techniques rely only on surface expression. In this chapter we quantify the surface expression of common cancer related biomarkers.

4.1.2 Common Surface Markers Associated with Metastasis

As most primary tumors are composed of adherent epithelial cells, it is obvious that most strategies target common epithelial markers. Of these, epithelial cell adhesion molecule (EpCAM) is by far the most widely used in the literature. EpCAM is a calcium ion-independent surface protein which is primarily involved in homophilic cell-to-cell adhesion [80]. EpCAM has been shown to have upregulation of two to three orders of magnitude in breast cancer tumors as opposed to healthy tissue [81]. While the targeting of EpCAM on CTCs is highly prevalent, problems can occur such as EpCAM negative cancers, and downregulation or loss of epithelial characteristics upon EMT and entering circulation.

In breast cancer, three highly targeted biomarkers are human epidermal growth factor receptor 2 (HER2), estrogen receptor (ER), and progesterone receptor (PR). These three markers are used to classify subtypes of breast cancer for therapy selection and prognostic information. HER2 is a tyrosine kinase that forms heterodimers with other markers in its family to increase cell division [82, 83]. ER binding with the hormone estrogen plays a role in promoting proliferation of mammary cells. Upregulation of ER is believed to be associated with over proliferation and/or formation of genotoxic by-products [84]. PR is transcription protein that when activated by progesterone controls the regulation of specific genes.

E-Cadherin and N-Cadherin are adhesion molecules that play different roles in metastasis. E-Cadherin is a calcium-dependent molecule that plays a role in homotypic

cell-to-cell adhesion. Decreased expression of E-Cadherin is thought to be one of the first steps in the metastatic progression [85] as well as EMT [86] by decreasing cell adhesion to the primary tumor. N-Cadherin is also a calcium-dependent homotypic cell adhesion molecule, but is also believed to be responsible for detachment mechanisms [87]. Expression of N-Cadherin has been associated with more invasive cancers [87, 88].

CD44 and integrin αVβ3 are both biomarkers that are adhesive to the extracellular matrix (ECM). CD44 is a transmembrane protein that is activated by hyaluronan to stimulate intracellular functions associated with metastasis, including adhesion, migration, and invasion [89, 90]. Integrins are a family of adhesion molecules that play roles in migration, survival, and activation of apoptosis suppressors [91]. Within this family, integrin αVβ3 has been identified as an important marker in early angiogenic activity, tumor growth, invasion and metastasis [92, 93].

Intercellular adhesion molecule 1 (ICAM1) is another adhesion molecule positively expressed in breast cancer [94, 95], that has roles in cell morphology, cell-to-cell adhesions, and migration [96] . Expression of ICAM1 found on CTC suggests that it may play a role in metastasis by promoting migration of cells through the ECM [96]. A major part of metastasis is also the ability to initiate tumor growth and sustain transport of nutrients through angiogenesis. Epidermal growth factor receptor (EGFR) is a member of the tyrosine kinase family and plays a significant role in angiogenesis, proliferation and apoptosis resistance apoptosis [97]. Positive expression of EGFR has been linked to less favorable prognoses over EGFR negative tumors in breast cancer [98].

4.2 Materials and Methods

4.2.1 Peripheral Blood

A peripheral blood sample was obtained with informed consent through University of Kentucky Medical Center IRB protocols and processed within an hour of collection. Whole blood was mixed with dextran and NaCl to a working concentration of 2 wt/v% dextran and 0.3 wt/v% NaCl and was allowed to separate by 1 x g in ambient conditions for 1 hour. The buffy coat containing peripheral blood mononuclear cells (PBMC) was then pipetted off and exposed to a red blood cell lysis buffer (155 mM NH_4Cl, 10 mM $KHCO_3$, 0.1 mM EDTA) for 5 minutes to further remove red blood cells from the sample. Nucleated cells were collected by centrifugation at 300 x g for 5 minutes and washed twice with cold 1 X PBS.

4.2.2 Surface Marker Immunostaining

Tumor cells were cultured and harvested as described in Chapter 3.2. Cell concentration and mean cell diameter was determined optically with a Cellometer Automated Cell counter (Nexelcom). Each replicate sample consisted of 1 x 10^5 cells in a microcentrifuge tube. For experimentation, a rinsing buffer of 1 X PBS with 3% FBS was prepared and used for all rinsing steps. All materials and cell samples were kept on ice throughout the staining procedure. For immunolabeling, samples were incubated with primary antibodies at ~ 0.5 μg in 150 μL of rinsing buffer for 40 minutes. For all cell lines, markers were targeted with primary monoclonal mouse antihuman IgG antibodies with corresponding isotype controls that consisted of: CD326/EpCAM (IgG2b, clone 9C4, BioLegend, San Diego, CA), HER1/EGFR (IgG1, clone AY13, BioLegend), CD44 (IgG1, clone BJ18, BioLegend), E-cadherin (IgG1, clone 67A4, BioLegend), erbB2/HER2 (IgG1,

clone 24D2, BioLegend), N-cadherin (IgG1, clone8C11, BioLegend), αVβ3 integrin (IgG1, clone 23C6, BioLegend), ICAM-1 (IgG1, clone HA58, eBiosciences, San Diego, CA), ER-α (IgG2a, clone F-10, Santa Cruz Biotechnology, Dallas, TX). Samples were then rinsed twice with rinsing buffer. Cells were then incubated with biotinylated goat anti-mouse IgG antibody (Vector Labs, Burlingame, CA) at a 1:400 dilution in rinsing buffer on ice for 40 minutes. Cells were rinsed twice and incubated with streptavidin-phycoerythrin at ~ 1 μg in 200 μL on ice for 20 minutes. Samples were rinsed three times and resuspended in ~ 200 μL for immediate analysis with flow cytometry.

4.2.3 Data Analysis

Data was calculated as mean ± standard error of the mean (n=3) for all marker quantification assays and cell diameter calculations. Standard error was used to as opposed to standard deviation due to the large variance in fluorescence within a single replicate. The standard error illustrates how our observation relates to the true mean of marker expression. Quantibrite PE bead calibration was performed every day of cell immunofluorescence data collection and fluorescence calibration values were collected using a 585/40 bandpass filter for red-orange detection. PE per cell values were calculated using a linear calibration curve (R^2 ~0.98) of PE molecules vs. fluorescence generated from the bead calibration for each on their respective days of collection. Statistical analysis consisted of a two-tailed student t-test performed in Matlab to calculate p-values.

4.3 Results

4.3.1 Image analysis

Morphological comparison of cell lines studied are shown by bright field images in Figure 4.1. The distinct morphology of the MDA-MB-231 basal like breast cancer cell line [99] from the other lines studied is present in the elongated, multipolar nature with minimal cell-to-cell contact. This morphology is characteristic of basal subtypes and is clearly present in the basal like tumor cells. In contrast, the luminal breast cancer lines MCF-7 and T-47D [100], and NSCLC line H358 exhibit much less elongation with tightly packed colonization highly favoring cell-to-cell contact. These traits are characteristic of the epithelial phenotype and commonly are minimally invasive. All cell types and diameters are summarized in Table 4.1.

Table 4.1: Summary of cell types analyzed in the study. Diameter and surface area calculations are reported as mean ± s.e.m.

Cell Type	Description	Diameter (μm)	Surface Area (μm^2)
MDA-MB-231	mammary adenocarcinoma	11.5 ± 0.3	415 ± 19
MCF-7	mammary adenocarcinoma	17.1 ± 0.4	922 ± 43
T-47D	mammary ductal carcinoma	14.5 ± 0.3	663 ± 34
A549	alveolar adenocarcinoma	15.0 ± 0.4	710 ± 38
H358	bronchioalveolar carcinoma	16.8 ± 0.5	890 ± 47
Peripheral Lymphocytes	Healthy PBMC	6.7 ± 0.1	142 ± 1
Peripheral Monocytes	Healthy PBMC	7.9 ± 0.1	197 ± 2
Peripheral Granulocytes	Healthy PBMC	8.2 ± 0.1	209 ± 1

Cell diameters for each cell line were obtained using a Cellometer automated counter (Nexcelom). Using regression analysis of cell line diameters with mean forward scatter in flow cytometry, the size of PBMC cells were estimated. For all cells a spherical model was assumed for surface area calculation.

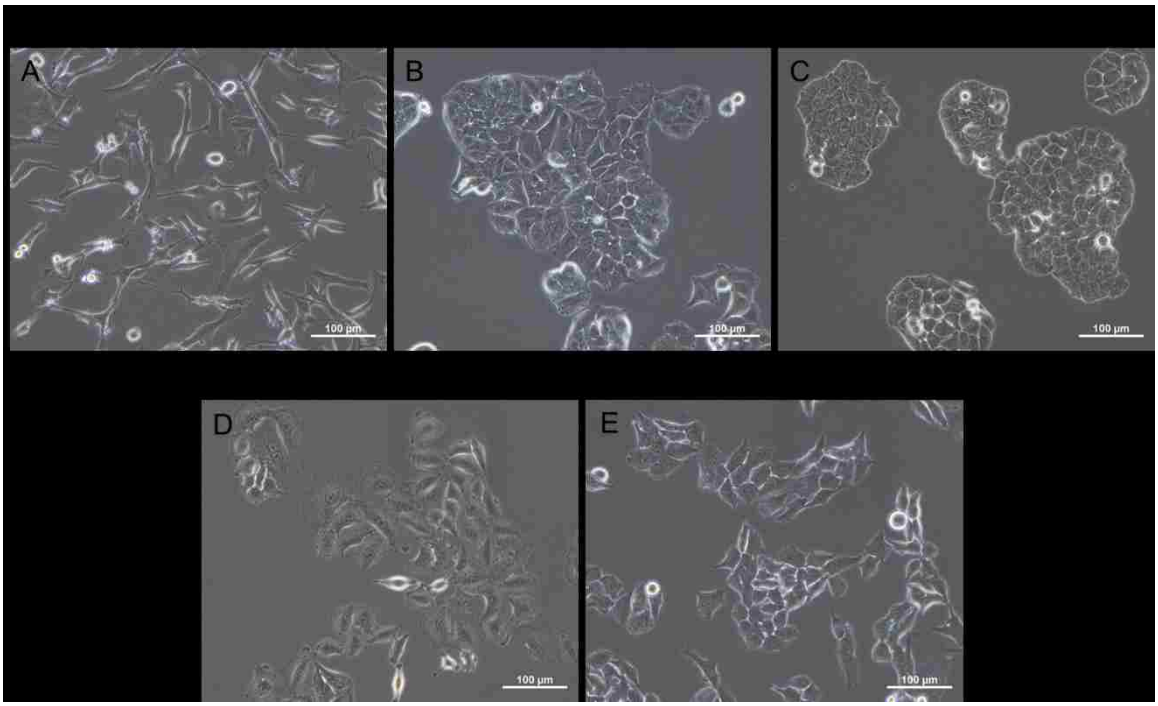

Figure 4.1: Representative bright field micrograph images of cultured breast cancer lines (MDA-MB-231, MCF-7, T-47D) and non-small cell lung cancer lines (A549, H358).

4.3.2 Flow cytometric analysis of surface markers

Quantitation of surface markers was done using QuantiBRITE PE beads with a SA-PE conjugate that served as a fluorescent reporter molecule for antigen expression. The indirect labeling method used here has minor amplification inherent within. Parallel comparison of direct staining with a biotinylated anti-EpCAM and a biotinylated anti-mouse secondary, both followed with SA-PE staining resulted in a 1.3-fold amplification of the secondary staining method shown in Figure 4.2. Although this amplification may overestimate the real number of target surface markers, secondary staining was performed to remain consistent with traditional immunolabeling in applications of CTC isolation. In these rare cell isolation strategies, amplification of labeling is often desired to further

separate positive from negative events. Consistent tagging was used for all markers on all cell lines to preserve relative expression levels.

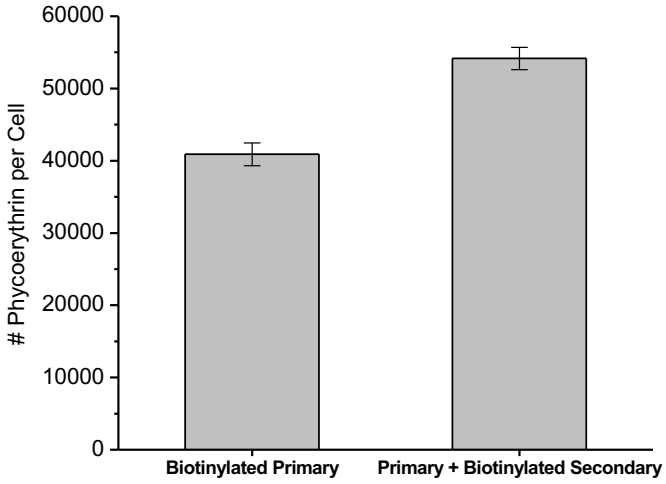

Figure 4.2: Phycoerythrin labeling per cell comparison for indirect staining conditions on viable A549 cells. Labeling conditions before streptavidin-phycoerythrin incubation were (left) covalently biotinylated mouse anti-human EpCAM and (right) mouse anti-human EpCAM + biotinylated goat anti-mouse.

Expression levels of the quantified markers varied drastically among the studied lines and is reported as fold over isotype controls showing expression over non-specific binding, as well as normalized against surface area for number of PE molecules per μm^2 on each cell type. These data are presented in Figures 4.3 and 4.4, respectively. Notably, the two lines possessing the more invasive morphologies, MB-MDA-231 and A549, are also the two that showed lower expression of EpCAM and E-Cadherin than the other three lines exhibiting more epithelial morphologies ($p < 0.001$, Figure 4.4). All statistical values are reported in Table 4.2 at the end of this chapter. MD-MBA-231 cells also showed higher expression of CD 44, EGFR and ICAM1 over MCF-7, T-47D, and H358 cell lines ($p < 0.01$). CD 44 was also expressed at significantly higher levels in A549 cells over MCF-7,

T-47D and H358 lines ($p < 0.01$). Integrin αVβ3 has an order of magnitude greater expression level for MB-MDA-231 than the other lines examined, registering ~30 PE molecules/μm^2 ($p < 0.001$). EGFR and ICAM1 showed relatively high expression, at least 100 PE molecules/μm^2, for all lines except MCF-7. These two markers are involved in many mechanisms that promote metastasis such as cell migration through the ECM and angiogenesis. Their increased expression has been linked to poorer prognoses [96, 101]. For breast cancer in particular ERα, PR and HER2 are markers used for subclassification of cancer as well as therapeutic targeting. All three breast cancer lines showed a slight increase in ERα expression over isotype controls (p-values< 0.05, Figure 4.3 A-C), and elevation in expression over NSCLC lines (p-values < 0.05) which showed virtually no ERα expression, with the exception of MCF-7 compared to A549 ($p=0.15$, Figure 4.4 D, E). HER2, however had relatively high expression in all lines of 50-100 PE molecules/μm^2.

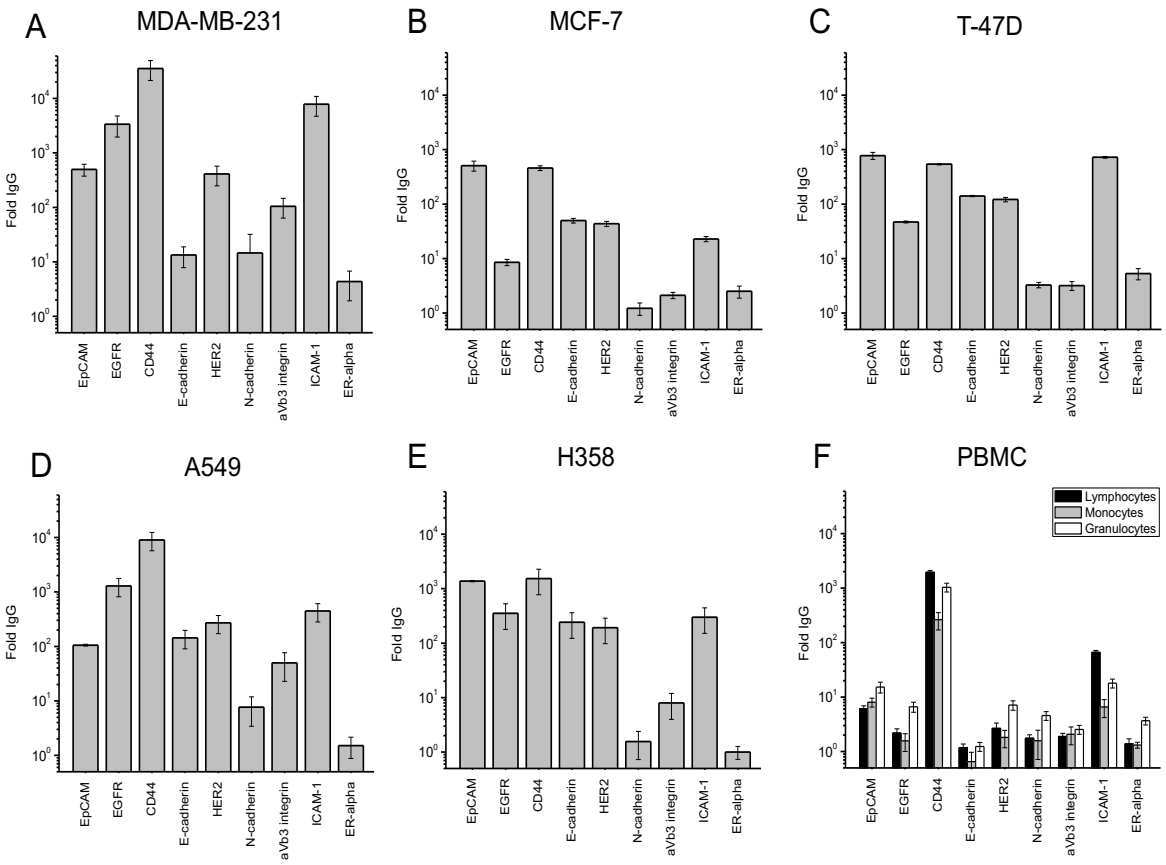

Figure 4.3: Summary of tumor marker expression on viable cells. Presented as fold over isotype controls for cancer lines and healthy peripheral blood mononuclear cells (PBMC) as quantified by flow cytometry analysis of a phycoerythrin reporter label.

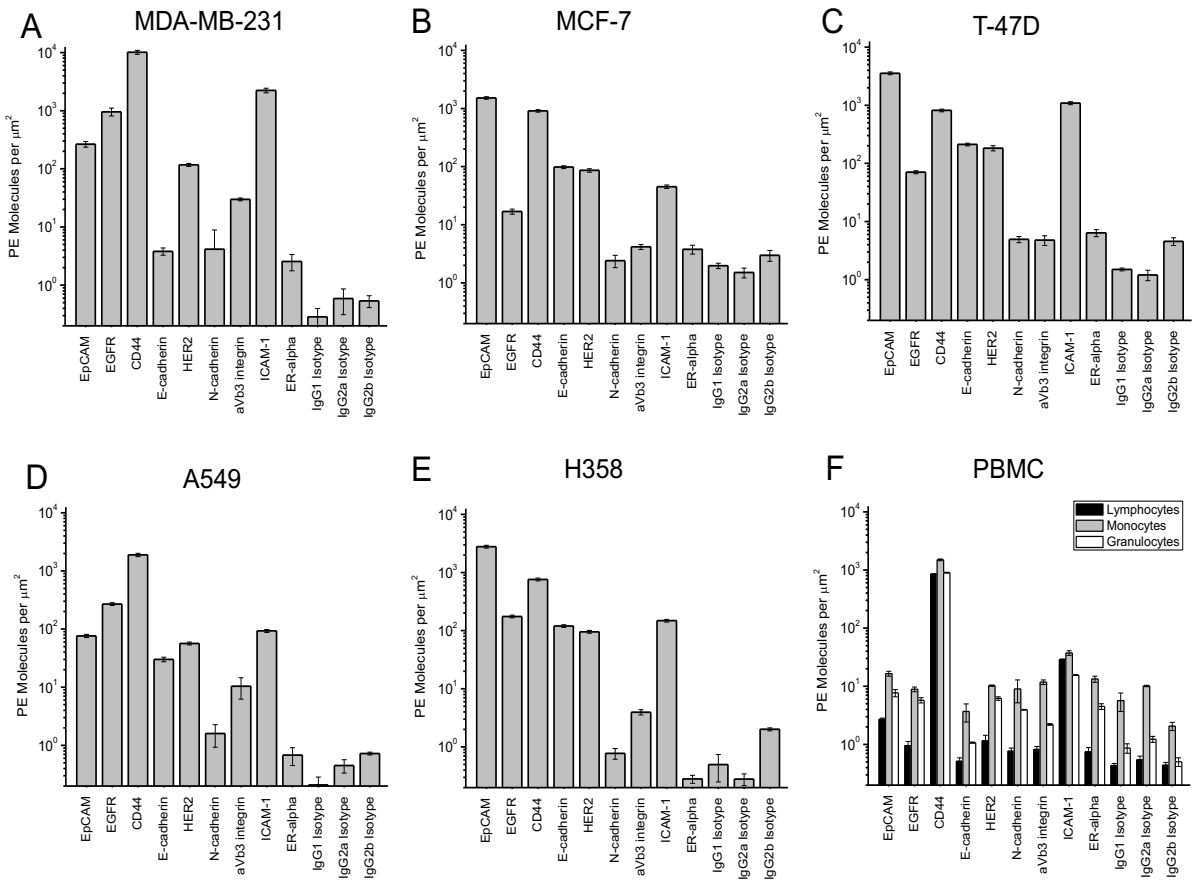

Figure 4.4: Summary of Phycoerythrin labeling density (# PE molecules/μm^2 of cell surface) for various tumor marker targeting conditions on viable cancer line cells and healthy PBMC.

For CTC isolation from peripheral blood, target markers must be chosen such that CTCs show clear distinction from PBMCs. Targeting markers that are highly expressed in both cell types effectively eliminates the ability to distinguish target cells within the population. Nucleated blood cells were fluorescently analyzed by flow cytometry with gating for the subtypes of leukocytes, monocytes, and granulocytes. Marker quantitation for each PBMC subtype was reported as fold over IgG (Figure 4.3F), and then as PE molecules/μm^2 after normalization to the size of each subtype (Figure 4.4F). These

estimates were in fair agreement with the literature [102, 103]. Relatively high staining is observed on PBMCs, especially with monocytes, which is somewhat expected due to their tendency for nonspecific binding. For further analysis, we report marker expression for each cell line over staining for monocytes specifically (Figure 4.5). CD 44 consistently showed high expression levels for all cancer cells studied, however would not be considered a suitable target due to high non-specific staining observed of CD 44 in PBMCs. Targeting CD 44 would likely result in a high occurrence of false positive events. The greatly attenuated expression of EpCAM for the more morphologically invasive lines of A549 and MB-MDA-231 would also likely produce false positives as a potential target.

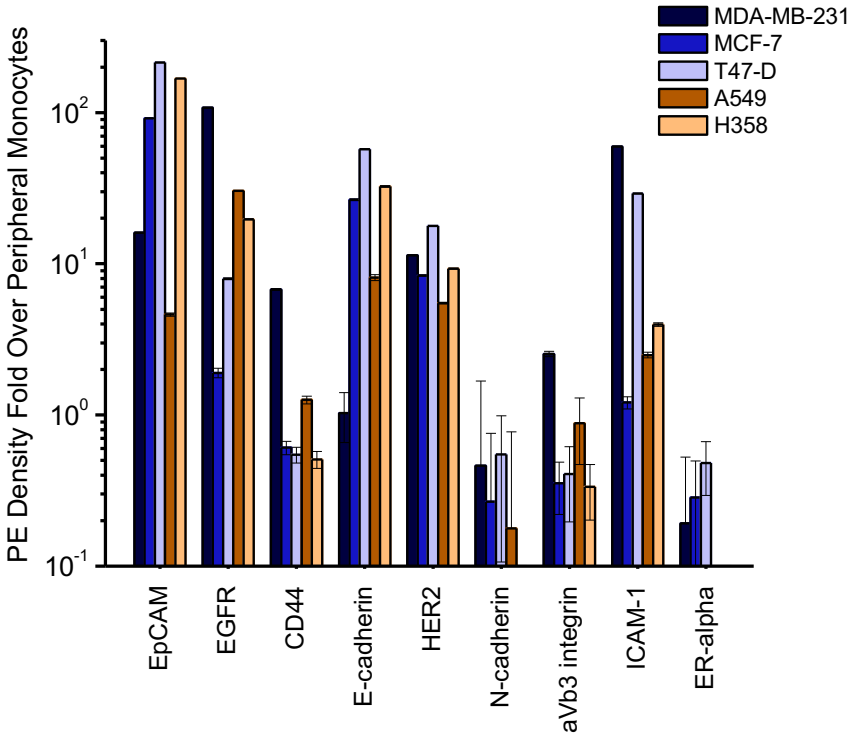

Figure 4.5: Summary of phycoerythrin labeling density of all cancer lines studied presented as fold expression over healthy monocytes from a peripheral blood sample.

4.4 Discussion

Here we have reported expression levels of commonly studied metastatic associated cancer biomarkers through antibody recognition for two breast cancer and three NSCLC lines in comparison to PBMC. In the literature, very little quantitative information has been reported for surface markers available for viable cell binding. While quantitative assays may provide prognostic or therapeutic information with positive/negative reporting, they may not be adequate for portraying highly dynamic surface expression of many tumor cells for isolation targeting [104-106]. For viable tumor cells the isolation ability is critically dependent on the unique surface expression of target cells over other cells within the heterogenous population. We propose these results as a significant step toward highly effective isolation strategies through informed target marker selection in the isolation community.

Our results show breast cancer marker expression consistent with the basal or luminal characteristics of each subtype. Basal subtypes are often more invasive and show less cell-to-cell contact than luminal cancers which are more epithelial-like [100, 107]. The basal-like MDA-MB-231 showed elevated levels of metastatic/mesenchymal associated markers CD44, N-cadherin, αV-β3 integrin, ICAM-1, as well as upregulation of EGFR as is common in basal-like tumors (Figure 4.3A) [107]. These cells also showed less expression of the epithelial markers EpCAM and E-Cadherin compared to the luminal T-47D and MCF-7 lines. Elevation of these mesenchymal markers are indicative of the more metastatic cancers as they play key roles in migration, invasion and angiogenesis [108]. Invasive cells of this nature are problematic for current isolation strategies that largely favor the EpCAM+ cells. Highly invasive cells of this nature are more prone to go

undetected in isolation methods due to epithelial marker expression lower than determined threshold.

An interesting result was seen for ERα expression in comparing the basal and luminal subtypes. MDA-MB-231 cells expressed similar surface densities of ERα compared to MCF-7 and T-47D. Since this study aimed to determine antigen surface densities on intact viable cells, differing results may arise from the incorporation of intracellular expression levels in literature. The antibody chosen for ERα targeting (clone F-10, Santa Cruz Biotech) targeted the C-terminal ligand binding domain and although these receptors show presence in the plasma membrane, they are largely a nuclear receptor [109]. While intracellular incorporation may be relevant in some applications, it holds no benefit for isolation strategies based on surface binding.

This study offers insight into the expression levels of several metastatic associated biomarkers including CD 44, N-Caderhin, ICAM1 and integrin αVβ3 as potential target markers [91, 96, 110]. Poorly expressed surface markers clearly serve little utility in functional isolation, along with markers that share high expression with that of PBMC cells. We found that both N-cadherin and integrin αVβ3 were upregulated on MDA-MB-231 and A549 lines. However, their utility as potential markers was diminished by the fact that expression density was still approximately equal to or below that found on peripheral monocytes (Figures 4.4F and 4.5). Additionally, CD44 was consistently high for all cancer lines (Figure 4.5) as well as PBMCs. All cancer lines showed expression of a factor of nearly 1 or below that found on monocytes except MDA-MB-231 that retained a seven-fold increase over monocytes (Figure 4.5). Because these markers show expression similar to that of peripheral monocytes, they likely would serve poor targets to distinguish CTCs.

Further study may be warranted for the expression of N-Cadherin due to the phenomenon known as the 'cadherin switch' in which E-Cadherin expression is downregulated while N-Cadherin is upregulated is observed *in vivo* upon cytokine stimulation [88, 111, 112]. This increased N-Cadherin expression is correlated with more invasive phenotypes and could potentially allow N-Cadherin to serve as a possible target. Our results indicate ICAM1 as a potential target for isolation of CTCs. ICAM1 is a cell adhesion molecule that plays a significant role in migration, and has been recently been classified as a mesenchymal cell marker [113-115]. A recent study has shown that increased populations of ICAM1 upregulated CTCs correlated to poorer prognosis [96], further suggesting the potential utility of it as a target.

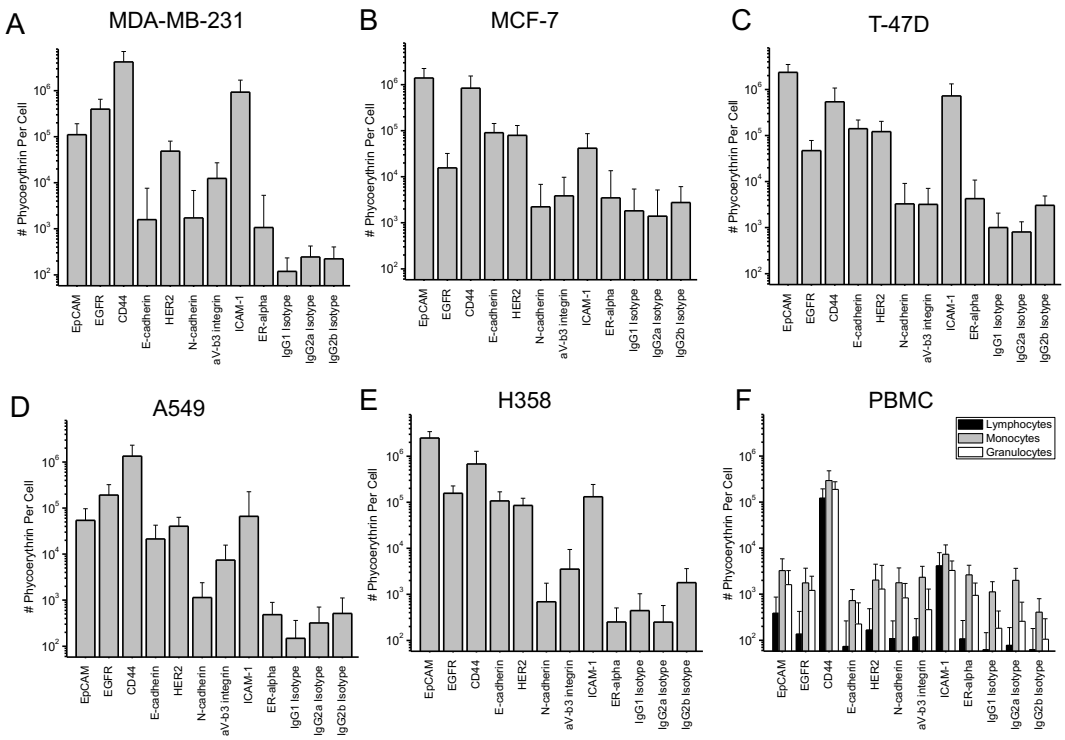

Figure 4.6: Summary of phycoerythrin labeling per cell for all markers and cell types.

Error bars represent the standard error of events collected by flow cytometry.

In conclusion, we have reported the surface expression of common cancer associated biomarkers on three breast cancer and two NSCLC tumor model cell lines. This information is critical in any antigen-based method for functional CTC isolation. Expression levels observed in this study shed some light on a key reason for poor performance in many isolation studies. These results also show the drastic variability in marker expression within cancer subtypes illustrating the need for a more dynamic approach to CTC isolation as opposed to one target epithelial marker. The intense variability shown in Figure 4.6 for cell events within each replicate in the staining protocol further supports the shortcomings in isolation methods based primarily on the expression of a single epithelial marker. This is likely due to the inherent variability within the cultured

cells, as well as the deviations from a mean affinity for each antibody used. Any antibody based-assay should carefully consider the variation in antibody affinity across suppliers when designing and interpreting methodologies and collected data. Further, heterogeneity in marker expression increases even more as some tumor cells undergo the phenotypic change known as the epithelial to mesenchymal transition (EMT) [72]. These invasive subsets are among the most dangerous and the most difficult to detect due to the lack of EpCAM expression. One possible approach to the highly varied surface expression is to use a mixture of antibodies to target multiple characteristic surface markers. For example, Yu et al. developed a method to target patient-derived breast cancer CTCs with a cocktail of EpCAM, EGFR, and HER2 antibodies on an affinity based microchip platform [104].

Table 4.2: Summary of student t-test calculations for surface marker data.

Line 1	Line 2	Marker	Data Type	P-value
MDA-MB-231	MCF-7	CD44	Label Density	0.0017
MDA-MB-231	T-47D	CD44	Label Density	0.0016
MDA-MB-231	H358	CD44	Label Density	0.0016
MDA-MB-231	MCF-7	N-cadherin	Label Density	0.588
MDA-MB-231	T-47D	N-cadherin	Label Density	0.8
MDA-MB-231	H358	N-cadherin	Label Density	0.34
MDA-MB-231	MCF-7	ICAM-1	Label Density	0.002
MDA-MB-231	T-47D	ICAM-1	Label Density	0.0059
MDA-MB-231	H358	ICAM-1	Label Density	0.0022
MDA-MB-231	MCF-7	EpCAM	Label Density	5.80E-07
MDA-MB-231	T-47D	EpCAM	Label Density	3.57E-05
MDA-MB-231	H358	EpCAM	Label Density	7.27E-08
MDA-MB-231	MCF-7	E-cadherin	Label Density	2.20E-04
MDA-MB-231	T-47D	E-cadherin	Label Density	1.17E-05
MDA-MB-231	H358	E-cadherin	Label Density	3.99E-06
MDA-MB-231	MCF-7	EGFR	Label Density	7.50E-03
MDA-MB-231	T-47D	EGFR	Label Density	8.40E-03
MDA-MB-231	H358	EGFR	Label Density	1.00E-02
A549	MCF-7	CD44	Label Density	9.20E-04
A549	T-47D	CD44	Label Density	9.70E-04
A549	H358	CD44	Label Density	1.10E-03
A549	MCF-7	EpCAM	Label Density	1.07E-04
A549	T-47D	EpCAM	Label Density	1.60E-04
A549	H358	EpCAM	Label Density	4.27E-05
A549	MCF-7	E-cadherin	Label Density	1.23E-05
A549	T-47D	E-cadherin	Label Density	4.80E-08
A549	H358	E-cadherin	Label Density	3.20E-06
MDA-MB-231	MCF-7	aV-b3 integrin	Label Density	4.15E-05
MDA-MB-231	T-47D	aV-b3 integrin	Label Density	3.74E-06
MDA-MB-231	H358	aV-b3 integrin	Label Density	5.60E-05
MDA-MB-231	lymphocyte	aV-b3 integrin	Label Density	2.30E-04
MDA-MB-231	monocyte	aV-b3 integrin	Label Density	2.70E-05
MDA-MB-231	granulocyte	aV-b3 integrin	Label Density	2.80E-04
MDA-MB-231	isotype	ER-alpha	Expression	3.80E-02
MDA-MB-231	isotype	HER2	Expression	4.15E-04
MCF-7	isotype	ER-alpha	Expression	1.30E-02
MCF-7	isotype	HER2	Expression	7.50E-04
T-47D	isotype	ER-alpha	Expression	5.50E-03
T-47D	isotype	HER2	Expression	2.70E-03
lymphocyte	isotype	CD44	Expression	1.53E-05
lymphocyte	isotype	ICAM-1	Expression	2.05E-04
monocyte	isotype	CD44	Expression	3.76E-04
monocyte	isotype	ICAM-1	Expression	4.82E-04
granulocyte	isotype	CD44	Expression	7.66E-05
granulocyte	isotype	ICAM-1	Expression	1.33E-07

Line 1	Line 2	Marker	Data Type	P-value
MDA-MB-231	monocyte	EpCAM	Label Density	3.80E-03
MDA-MB-231	monocyte	E-cadherin	Label Density	8.97E-01
MDA-MB-231	monocyte	EGFR	Label Density	7.40E-03
A549	monocyte	EGFR	Label Density	1.81E-05
H358	monocyte	EGFR	Label Density	1.80E-08
MDA-MB-231	monocyte	CD44	Label Density	1.80E-03
MCF-7	monocyte	CD44	Label Density	9.68E-04
T-47D	monocyte	CD44	Label Density	1.00E-03
H358	monocyte	CD44	Label Density	1.30E-03
A549	monocyte	CD44	Label Density	2.00E-03
MDA-MB-231	monocyte	ICAM-1	Label Density	2.00E-03
MCF-7	monocyte	ICAM-1	Label Density	3.41E-02
T-47D	monocyte	ICAM-1	Label Density	2.44E-04
H358	monocyte	ICAM-1	Label Density	1.05E-05
A549	monocyte	ICAM-1	Label Density	4.45E-05
MDA-MB-231	monocyte	aV-b3 integrin	Label Density	2.70E-05
MCF-7	monocyte	aV-b3 integrin	Label Density	3.00E-03
T-47D	monocyte	aV-b3 integrin	Label Density	9.76E-04
H358	monocyte	aV-b3 integrin	Label Density	3.00E-03
A549	monocyte	aV-b3 integrin	Label Density	7.20E-01
MDA-MB-231	monocyte	N-cadherin	Label Density	2.40E-01
MCF-7	monocyte	N-cadherin	Label Density	9.30E-02
T-47D	monocyte	N-cadherin	Label Density	2.00E-01
H358	monocyte	N-cadherin	Label Density	6.50E-02
A549	monocyte	N-cadherin	Label Density	7.40E-02
MDA-MB-231	A549	EpCAM	Label Density	6.40E-03
MDA-MB-231	A549	EGFR	Label Density	1.40E-02
MDA-MB-231	A549	CD44	Label Density	1.90E-03
MDA-MB-231	A549	E-cadherin	Label Density	1.40E-03
MDA-MB-231	A549	HER2	Label Density	8.20E-04
MDA-MB-231	A549	N-cadherin	Label Density	4.48E-01
MDA-MB-231	A549	aV-b3 integrin	Label Density	8.80E-02
MDA-MB-231	A549	ICAM-1	Label Density	2.00E-03
MDA-MB-231	A549	ER-alpha	Label Density	4.30E-02
MDA-MB-231	MCF-7	ER-alpha	Label Density	1.10E-01
MDA-MB-231	T-47D	ER-alpha	Label Density	5.00E-03
MCF-7	T-47D	ER-alpha	Label Density	1.50E-02
MDA-MB-231	MCF-7	HER2	Label Density	7.77E-04
MDA-MB-231	T-47D	HER2	Label Density	1.60E-02
MCF-7	T-47D	HER2	Label Density	6.80E-03
MDA-MB-231	A549	ER-alpha	Expression	0.05
MDA-MB-231	H358	ER-alpha	Expression	0.047
MCF-7	A549	ER-alpha	Expression	0.15
MCF-7	H358	ER-alpha	Expression	0.016
T-47D	A549	ER-alpha	Expression	0.007
T-47D	H358	ER-alpha	Expression	0.0066

CHAPTER 5. COMMERCIALIZATION OF ASL THROUGH THE USE OF FITC FOR PHOTOINITIATION

5.1 Introduction

Eosin Y is among the most common visible light initiators for radical polymerization in aqueous media [38, 41, 44, 116, 117]. It has been widely used in the formation of cell laden gel due to its ability to generate radical species with low intensity visible light while showing minimal cytotoxicity [118]. Visible light photopolymerization eliminates the possibility of UV mediated damage when dealing with live cells [37]. Eosin Y is a xanthene derivative photosensitizer that is excited by absorption of light at 530 nm. Radical generation is achieved through excitation of the eosin molecule where it undergoes an intersystem crossing to yield a triplet excited state. In the presence of a tertiary amine coinitiator, commonly triethanol amine (TEA), electron transfer from the amine to the eosin molecule followed by hydrogen abstraction by eosin yields two neutral radical species [40]. Of these two, the TEA radical is much more reactive toward the acrylate functional groups [38, 41] that are commonly used in biologically compatible hydrogel formation. While the TEA radical initiates chain propagation, a neutral eosin molecule is regenerated through a disproportionation reaction where once back in the ground state, can again undergo excitation to form more radicals. The cyclic regeneration of eosin makes it highly valuable in systems that contain radical quenching species, or limited initiator present. It has been shown to generate hydrogel polymerization in systems containing 1000-fold greater inhibitor concentration over initiator [119]. Eosin has also commonly been functionalized to surfaces for generation of thin hydrogel films on cellular surfaces

[44], as well as protein conjugation on micro arrays for highly sensitive biodetection of ultra-low analyte density [66, 120-123]. Figure 5.1 below shows the polymerization reaction scheme with cyclic regenerating photoinitiators.

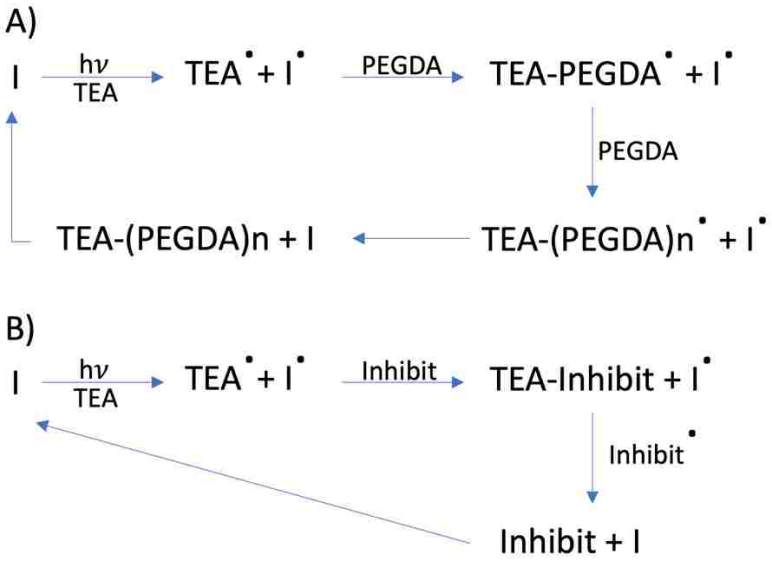

Figure 5.1: Reaction schematic of A) radical polymerization and regeneration of photoinitiator (I = eosin Y or fluorescein), and B) initiator ability to consume inhibiting species and regenerate.

Our lab has developed a method of surface polymerization that utilizes eosin functionalized cells for nano thin film generation [33]. This technology has applications in rare cell isolation [33], immunoprotection [124], and is being studied for mechanical protection against shear forces in 3D bioprinting. Many cell encapsulation strategies use aqueous cell suspensions with eosin in solution to form cell laden bulk gels [118], or microscale coatings [116, 125]. Our lab uses cell membrane proteins as targets to highly specifically functionalize cellular surfaces with eosin through antibody recognition [33]. When suspended in a monomer solution containing TEA and irradiated, localized polymerization occurs only near the membrane of initiator labeled cells. This process yields

individually encapsulated cells in an ~100 nm thick hydrogel film while retaining high cell viability [33]. A limitation in this technology is the lack of commercially available eosin conjugates to common biorecognition molecules. Currently researchers must prepare their own eosin conjugates to achieve cell surface immobilization [66].

Fluorescein is another molecule that is part of the family of xanthene photosensitizers [38]. Like eosin, fluorescein can undergo the same photoinitiation mechanisms with a tertiary amine coinitiator to generate active radicals [38, 41, 119]. Figure 5.2 below shows the structural similarities between eosin and fluorescein.

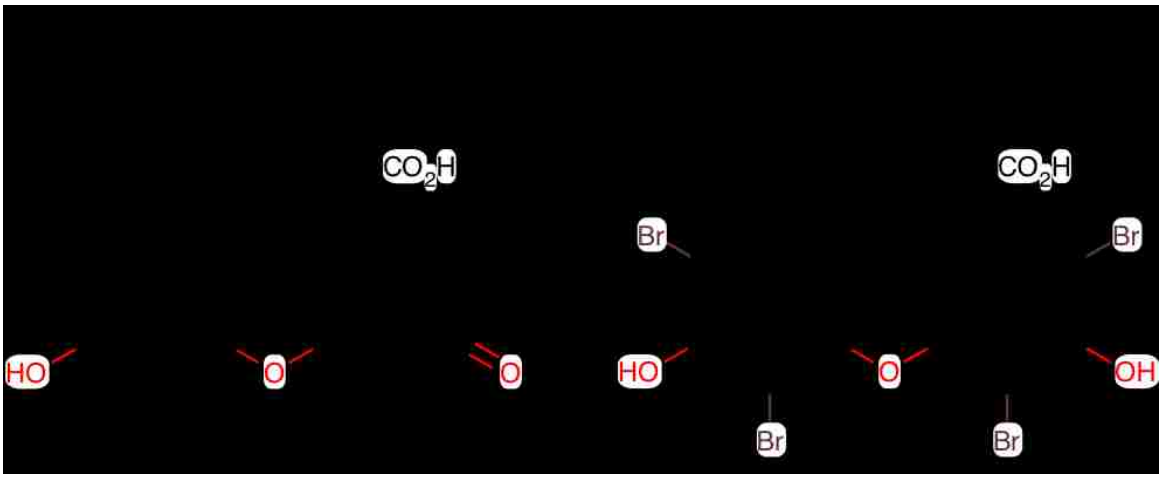

Figure 5.2: Chemical structures of eosin Y and fluorescein.

While eosin has been extensively studied in radical polymerization [38, 40, 116, 119, 125-129], fluorescein has generally shown comparative results [119, 130]. While fluorescein possesses similar abilities of cyclic regeneration for continued radical production, it has been shown to be less effective at achieving gelation and also has lower sensitivity requiring a greater presence or surface density than that of eosin [119, 130].

In this study we seek to directly compare the ability of fluorescein and eosin to generate thin films. Although eosin and fluorescein have been studied simultaneously on polymerization

ability [38, 119, 130], the eosin-5-isothiocyantate (EITC) and commercially available fluorescein-isothiocyante (FITC) have not been evaluated under the cytocompatible conditions of aqueous media at neutral pH with decreased coinitiator concentration. We first compare film generation of FITC and EITC on protein printed micro array slides which serve as a model for the cell surface. Serial dilutions of printed protein afford sensitivity determinations and film thickness analysis across a range of initiator surface densities. These micro array slides also offer great reproducibility that is not readily observed on living biological substrates. We then compare these initiators on living substrates. Epidermal growth factor receptor (EGFR) was targeted on the surface of A549 cells for initiator immobilization and subsequent hydrogel encapsulation. Hydrogel encapsulation was determined by hypotonically challenging the coated populations. Complete hydrogel coatings of sufficient thickness provide membrane reinforcement against swelling and lysis in hypotonic conditions. We show that FITC is capable of generating films similar to that of ETIC on both micro arrays and living cells. As FITC is >10-fold cheaper than EITC by mass and is widely commercially conjugated to biorecognition molecules, this work presents an exciting step forward in translating our technology to a more standardized process with a range of applications.

5.2 Chemical structures of eosin Y and fluorescein.

5.2.1 Micro array printing

Protein printed micro array slides were prepared as described in Chapter 3.5 with a larger range of biotin-BSA (bBSA) concentrations. A total of 24 spots were printed at two locations on each slide to be centered in the Whatman Chip Clip well. Two spots of each of the twelve bBSA solution concentration were printed on each slide. Serial dilutions of 1000, 400, 160, 64, 25.6, 10.2, 4.1, 1.64, 0.66, 0.26, 0.1, and 0 μg bBSA/mL were used.

5.2.2 Micro array polymerization

Polymerization on micro array glass slides was done as described in Chapter 3.6, with minor changes in component concentrations as noted here. Monomer formulations contained 420 mM PEGDA-575, 210 mM triethanol amine (TEA) and 35 mM vinyl pyrrolidinone (VP) in deionized water. Cytocompatible conditions were achieved through the use of PBS as a solvent, pH adjustment with 1.2 M hydrochloric acid to 7.3-7.5, and lowering the concentration of TEA by 10-fold to 21 mM. Monomer solutions were gently bubbled with ultra-pure nitrogen to remove excess oxygen from solution. Irradiation was done at 20 or 30 mW/cm^2 using a collimated LED lamp (M530L3) for 10 min.

5.2.3 Fluorescent calibration using Cy3

SA-Cy3 conjugates were labeled on to micro array slides identically to SA-EITC and SA-FITC as described in Chapter 3.8. Micro array scans for fluorescence were done using an Affymetrix 428 array scanner. Fluorescent intensities were obtained with excitation from 532 nm laser line and detection with a 570 nm centered band pass filter. Fluorophore surface density was determined using a Cy3 calibration slide (Full Moon Biosystems). This calibration slide contained highly accurate Cy3 surface density for 28 values at 2-fold dilution with 12 replicates of each. Using the same scanning conditions, a calibration curve was generated and used to calculate surface density of bound SA-Cy3 conjugates.

5.2.4 Surface polymerization of A549 cells

Cells were cultured and harvested as described in Chapter 3.2. Immunolabeling of A549 cells was done using a biotinylated mouse anti-human EGFR primary antibody at a

1:100 dilution in blocking buffer of PBS supplemented with 3% fetal bovine serum (FBS). 200 μL of primary antibody were incubated with 1.5 million cells for 40 min on ice. Cells were then washed 2x with blocking buffer. Cells were then labeled with SA-EITC as described in Chapter 3.8. Monomer formulations for use with cells contained PEGDA 3400 (synthesized as reported [33]) for increased cytocompatibility over that of PEGDA 575 as generally higher molecular weight PEGDA monomers show decreased cytotoxicity [131]. PEGDA 3400 was used at 25 wt/v% with 21 mM TEA, 35 mM VP in PBS with final pH adjusted to 7.3-7.5. Monomer solution was bubbled with humidified ultra-pure nitrogen for 10 min prior to use to remove excess dissolved oxygen. Initiator labeled cells were polymerized as described in Chapter 3.9. Briefly, cells were suspended in 350 μL of monomer solution and placed into the well of a Whatman chip clip containing a standard microscope slide. The chip clip was placed into a polymerization chamber fabricated from two polystyrene petri dishes. The chamber was purged with nitrogen for 5 mins before, and for 10 mins during irradiation. The sample was irradiated at 30 mW/cm^2 for 10 min. Cells were then collected and washed 2x in PBS for further analysis.

Cell polymerizations using FITC as a photoinitiator were initially labeled with a primary antibody as described above. Cells were then labeled with a commercially available, FITC conjugated, horse anti-mouse secondary antibody (Vector Labs). Incubation of cells in 200 μL of the FITC secondary antibody at a 1:100 dilution was done on ice for 40 mins. Cells were then washed in PBS and polymerized as described above for EITC labeled cells.

5.3 Results and Discussion

5.3.1 Spectral Analysis of EITC and FITC

For experimental consistency, one lamp centered at ~530 nm was used for all polymerization experiments that has previously been shown to be effective with eosin [19, 33, 124, 132]. There are a number of xanthene dye derivatives that have been shown to absorb light in the visible range. Many of these molecules can also undergo similar mechanisms of radical generation in the presence of a tertiary amine. The absorbance and intersystem crossing quantum yield of a molecule is highly dependent on the substitution of the molecule, which gives rise to a range of fluorescent dyes [38]. This is evident in comparing the maximum absorbance of eosin (~530 nm) and fluorescein (~495 nm).

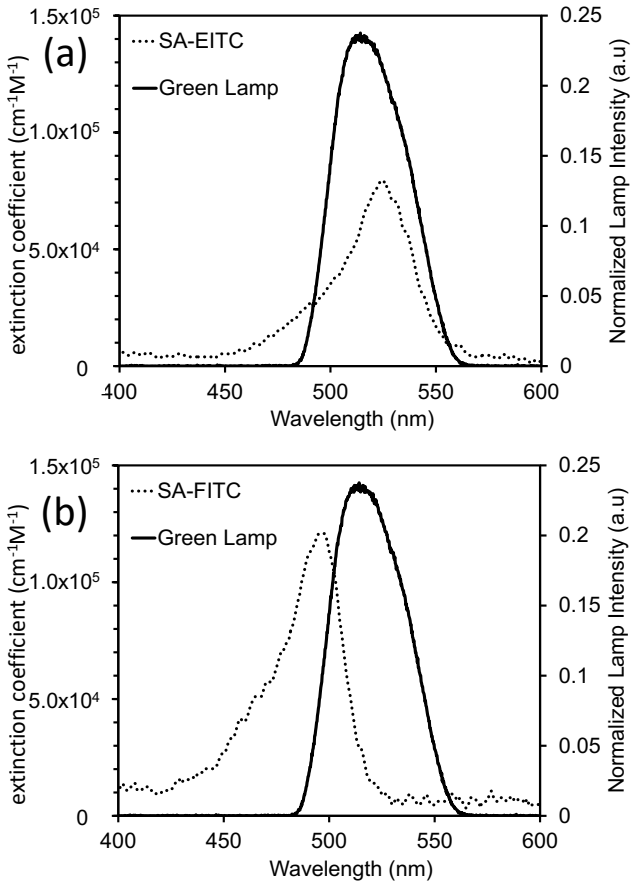

Figure 5.3: Analysis of photoinitatior absorbance spectral overlap for (a) SA-FITC and (b) SA-EITC with a Thorlabs collimated LED emitting green light. Lamp spectra obtained from manufacturer.

Due to the difference in the maximum absorbance wavelength of these two initiators, we first quantify the spectral overlap of the lap with each dye. Extinction coefficients were calculated using Beer-Lambert law with absorbance data collected by a UV/Vis spectrophotometer (Nano Drop 2000). Normalized emission data from the LED and extinction coefficients are plotted in Figure 5.3, and spectral overlap was quantified using numerical integration. Extinction coefficients of EITC and FITC agree with literature values for eosin Y and fluorescein alone indicating that conjugation to biomolecules have

little effect on their spectral properties. Integration reveals the relative amount of light absorbed by each species assuming identical concentration. Calculated values show that EITC absorbs ~48% more optical energy than FITC. This is not surprising considering the maximum absorbance of EITC is almost directly in alignment with the maximum emission of the lamp. The absorbance curve of FITC is shifted toward the shorter wavelengths as compared to the lamp emission. Absorbance is not the only factor involved in radical generation. Triplet quantum yield, as well as regeneration rate are both very important factors that greatly affect the gelation rate of the polymer system [38, 119, 130]. However, the spectral mismatch of FITC compared to EITC with the chosen lamp presents an inherent skew towards the performance of the EITC system.

5.3.2 Polymerization with micro arrays

Micro array polymerization allowed us to compare the film generating ability of the two initiators in a highly controlled environment that mimics the cellular surface. Both non-cell friendly microassay and cell compatible polymerization conditions were studied on a range of initiator loading densities. The high binding affinity of the biotin/ streptavidin system [133] allowed us to confidently control the initiator loading by varying the biotin concentration within the printed solutions.

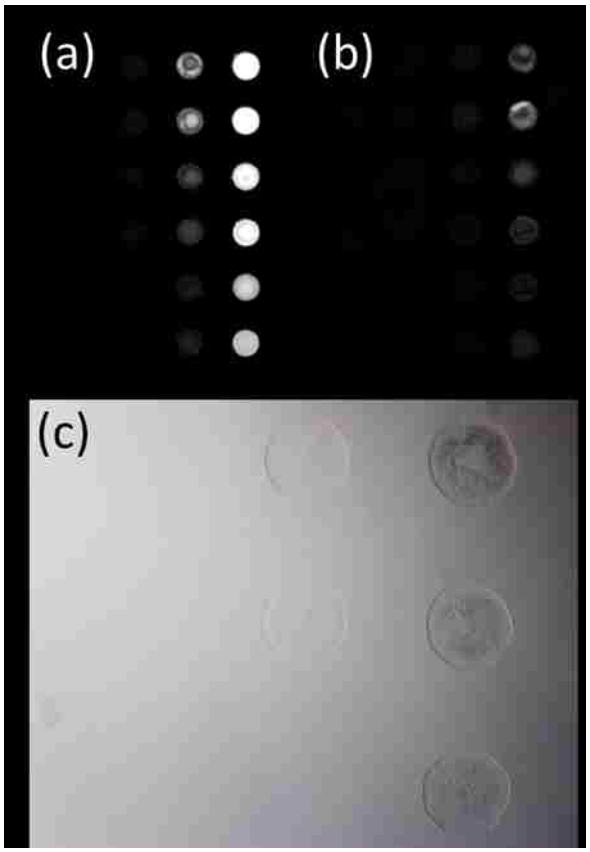

Figure 5.4: Specific polymerization of photoinitiator tagged micro arrays. (A) Grayscale fluorescence scanner image of SA-EITC bound to biotin-BSA printed micro arrays. Scan at 50 dB gain with 532 nm excitation and 551/25 nm detection with bandpass filter. (B) Grayscale fluorescence scanner image of SA-FITC bound to biotin-BSA printed micro arrays. Scan at 50 dB gain with 532 nm excitation and 551/25 nm detection with bandpass filter. (C) Bright field optical microscopy example image of a micro array sample tagged with SA-FITC after photopolymerization at 30 mW/cm^2 for 10 minutes.

Local gelation and varying of specific binding to only bBSA printed areas can be seen in Figure 5.4. The variation in biotin print concentration is observed for both EITC and FITC labeling in Figure 5.4a and 5.4b respectively. Figure 5.4c shows local film generation in

conditions that are conducive to high cell viability. Although this polymerization system has been used in rare protein detection with highly sensitive gelation [44], parameters have been modified to support living cell applications. Solution tonicity, pH, component concentrations, irradiation time and intensity, all must be considered when using living cell systems. To account for viability, PBS was used as the monomer solvent, pH was adjusted to physiological levels (~7.5), and the toxic component of TEA was reduced by 10-fold from 210 mM to 21 mM.

Thickness of generated film for EITC and FITC under cell friendly conditions under two different radiation intensities can be seen in Figure 5.5. Film thickness was recorded by profilometry. The highest film generation of ~145 nm average thickness occurred with 30 mW/cm^2 radiation of SA-EITC functionalized spots at the highest bBSA densities.

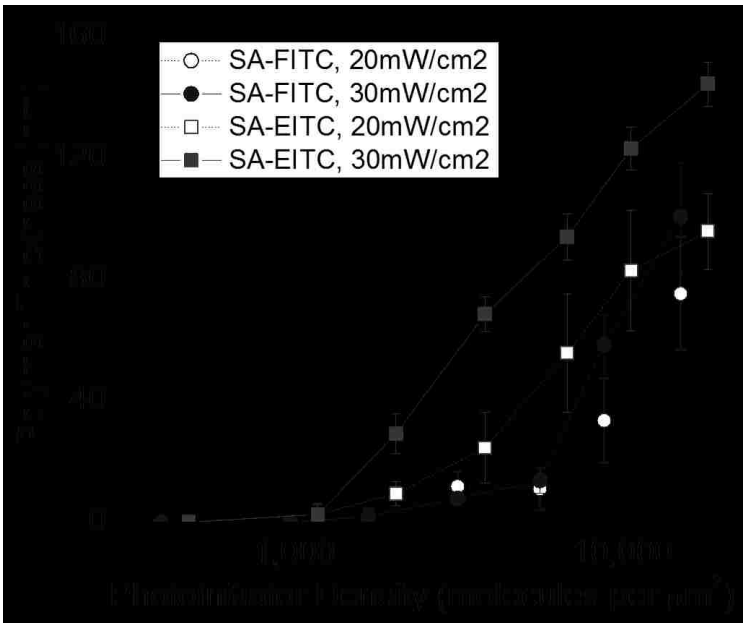

Figure 5.5: Comparative analysis of polymer gelation thickness vs. photoinitiator density for SA-FITC and SA-EITC tagged micro array samples. Analysis was conducted with cell compatable conditions consisting of 420 mM PEG-diacrylate, 21 mM triethanol amine, 35 mM vinyl pyrrolidone, in phosphate buffered media (pH=7.5) with a constant reaction time of 10 minutes.

The EITC labeling density for these spots was ~18,000 molecules/μm^2, and yielded film generation comparable to previously published works with similar conditions [124, 132]. Increased radiation intensity generally showed increased film generation as expected for both EITC and FITC. Increased radiation likely increases the influx of active radicals for faster gelation at similar initiator loading, especially at the higher initiator surface densities. While neither initiator showed any appreciable film generation at the lowest print concentrations, EITC does show a lower threshold for initial gelation indicating a higher sensitivity. Lower threshold limits were ~1,200 molecules/μm^2 for EITC and ~1,800 molecules/μm^2 for FITC.

Film generation by FITC initiation was generally lower than EITC for the same loading conditions. However, FITC was still able to record appreciative polymer formation even with the discussed disadvantage of spectral mismatch. At high initiator loading and high intensity, FITC was able to generate films that averaged ~100 nm, which is very different than previously reported studies for fluorescein in aqueous conditions [38]. These reports have stated that quantum yield of the triplet state and radical generation is much lower for fluorescein than that of FITC. However, a large difference in our study is the use of the 530 nm LED. Other studies have used sources with a very narrow bandwidth such as laser lines that are either well above 500 nm or near 400 nm [130]. As we have calculated that FITC absorbs ~48% less light than EITC with our relatively broad bandwidth source, absorption would decrease drastically with decreased bandwidth. These studies suggest that a light source that is further aligned with the absorption profile of FITC would considerably increase absorption and radical generation for initiation of polymerization.

This study also evaluated the film generation in 'unconstrained' conditions which are not conducive to cell viability. Coinitiator concentration was increased 10-fold, pH was not adjusted, and the solvent was not buffered. Figure 5.6 shows the drastically increased film generation of the FITC initiated unconstrained system. Sensitivity is increased nearly 2-fold to a threshold of ~1000 molecules/μm^2, and film generation rivals that of previously reported values for EITC initiated systems. This suggest the possibility of the commercially available FITC bioconjugates for use in sensitive biorecognition assays.

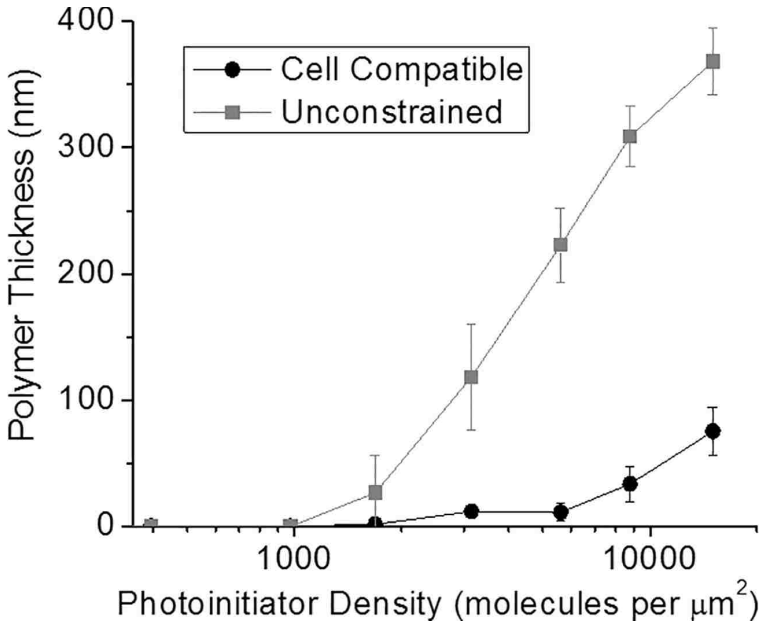

Figure 5.6: Comparison of polymer gelation thickness vs. photoinitiator density with cell compatible and unconstrained formulations and FITC photoinitiation. All samples were irradiated with 20mW/cm^2 of green light (530 nm LED lamp, ThorLabs) for 10 minutes. Cell compatible = 420 mM PEG-diacrylate, 21 mM triethanol amine, 35 mM vinyl pyrrolidone, in phosphate buffered media (pH=7.5). Unconstrained= 420 mM PEG-diacrylate, 210 mM triethanol amine, 35 mM vinyl pyrrolidone in deionized water.

5.3.3 Cell encapsulation using FITC initiated systems

For comparison of EITC and FITC on living cell encapsulation, epidermal growth factor receptor (EGFR) was targeted on the surface of the non-small cell lung cancer line, A549. A549 cells have been shown to overexpress EGFR, which serves as a prototypic model for FITC initiation in a live cell system. Cells were first labeled with mouse antibodies against human EGFR followed by initiator labeling with either SA-EITC or a FITC labeled secondary antibody. Initiator labeling was confirmed by green fluorescence

using flow cytometric analysis. Polymerization was carried out with cell friendly conditions and viability was assessed by MTT assay shown in Figure 5.7 (figure caption on page following figure). Viability following polymerization was maintained for both initiating systems. While different cell lines may show different susceptibility to toxins, these data show that FITC, like EITC, is generally compatible for surface polymerization on living cells. Polymerized cells were then subjected to hypotonic conditions where uncoated cells are lysed, while cells possessing a complete coating are protected from the harsh conditions [21, 33]. The FITC initiated system shows very comparable results of ~20% viability following hypotonic challenge.

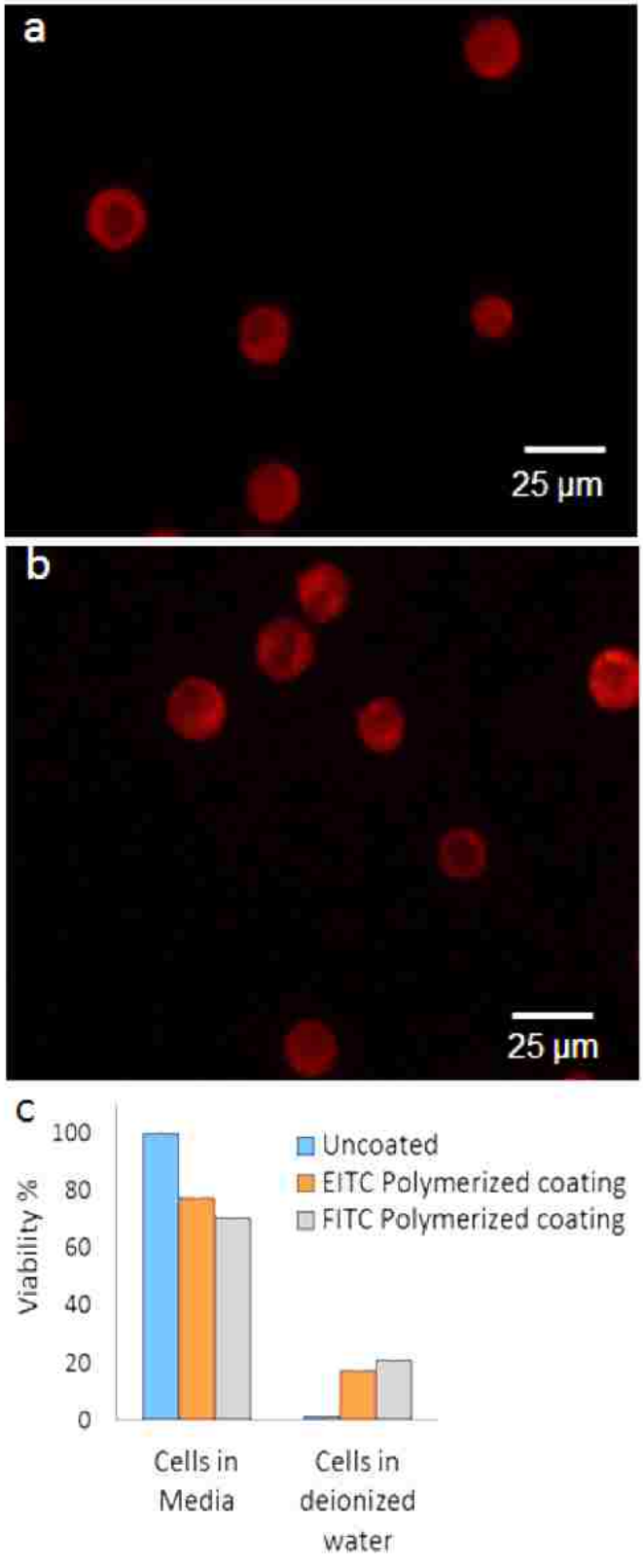
a
25 µm
b
25 µm
c
Viability %
100
80
60
40
20
0
Uncoated
EITC Polymerized coating
FITC Polymerized coating
Cells in Media
Cells in deionized water

Figure 5.7: Polymerization of A549 cells using an eosin or fluorescein photoinitiator targeted to EGFR and PEGDA3500 as a monomer. (a) Fluoroscence image of A549 cells coated with red fluorescent hydrogel using an eosin photoinitiator. (b) Fluoroscence image of A549 cells coated with red fluorescent hydrogel using a fluorescein photoinitiator. (c) Viability of A549 cells determined using MTT assay at various stages of polymerization (n=3).

These findings indicate film generation with a commercially obtained FITC bioconjugate is similar to that of the SA-EITC that is extensively used. Cell viability data and micro array studies agree with the performance of FITC compared to EITC. Our results support the use of FITC initiated systems for cellular encapsulation in isolation [21, 33], immunoprotection [33, 134-136] applications as well as sensitive polymerization-based amplification [44].

5.4 Conclusion

In this study we directly compared the initiating ability of SA-EITC and SA-FITC on micro array formats under cytocompatible conditions. We sought to determine the feasibility of commercially available FITC conjugates for live cell encapsulation as a standardized alternative to custom SA-EITC conjugates. Although spectral calculations indicate that FITC absorbs 48% less light than that of EITC for the 530 nm LED used here, film generation on micro array systems were comparable. FITC systems were able to generate films of ~100 nm in the constrained cell friendly environments and ~350 nm is unconstrained conditions. Live cell studies indicated very similar viabilities of polymer coated cells as well as hypotonically challenged cells with either system. These results

support the use of commercially available FITC-conjugates for single cell encapsulation, thus further standardizing the encapsulation process.

CHAPTER 6. SCALING PROCESS TO THERAPEUTIC SCALE FOR ACCURATE CTC DETECTION AND ISOLATION

6.1 Introduction

Cancer is a leading cause of death in the United States and worldwide. With an estimated over 1.7 million new cases in 2017, and a lifetime probability of diagnosis of 40.8% and 37.5% for men and women respectively, cancer research is among the most intensely studied diseases [137]. Tools for early diagnosis, prognosis, and effective treatments in this drastically heterogenous disease are rigorously studied [67, 69, 70, 138]. A subset of cancers and by far the most lethal, are the metastatic diseases. Metastasis occurs when cells from the primary tumor make their way into the blood stream, travel to a distant site and exit circulation where they colonize and begin the formation of a secondary tumor [24, 26, 67, 71]. Metastatic cancers are responsible for >90% of all cancer related deaths [26, 67]. Multiple mechanisms are thought to be responsible for the presence of circulating tumor cells (CTCs) including leaky vasculature, and a phenotypic change from more adhesive cell type to much more invasive and mobile cells called the epithelial to mesenchymal transition (EMT) [88, 139]. EMT is thought to be a reversible process where cells lose epithelial nature to enter circulation, but then regain lost characteristics during colonization at a distant site [139]. Tumor cells in circulation were first observed over 150 years ago [68], and have been widely studied ever since [24, 26, 67, 71]. Recently, the concentration of CTCs in peripheral blood has been shown to provide important prognostic information in some cancers [29-31, 140]. Not only does accurate detection of these cells serve as a prognostic indicator, but these cells present the possibility of an early diagnostic tool in the form of a ‘fluid biopsy’. These CTCs are believed to appear in blood as many as 17 years before a primary tumor becomes large enough to detect with typical scans [71].

Early diagnosis of cancers, especially the lethal metastatic variety, would allow patients to undergo treatment years before the current timeline which would greatly increase survival rates [69, 70]. This diagnostic tool also has the advantage of being minimally invasive as opposed to invasive and often painful solid tumor biopsies. Accurate detection and enumeration of CTCs is plagued by the extreme rarity at which they occur (~1 CTC per million nucleated blood cells), and the vast heterogeneity in characteristic marker expression between cancers [24], as well as a result of EMT [26]. The rarity at which CTCs are observed in blood indicate the need for a robust detection method that can process large cell numbers while maintaining high sensitivity.

The two most common types of viable cell isolation techniques are magnetic activated cell sorting (MACS) and Fluorescent activated cell sorting (FACS). These two methods both use antibodies that target antigen expression characteristic of the target cell population to distinguish them from the rest of a heterogenous sample. MACS uses antibody functionalized magnetic microbeads to label target cells rendering them susceptible to magnetic fields. Cell are then passed through a column that is placed within a strong magnetic field. Magnetically functionalized cells are retained at the wall of the column while all other cells pass through, followed by removal of the magnetic field and collection of target cells. FACS surface functionalizes specific cells with fluorochromes. Flow cytometry is then used to physically separate target cells from the rest of the population. Using microfluidics to funnel cells into single file, cells are fluorescently analyzed one-by-one. The sample stream is aerosolized into microdroplets containing individual cells. Each droplet is electrically charged based on the cell's fluorescent characteristics before passing through an electric field where droplets are deflected to

separate containers based on charge. While MACS maintains the advantage of high sorting speeds (up to 10^{11} cells in ~30 min) [75], the isolation purity is far less than desired, and is dependent on initial target cell population [78, 79]. FACS is able to achieve very high purities but is greatly limited by the processing time in large cell numbers due to analysis of each individual cell.

Currently, the only FDA approved CTC enumeration method for clinical utility is the CellSearch system [29-31, 140]. CellSearch uses MACS as a pre-enrichment step followed by cell fixation, permeation and intracellular staining for characteristic epithelial markers. Stained cells are then analyzed by a Celltracks Analyzer II where positive cells are determined visually by the user. While magnetic enrichment decreases the overall cell count to be analyzed microfluidically, processing time may still be a challenge when scaling batch sizes. The major limitation of the CellSearch system is the lack of viable isolated cells. Fixation and intracellular staining may provide prognostic information, but at the cost of translation of the technology. Fixation limits the applications of the CellSearch system to enumeration only, and provides no possibility of functional cell analysis or use of isolated cells.

Our lab has developed an isolation strategy that possesses the processing power of MACS and the isolation purity of FACS using relatively inexpensive materials. Antigen specific lysis (ASL) uses antibody recognition similar to that of MACS and FACS to very specifically distinguish target cells within multiple populations. Target cells are surface functionalized with a visible light photoinitiator, where upon radiation in the presence of monomer will initiate localized polymerization individually encapsulating target cells in a protective hydrogel. The entire population is then subject to harsh conditions, such as ionic

surfactants, in which all antigen negative cells are lysed while polymer coated cells are protected leaving a nearly 100% pure population. A major proposed advantage to this technology is the ability to scale batch size by one to two orders of magnitude with little to no increase in processing time. Scaling systems that require flow cytometric analyses are also accompanied by a directly proportional increase in processing time. A fluid biopsy for screening is likely on the order of 10-100 mL of peripheral blood. In an adult, this would contain 10^8-10^9 peripheral blood mononuclear cells (PBMCs). For FACS to accurately process this number of cells would be on the order of 10-20 hours for one sample. ASL has the potential to accomplish the same FACS purity in as little as 1 h per sample. Another major advantage of ASL is the result of viable cells upon isolation, which allows enumeration of CTCs like CellSearch while further adding the aspect of functional CTC analysis upon isolation. The clinical utility of a fluid biopsy for early cancer detection, prognostic information, and functional analysis of these highly sought-after cells is invaluable.

Here, we systematically study all parameters associated with the ASL processing for rare cell isolation for scaling to a clinically relevant batch size for potential fluid biopsy. Optics, chamber materials, chamber geometry, cell densities, fluid volumes, and more are studied to determine what factors are key to successful rare cell isolation.

6.2 Materials and Methods

6.2.1 Micro array printing

Micro arrays were fabricated as described in Chapter 3.5, as well as additional slides with minor changes in printed concentration of bBSA solutions. All spots were printed

with the same concentration of bBSA to ensure identical biotin surface densities for accurate analysis of other parameters. All array spots were printed with a bBSA concentration of 160 μg/mL in PBSA for a total protein concentration of 1000 μg/mL.

6.2.2 Radiation intensity with increase monomer volume

Whatman incubation chambers were firmLy held against a standard microscope slide using binder clips. Clips were positioned such that slides were able to lay flat upon the radiometer detector without any obstruction of optics. Complete PEGDA 700 monomer formulation was added to the slide first at 150 μL followed by 100 μL additions. Radiation intensity was recorded along with the total monomer volume after each addition. All monomer formulations for intensity measurements and polymerization experiments on micro arrays used PEGDA 700 as described in Chapter 3.6.

6.2.3 Maximum Target Cell Density

Maximum target cell density was assessed by varying number of total cells processed with volume processed. Physical parameters such as fluid depth and radiation incident angle were controlled by changing only chamber surface area to vary volume. Three glass bottom dishes (Cellvis) of varying diameters (10, 14, 20 mm) with constant well depth were used. All glass bottom dish diameters were well within the diameter of the radiation beam. Polymerization using PEGDA 700 on cell surfaces was performed as described in Chapter 3.9.

6.3 Results and Discussion

Here, we sought to quantitatively assess the parameters associated with localized polymerization on both controlled micro array formats as well on living cells. Initiation of polymerization through visible light radiation is highly dependent on observed radiation intensity by the photoinitiators. This has been shown in multiple studies including the previous chapter and is observed in Figure 5.6. When scaling the process, volume of monomer solution used, and perhaps more importantly, depth of a monomer within the cell solution chamber can have a large effect on the radiation which cells further from the solution surface see. The monomer solution is relatively clear and colorless and therefore absorption of visible light is minimal, but slight turbidity and light scattering play a role. Using a radiometer, we monitored the effect of fluid depth on radiation intensity observed. Figure 6.1 shows the normalized radiation intensity with different monomer volumes within the polymerization well.

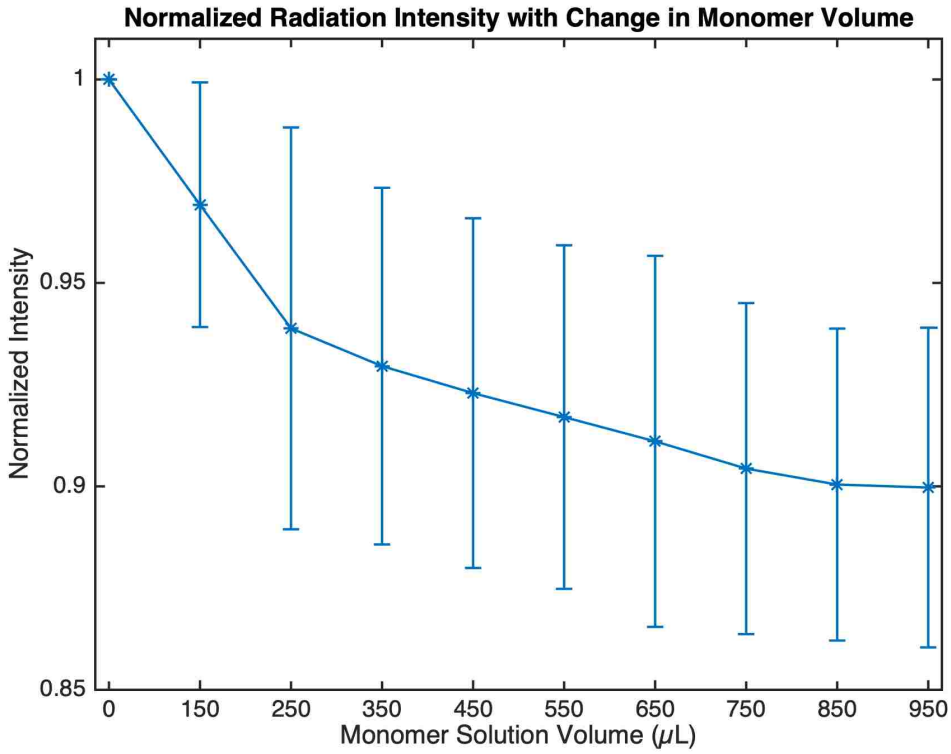

Figure 6.1: Normalized observed radiation intensity for increasing volume of monomer solution. Values are normalized to observed radiation through a standard microscope slide in the absence of monomer solution.

All values were normalized to the radiation observed in the presence of the glass slide and absence of monomer solution. As expected, radiation observed by the detector after passing through the solution slightly decreases in intensity. One interesting observation is the radiation intensity appears to level off as monomer addition is continued. This may be explained partially by the irregular geometry of the chamber wall as fluid depth increases, as well as meniscus effects with chamber wall. With these variables, 100 µL additions may not directly translate to an increase in fluid depth associated with a perfectly square or circular wall geometry. Therefore, additional experimentation is warranted using a more controlled geometry. In light of these findings, we proceeded to determine the effect of the

fluid depth on film generation using micro array slides. Figure 6.2 reports thickness of generated film as determine by profilometry for multiple monomer volumes in the same size well.

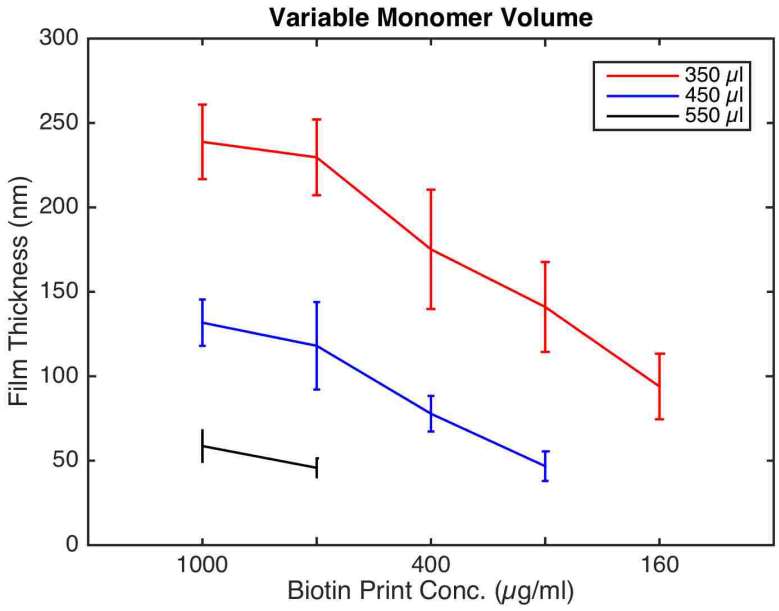

Figure 6.2: Thickness of generated polymer film determined by contact profilometry for multiple monomer volumes within the same chip well.

From Figure 6.2 it is evident that the volume of solution plays a significant role in the ability to generate polymer. However, the drastic decrease in film generation correlated to the difference in observed radiation intensity suggests that there are more factors effecting the system than fluid depth alone. Figure 6.1 shows less than a 2% difference in observed radiation intensity from 350 µL to 550 µL of monomer solution, as Figure 6.2 shows an ~4-fold decrease in film generation from 350 µL to 550 µL. Another major factor in radical polymerization that would depend on solution volume is the presence of oxygen in solution. Oxygen is known to quench active radical species hindering free radical polymerization. For this reason, all polymerizations are carried out under an inert nitrogen

atmosphere. As described in Chapter 3.9, the system is purged for 5 mins before and for the duration of irradiation. Purging the system with nitrogen facilitates diffusion of oxygen out of solution for less radical quenching. Increasing solution volume affects the rate at which oxygen leaves the system. As concentration is the driving force behind mass transport, increased fluid depth correlates to increased time before a change in oxygen concentration is observed at points furthest from the solution/nitrogen interface. Additional experimentation was done using nitrogen bubbled solutions. Identical processing to that of data collected for Figure 6.2 was done, with the additional step of gently bubbling nitrogen through the solution. Although this step introduces additional variables such as evaporation of solvent which may result in slight changes in component concentration, it greatly increases the rate at which oxygen is removed from solution. Figure 6.3 shows the thickness of generated film for the experiment including nitrogen bubbling.

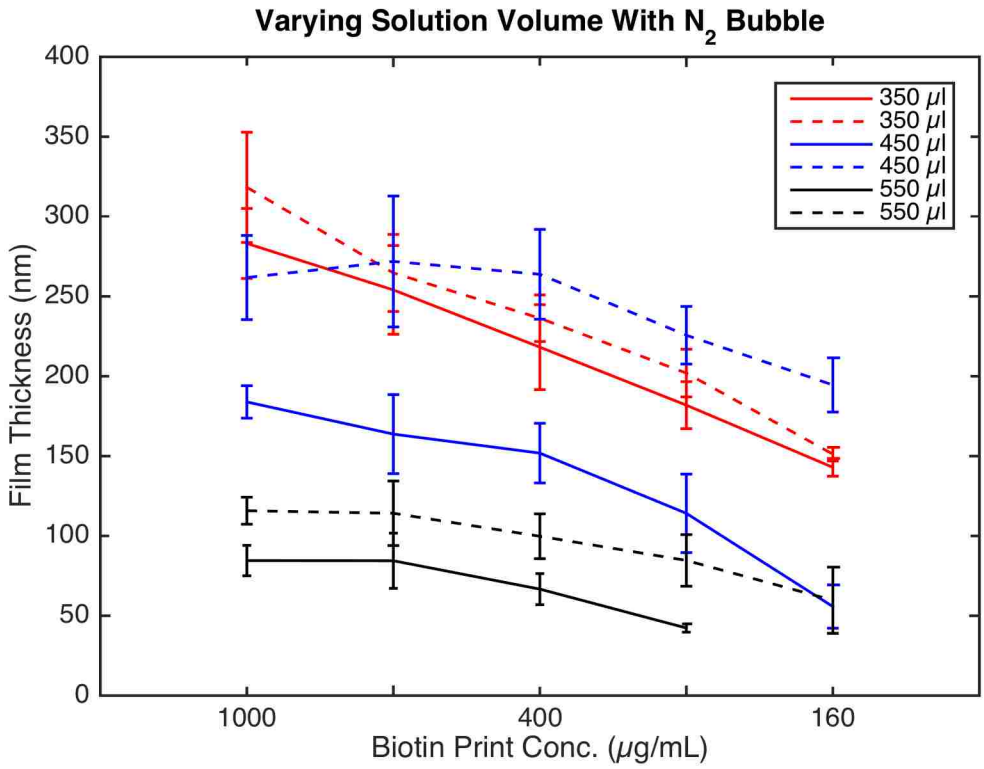

Figure 6.3: Thickness of generated polymer film determined by contact profilometry for multiple monomer volumes within the same chip well after nitrogen bubbling of the monomer solution. Dashed lines indicate nitrogen bubbled monomer studies, while solid lines indicate studies without bubbling nitrogen through the monomer before use.

While there still appears to be a trend in monomer solution depth and with thickness of generated film, the distinction is less evident. These data support the hypothesis that oxygen diffusion plays a role in film generation through the increase thickness for all monomer volumes studied and the increased sensitivity in film generation of 450 µL and 550 µL volumes on the lower biotin printed spots. Additional experimentation of these conditions may be required to allow statistical analysis for this parameter.

Next, we looked to determine the film generation dependence on the variation in light intensity within the radiated area as well as meniscus effects at the edges of the solution chamber. Although the collimated light source is theoretically consistent in radiation intensity in the beams cross sectional area, slight variations are inherent within the LED system. Additionally, the angle of incidence between light and the solution will affect the amount of light transmitted across the change in medium. With the micro array centered within the chip clip well, the solution fluid is relatively flat and therefore the angle of incident light essentially 0˚, which facilitates a maximum transmittance. In the meniscus region however, this angle will be significantly greater. In cellular studies, as opposed to micro array polymerization, target cells occupy the solution well and not just the center. Figure 6.4 demonstrates how each of these parameters effect film generation.

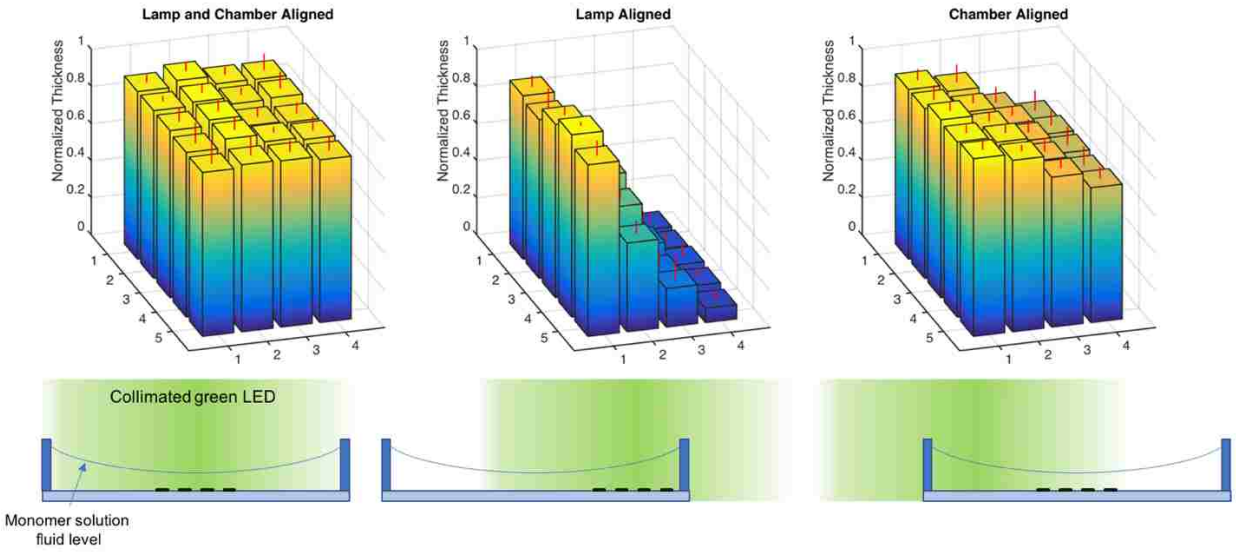

Figure 6.4: Normalized film thickness generated on micro arrays under varying conditions. Left: Array centered within the chip well and centered within radiation area. Middle: Array positioned at the edge of the chip well where the meniscus is most prominent while centered under radiation area. Right: Array centered within chip well while positioned at the edge of radiation area where variation in light intensity is most prominent. Top: Normalized film generation (x and y axes represent printed micro array position analyzed. Conditions varied in the x direction). Bottom: Schematic of polymerization set up (View of the x-z plane).

It is evident from Figure 6.4 that the meniscus plays a crucial role in film generation on micro array polymerization. Light variation across the collimated source is also a minor factor as is evident from the slight decrease in film generation in spots as they approach the edge of the beam. It is worth noting that while there is not quantitative data for the combined effect of lamp variation and the meniscus it is highly likely that the two

parameters would compound to show an even greater deficit in film thickness. Again, this becomes a more significant issue in cellular polymerizations as a large number of cells occupy this area.

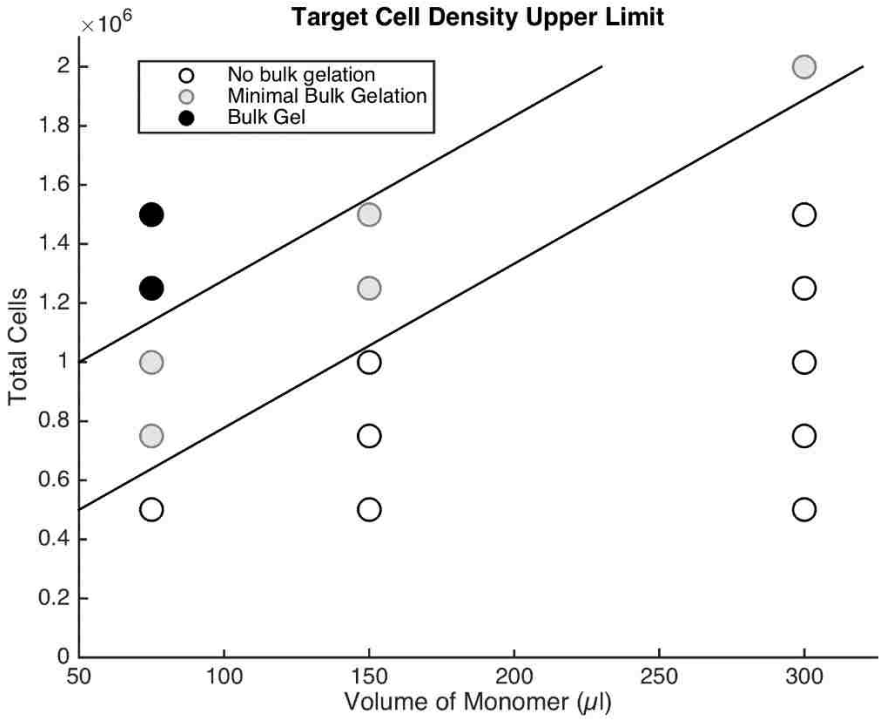

Figure 6.5: Analysis of total cells processed with total volume processed. Lines draw estimated distinction between observed bulk gelation and individual cell encapsulation.

In conjunction with acellular studies, cellular experiments were also conducted. As maximum target cell density is not likely an issue regarding rare cell isolation, we still explore this parameter for rigor as exceeding this maximum results in bulk gelation of the sample in a covalently crosslinked system. As shown in Figure 6.5, we have observed an upper limit of target cell density to be ~6-8 million cells/mL. At this point small bits of bulk polymer will form in solution. Exceeding these cell densities resulted in nearly a one

continuous crosslinked network of cell laden hydrogel. Minimum target cell density is among the most important of the parameters as CTCs are on the order of 1 per million PBMCs. Achieving this level of sensitivity is crucial to providing diagnostic and prognostic information in a clinical setting.

6.4 Conclusion

Here we systematically study the processing parameters of ASL for scaling to clinically relevant batch sizes. This system has the potential to provide highly sensitive, viable cell isolation for the application of CTC detection in a fluid biopsy. As the only FDA approved method for CTC enumeration does not produce viable cells for functional analysis, we propose a novel and scalable alternative to viable cell isolation in ASL. Through the information gained in this study, we can improve the efficacy of the current batch sizes as well as determine what parameters are of great importance in clinically relevant batches. Although experimentation is ongoing, we have learned a great deal in acellular studies. Angle of incident light, and monomer solution depth (with roles of oxygen diffusion) appear to have great effects on the ability to generate film on micro array slides. These data suggest that increasing processed volumes by increased solution chamber surface area as opposed to depth would be beneficial. This would minimize attenuation of light by scattering within the monomer solution as well as allow for rapid diffusion of oxygen away from the system. A potential problem is that increased surface area also increases evaporation rate of monomer solution in volume per time. Additionally, solution chambers that have a minimized meniscus, maximizing light at a normal incidence would also maximize the efficiency of the irradiated area.

CHAPTER 7. MECHANICAL PROTECTION FOR HIGH RESOLUTION, HIGH THROUGHPUT 3D CELL PRINTING

7.1 Introduction

The shortage of donor organs continues to be critical problem [141]. Efforts have been made through education programs and expanded donor criteria to increase the number of donors [142], but the demand continues to rise faster than supply. Every day 20 patients die waiting on a donor organ (based on OPTN data for 2017). There are currently over 4,000 patients on the waiting list of a heart while less than 3,300 heart transplants were conducted in the entire year of 2017 (based on OPTN data for 2017). The drastic deficit of cadaverous and live organ donors to the demand clearly highlights the need for a new source of viable organs. 3D bioprinting shows great promise in bridging this gap between supply and demand. 3D bioprinting is the precise deposition of biological or biocompatible components into constructs to imitate or replicate natural functions. Non-biological 3D printing has gained great momentum in the past two to three decades. It has been used to print a range of structures from toys and trinkets, to objects for educational purposes, to functional prosthetics [57, 58]. 3D printing has proved to be very useful for education in the medical field [143]. Printed anatomical structures help to visualize the complex morphologies in ways that 2D representations fail. This can be especially important in surgical planning where imaging and printing surgical sites of interest or anomalies can greatly prepare surgeons for medical procedure [46, 47]. In recent years, this technology has been translated to use with biocompatible materials in printing numerous cellular and acellular structures for tissue engineering in regenerative medicine [48-54], and 3D organ-on-a-chip for in vitro drug screening [55, 56]. The world of 3D bioprinting holds an

exciting future in a range of biological applications including the printing of whole organs for transplant.

The keys to successful tissue/organ printing are precise, high throughput deposition of viable cells. Incorporation of vasculature within large tissue is critical for transport of nutrients to sustain viability, but requires extremely high-resolution printing. With the harvesting, propagation, and differentiation of a patient's own stem cells, tissues can be printed with the necessary numbers and phenotypes while ensuring that the possibility of graft vs. host rejection is nearly eliminated [48, 53, 144]. This type of transplant is essentially an autograft. 3D bioprinting has made great strides in the past 5-10 years, but there are still many challenges that must be overcome before viable organ printing is achieved.

Extrusion based bioprinters are a common type of printer that are commercially available. These printers use pressure or mechanically driven flow to extrude material through a small nozzle for direct write printing [59]. These types of printers are common due to their simple design, moderate affordability, and compatibility with a large range of viscosity bioinks and cell densities [48, 59, 145]. Some of these printers even have the capability of printing multiple cell types through a multi-head printer design [53, 146, 147]. When printing cellularized scaffolds, these printers commonly use a suspension of cells in a cytocompatible material, or 'bioink' for deposition onto a substrate. Common bioinks consist of poly-(ethylene glycol) (PEG) acrylates, gelatin, collagen, and alginate [48, 49, 51, 53, 54, 62, 64, 65]. As advances in tissue engineering continue to be made, the choices of biocompatible materials for potential bioink is increasing.

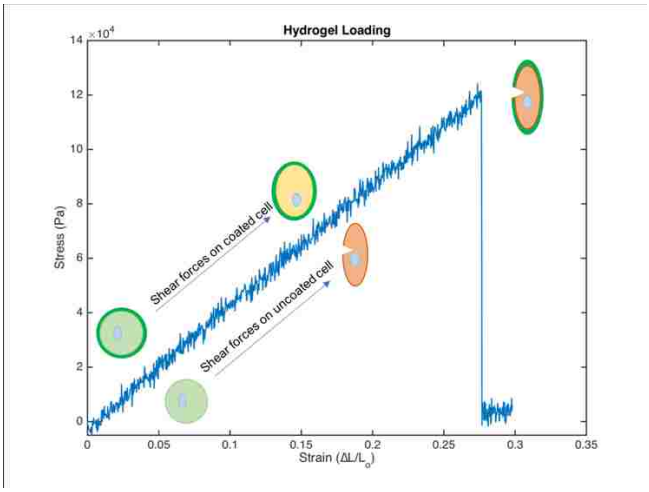

Figure 7.1: (Top) Schematic representation of cell deformation due to mechanical forces during extrusion printing. As printing resolution increases from left to right with constant flow rates, fluid velocity increases along with shear stress, τ, and pressure drop, ΔP. (Bottom) Stress/strain relationship for PEGDA 2000 subjected to uniaxial tension with representation of coated and uncoated cell response to increasing fluidic shear.

Extrusion based printers carry with them the inherent challenge of shear mediated cell damage. While tensile, compressional, and shear forces are all mechanical stimuli a cell can experience during the printing process [64, 148, 149], shear forces have been the

main concern in maintaining cell viability and membrane integrity [65, 150, 151]. In fluid flow through a small pipe, shear forces are created by the radial velocity gradient associated with laminar flow [152]. These forces are highly dependent on pipe or capillary diameter as well as flow rate. Figure 7.1 shows a schematic for the effect of shear forces on living cells. For large tissue/organ printing, the combination of high throughput (high flow rate) with high resolution (small capillary diameter) presents a critical issue for reduced cell viability from shear-mediated death. 3D cell printing is commonly performed at resolutions much greater than that of a single cell (150-300 μm nozzle diameter) and at flow rates that are typically on the order of 1-10 μL/min. [60-63] With these current printing conditions it would take on the order of 100 days to print one organ without achieving the necessary resolution required for small vasculature. In efforts to minimize shear forces experienced by cells, studies have been done in areas such as altering print heads [64], using low viscosity bioinks [65] or using shear thinning fluids [63]. These printing techniques have been able to print with high cell viability, but still with moderate resolution and relatively low throughput. Advances must continue to be made in order for whole organ printing to be done on a time scale plausible for transplantation.

In this study, we analyze the protective potential of hydrogel encapsulation against the mechanical forces of high throughput, high resolution cell printing. Through a novel encapsulation method developed in our lab, we examine polymers possessing a range of mechanical properties on their ability to reinforce the cell membrane during extrusion. Rat cardiac myoblasts (H9C2 cell line) were used as a model for cardiac tissue printing. These cells were individually encapsulated by surface mediated photo-initiated radical polymerization [33]. Both uncoated and surface functionalized cells were extruded through

50 μm diameter capillary at 4.8 μL/s. Cells were then analyzed for intactness using scattering parameters in flow cytometry upon extrusion, as well as using two viability assays. We then sought to decouple the cellular damage caused by rapid pressure changes and shear associated with high throughput extrusion printing. Each parameter was tested separately outside the system of extrusion for individual analysis. Mechanical properties of each polymer were recorded for correlation to protection potential. This work aims toward providing membrane reinforcement for simultaneous high resolution and high throughput bioprinting for goals in whole organ printing.

7.2 Materials and Methods

7.2.1 Cell Encapsulation

Five different monomer formulations were evaluated for their protective potential in a high shear, extrusion environment. All formulations contained equal amounts of the co-initiator triethanolamine (TEA, Sigma >99%) and co-monomer vinyl pyrrolidinone (VP, Sigma >99%) at 35 mM each. PEGDAs 700 (Sigma), 1000, 2000, and 3400 were all used at 25% w/v, and the fifth formulation was 1% w/v of PEGDA 3400 with 3% w/v gelatin methacryloyl (gelMA; BioBots). The formulation containing gelMA and PEGDA 3400 is denoted as gelMA/3400. PEGDA 1000, 2000 and 3400 were all synthesized in house as described in Chapter 3.1. All other procedures including cell culture, viability assays, extrusion, and analysis are described in Chapter 3.

7.3 Results and Discussion

7.3.1 Mechanical Properties

Here, we present an extended application to a novel method of individual cell encapsulation using surface mediated radical polymerization developed in our lab. Encapsulation in a protective hydrogel provides mechanical protection of rat cardiac myoblasts for simultaneous high resolution and high throughput bioprinting. We have shown that encapsulation in thin hydrogel polymers possessing the right mechanical properties yield significantly more intact cells over uncoated cells upon exposure to high shear forces experienced traveling at high speeds through a narrow capillary.

Young's modulus is a measure of hydrogel stiffness. The Young's modulus, which is commonly referred to as the modulus, of the gel is a measure of the deformation (strain) of the gel required to develop a given stress. Stiffer materials have a higher modulus and therefore generate a larger stress from the same deformation as softer materials. The modulus of each gel was calculated by equation (1) below,

$$E \equiv \frac{\sigma}{\epsilon} = \frac{F/A}{\Delta L/L_o}. \quad (1)$$

Where σ is the stress, or generated force, F, per cross sectional area, A, and ϵ is the strain, or change in sample length, ΔL, relative to initial length, L_o. Moduli ranged from 9.2 +/- 0.8 kPa for gelMA/3400 to 1269 +/- 103 kPa for PEGDA 1000. Although PEGDA 700 did not have the highest average modulus (Table 7.1), the means between PEGDA 1000 and PEGDA 700 were not statistically different, suggesting that the small difference in molecular weight did not greatly affect the mechanical properties and therefore still preserving the expected trend between modulus and monomer molecular weight.

Table 7.1: All mechanical properties recorded for each polymer assessed. Data reported as mean ± standard deviation.

Monomer	Swelling Ratio	Modulus	Ultimate Tensile Strength (kPa)	Max Strain (%)
700	3.02 ± 0.03	$1.21 \times 10^3 \pm 127$	138 ± 36	11 ± 2.7
1000	3.77 ± 0.12	$1.26 \times 10^3 \pm 103$	128 ± 26	9 ± 1.4
2000	5.41 ± 0.12	502 ± 61	134 ± 23	9 ± 3.6
3400	7.21 ± 0.01	204 ± 20	55.0 ± 7.1	25 ± 0.94
GelMA/3400	15.4 ± 0.89	9.2 ± 0.79	$6 \times 10^{-4} \pm 3 \times 10^{-4}$	44 ± 13

The expected trend of increasing modulus with decreasing molecular weight is due to the formation of a more tightly crosslinked network. As molecular weight decreases, molecular weight between crosslinks also decreases limiting the mobility of polymer chains within the gel and therefore increasing the observed stiffness.

Ultimate tensile strength (UTS) and percent elongation at failure (%EL) were calculated by equations (2) and (3) respectively.

$$UTS = \frac{F_f}{A}. \tag{2}$$

$$\%EL = {}^{\Delta L}/_{L_o} \times 100\%. \tag{3}$$

Where, F_f is the force applied at the point of failure. Swelling ratios were determined as described by equation (4) below,

$$SR = \frac{m_s - m_d}{m_d}. \tag{4}$$

Where m_s is the mass of the swollen gel and m_d is the mass of the dried polymer. The calculated swelling ratios of the five formulations ranged from 3.02 +/- 0.03 for PEGDA 700, to 15.41 +/- 0.89 for gelMA/3400. As expected, the swelling ratio decreases as the molecular weight of the monomer decreases similarly to that of the modulus. This is due to a decrease in molecular weight between covalent crosslinks within the hydrogel network limiting the ability of the gel to take on water and swell.

7.3.2 Protective Potential

Cell samples were analyzed by flow cytometry both before and after extrusion process. Events were gated for intact cells in samples before being extruded through the capillary. These same gates were used to determine the fraction of cells that remained intact after the harsh forces of high flow rate extrusion through the capillary. Figure 7.2 is a representation of how each sample was gated and analyzed.

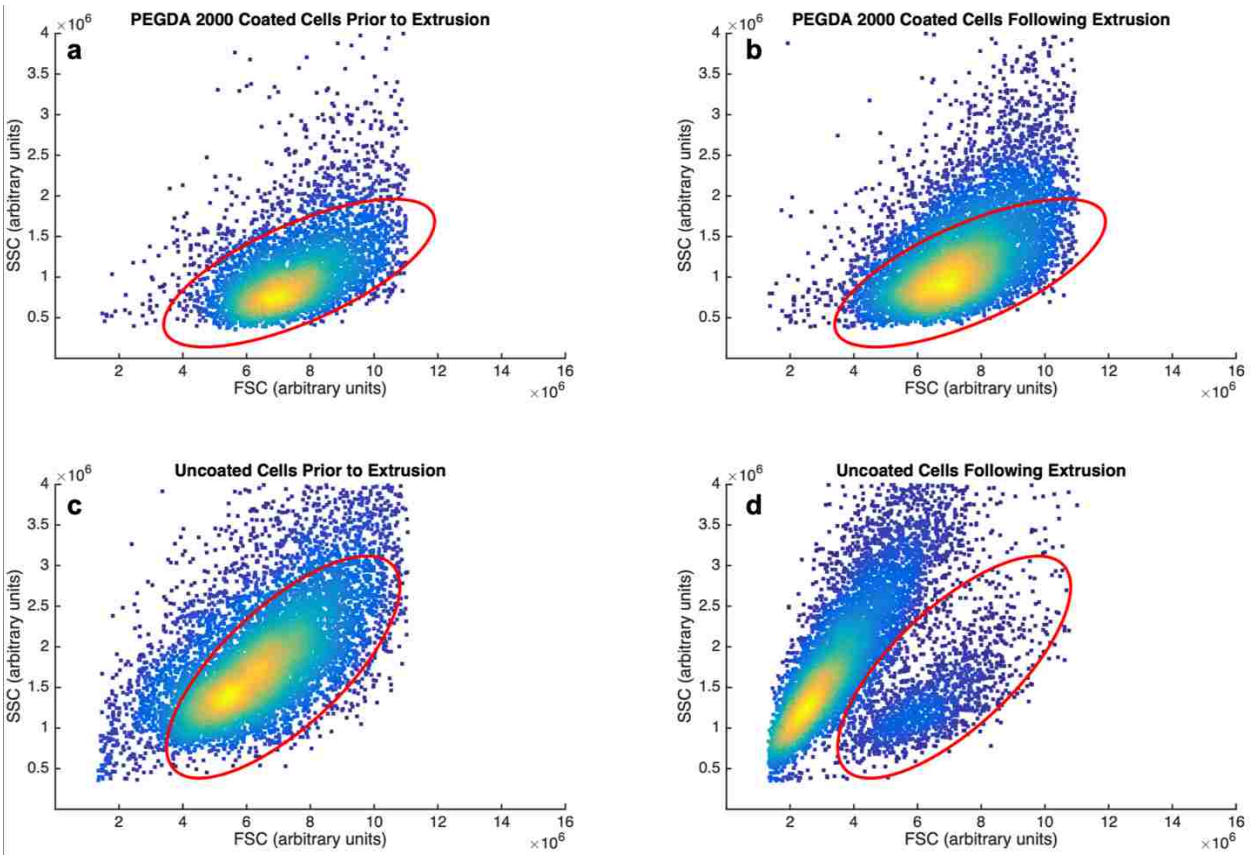

Figure 7.2: Sample gating of flow cytometry scatter plots for PEGDA 2000 coated cells before (a) and after (b) extrusion, and uncoated cells before (c) and after (d) extrusion. The red circle indicates the gated region consistent with intact cells.

Upon extrusion through the capillary tube, percentage of intact cells were recorded and normalized to the percentage of cells that fell within the gate prior to extrusion. Cells were then analyzed by two different viability assays: MTT proliferation assay, and ethidium homodimer permeation assay. Figure 7.3 shows all of the scattering and viability data compiled for each polymer used. Asterisks indicate means that are statistically different from the uncoated cell populations as determined by Student's t-test in Matlab. P-values for Figure 7.3 are given in Table 7.2.

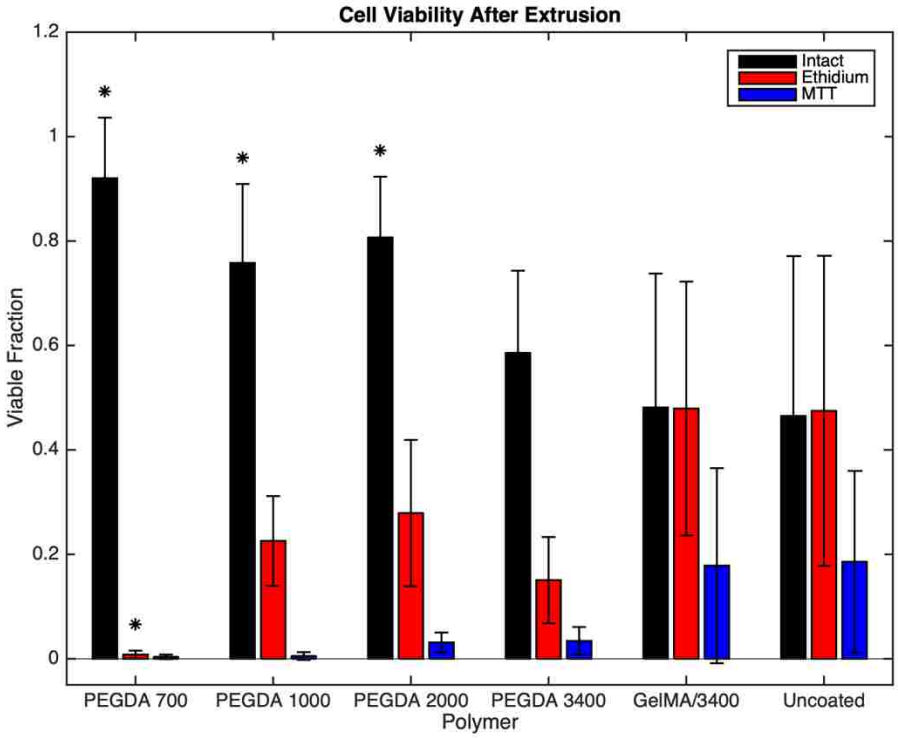

Figure 7.3: Cell viability for each assay type following extrusion for each polymer coating. (* indicates statistically different mean than the corresponding uncoated group.)

Table 7.2: P-values generated using Student's t-test for samples following extrusion when compared uncoated cells (Figure 7.3).

	P-Values		
Polymer Type	Scattering Analysis	EthD-1	MTT
PEGDA 700	0.005	0.003	0.107
PEGDA 1000	0.039	0.062	0.110
PEGDA 2000	0.027	0.179	0.165
PEGDA 3400	0.462	0.050	0.173
GelMA/3400	0.924	0.980	0.945

These viability data were then plotted against the measured mechanical properties of each polymer to observe trends in protection potential. Figure 7.4 shows each polymer property plotted against ethidium permeability assay as well as fraction intact as determined by scattering properties in flow cytometry. MTT assay viability was left out of these figures for clarity.

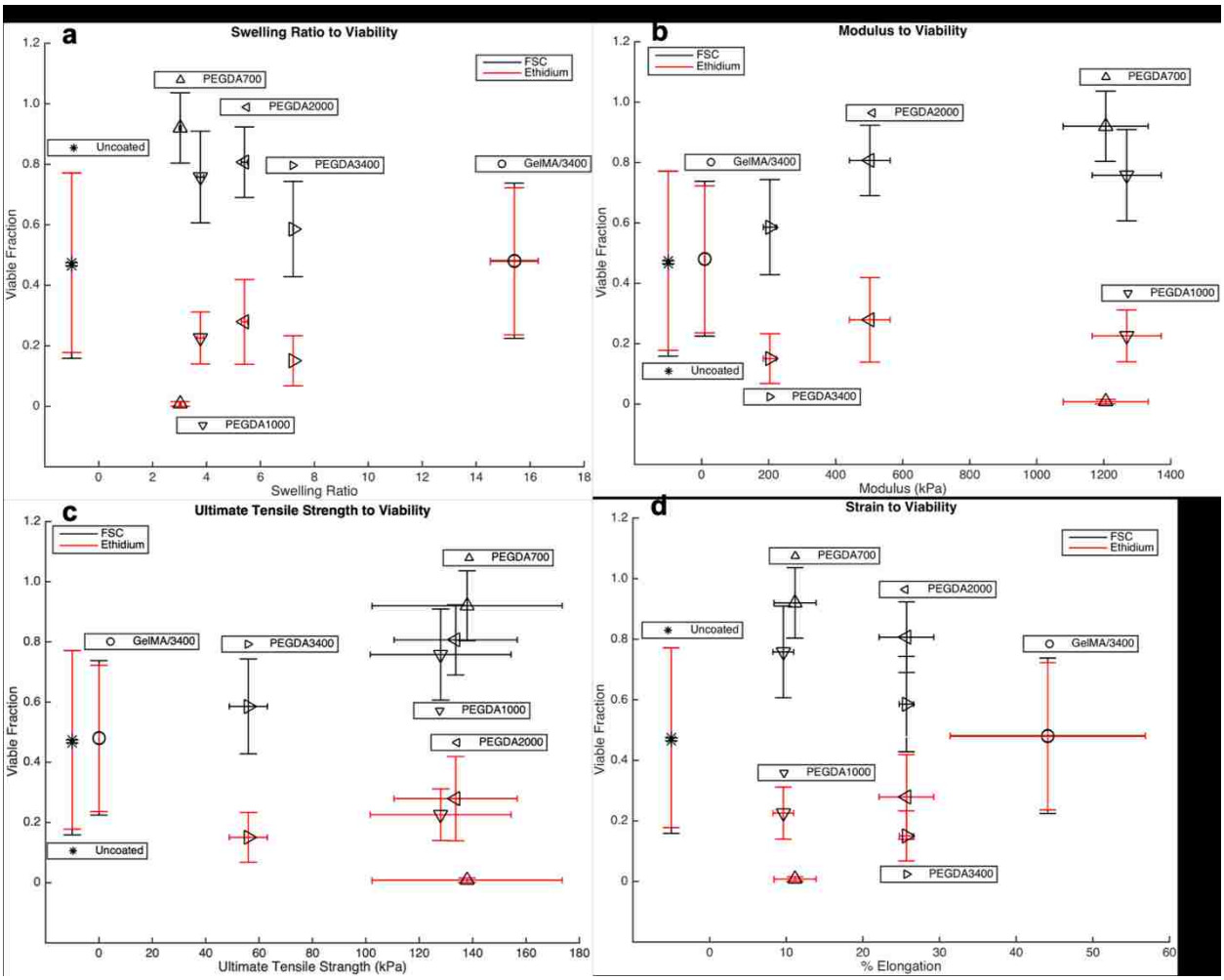

Figure 7.4: Mechanical properties of each gel plotted against ethidium permeability assay and scattering properties. (a) swelling ratios, (b) modulus, (c) ultimate tinsel strength, (d) percent elongation at failure. Polymer legend, scattering data, and ethidium assay data are vertically in line with one another for a specific polymer.

From this figure it can be observed that there is a clear trend between percentage of intact cells by scattering to swelling ratio and modulus. Coatings formed using the higher modulus gels, PEGDA's 700, 1000, and 2000, showed a significantly higher protection potential from lysis due to shear forces than the softer gels of PEGDA 3400 and

gelMA/3400 which did not significantly protect cells from lysis. This suggests that cells coated in the higher modulus gels (>500 kPa) experience less deformation under the same fluid forces and therefore reduce the number of cells lysed in the process. This same trend was also observed for the swelling ratio. Polymers with a swelling ratio of <5.5 showed significant protection when compared to uncoated cells. This data once again reinforces the hypothesis that the tighter crosslinked gels limit deformation reducing the number of cells lysed. Although the high variance in the data does not support a definitive conclusion, this trend may extend to ultimate tensile strength (UTS) as well. The observed UTS's for the three polymers that showed significant protection ($p < 0.05$) are not distinguishable between one another, but all three are significantly higher than PEGDA 3400 and gelMA/3400, which do not significantly protect from lysis. This again supports that the mechanical properties of the gel greatly influence the protective potential.

During the simulated printing process cells experience rapid and high changes in pressure (~16 bar in < 0.1 s). Drastic fluctuations in pressure could potentially change the solubility limits of gases dissolved within the cell solution, as well as exert compressional forces on cells which can affect the folding properties and stability of cellular proteins [153, 154] . Gases coming out of solution causing microbubbles have the ability to disrupt the cell membrane or organelles within the cell hindering or eliminating cellular function [155]. Changes in specific protein properties or the unfolding of proteins could reduce the cell's ability maintain normal functionality. In 3D extrusion printing, the pressure change in the nozzle is coupled to the shear stress associated with fluid flow and cannot be independently varied. To de-couple these parameters and look at the effect of pressure drop in the absence of shear stresses, we used a pressure chamber to subject cells to the high

pressures experienced during extrusion without any fluid motion. The pressure chamber was quickly opened using a ball valve for a sudden decrease back to atmospheric pressure. This study revealed that pressure changes alone comparable to what cells experienced during extrusion in our system do not affect cell viability. Figure 7.5 shows cell viability for cells following high pressure conditions compared to untouched control cells.

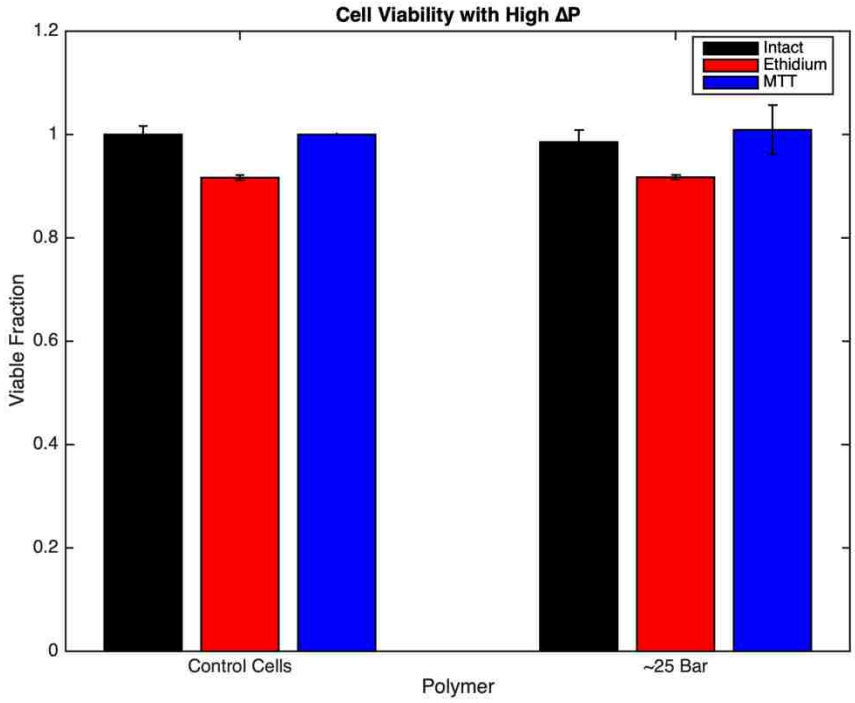

Figure 7.5: Cell viability for each assay type following exposure to high pressures (~25 bar) and rapid decompression (< 0.1s) back to atmospheric conditions.

There were no statistical differences in viability for any of the pressures (8-25 bar) or time lengths (2-10 min) studied. These pressures far exceed those reported in the literature [60, 62]. High viability across all pressures studied supports the hypothesis that cell damage in extrusion printing is highly shear dependent. This study confirms that large pressure drops over very short time scales have no effect on cell viability when at high pressure for ~10

mins. The notion of shear mediated cell damage is supported in literature for printing applications [65, 150, 151], but had not been independently studied. Using A DHR-2 Viscometer (TA Instruments) cells were subject to shear forces associated with fluid motion without pressure driven flow. Cells coated with PEGDA 1000 as well as uncoated cells were exposed shear forces of ~110 Pa for 10 s, then analyzed in flow cytometry for viability and scattering properties. Although 110 Pa is a lower shear stress than what is observed through our extrusion system (~400 Pa), we are still able to induce cell lysis in the control population. Figure 7.6 below shows the viability of cells after exposure to shear forces for uncoated and PEGDA 1000 coated cells, and Table 7.3 gives p-values comparing viability means.

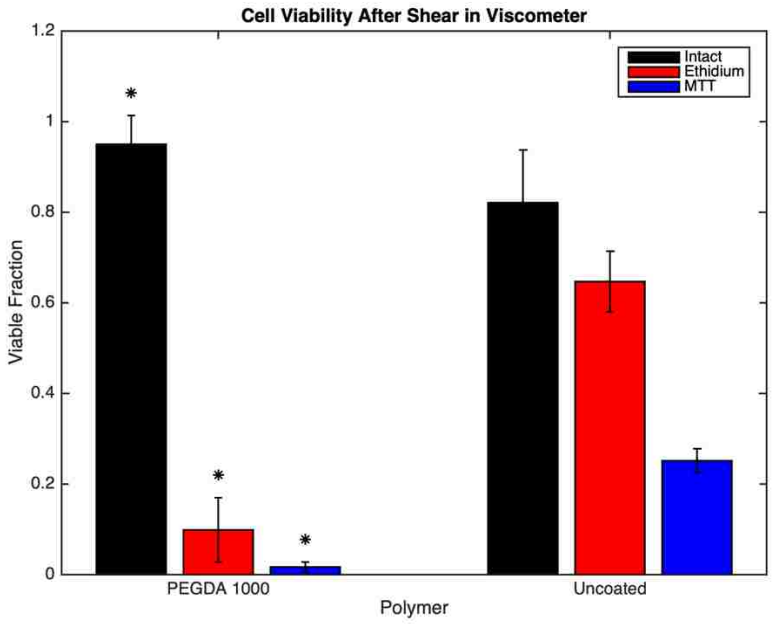

Figure 7.6: Cell viability for each assay type following exposure to shear forces in the absence of pressure changes. (* indicates statistically different means from the corresponding uncoated group.)

Table 7.3: P-values for viability assays of coated cells compared to uncoated cells after being exposed to shear forces only (Figure 7.6).

	P-Values		
Polymer Type	Scattering Analysis	EthD-1	MTT
PEGDA 1000	0.039	1.52×10^{-6}	1.46×10^{-4}

With the shear only system, as with the extrusion system, we see the PEGDA 1000 hydrogel coating provides protection from lysis as analyzed by the scattering properties. The absence of a pressure changes with this system suggest the mechanical properties of the gel reinforce the cell membrane limiting deformation, as suggested with the extrusion system. These data, along with the high cell viability of cells exposed to high pressures further supports the notion of shear forces play the largest role in cell damage upon extrusion.

The viability of all extruded cells is relatively low for what would be desired when bioprinting. With the exception of PEGDA 700 which we know from previous studies is toxic and permeabilizes cells, the viability of coated cells vs. uncoated cells in the extrusion system (Figure 7.3) are not statistically significant (all p-values > 0.1, Table 7.3). Figure 7.7 shows the viability of all cells after hydrogel coating but before extrusion through the capillary.

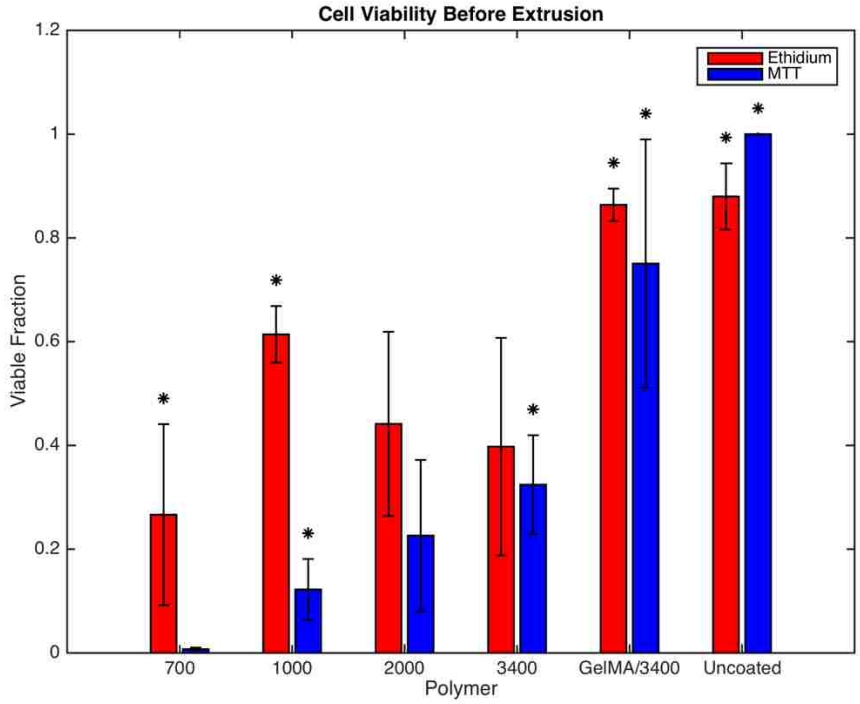

Figure 7.7: Viability assessed by EthD-1 and MTT assay following polymerization prior to extrusion. (* denotes samples that showed a statistically significant drop ($p < 0.05$) in cell viability following extrusion.)

These coatings are preserving the size and shape of the cell as determined by light scattering in flow cytometry, but the cells lack full functionality. This may be partially due to monomer toxicity and may also be partially due to stressing of the cells beyond what is ideal for functionality without complete lysis of the cell membrane. Of all polymers assessed, PEGDA 2000 not only shows significant protection over uncoated cells in scattering analyses, but there is also no significant difference in any of the viability assays between before and after extrusion. P-values for Figure 7.7 are given in Table 7.4. All other conditions show a significant change in viability ($p < 0.05$). PEGDA 2000 preserves the

viability of cells that remain living following polymerization when extruded at high shear stress.

Table 7.4: P-values generated using Student's t-test for viability before capillary extrusion (Figure 7.7) to viability following extrusion of each polymer type and uncoated cells.

	P-Values	
Polymer Type	EthD-1	MTT
PEGDA 700	0.011	0.322
PEGDA 1000	3.0×10^{-6}	0.0297
PEGDA 2000	0.147	0.084
PEGDA 3400	0.071	0.007
GelMA/3400	0.020	0.009
Uncoated	3.4×10^{-5}	1.6×10^{-11}

This suggests that PEGDA 2000 may serve as the best pairing of mechanical properties of polymers studied with minimal cytotoxicity. A contrast to the trend in protection potential of each polymer is the toxicity of the chosen monomer. It is generally understood with PEGDA monomers of smaller molecular weights have a higher cytotoxicity prior to crosslinking and gelation, as observed with PEGDA 700 [131]. Although PEGDA 1000 shows significant protection as with PEGDA 700, the molecular weight is low enough to cause cell damage during polymerization that, when paired with the stress of extrusion, is counter-productive in preserving cellular function. The molecular weights larger than PEGDA 2000 show an increase in viability of cells immediately following polymerization compared to PEGDA 2000 but also show a significant decrease in viability following extrusion when compared to themselves. Therefore, the production potential of the softer gels falls short in comparison to the stiff more crosslinked networks.

7.3.3 Conclusion

In this study we assessed polymers containing a range of different properties on a novel method of mechanical protection. Individually encapsulated cells were subject to high shear forces associated with high throughput, high resolution bioprinting. From these data we show that the mechanical properties of the different polymer films play a significant role in the protection of the coated cell. The extremely soft formulation of gelMA/3400 provided essentially no protection against lysis when compared to uncoated cells. While the higher modulus gels provide significant protection as analyzed by scattering analyses, they do not preserve high cell functionality. Protective cellular coatings of similar mechanical properties to PEGDA 700, 1000 and 2000, with higher cytocompatibility found in gelMA/3400 could provide mechanical protection that also preserves the high cellular functionality desired for organ printing

CHAPTER 8. CONCLUSIONS AND FUTURE DIRECTIONS

Surface modification on living cells is an exciting field of study with a vast array of applications. The potential clinical benefit in areas of drug delivery, immunoprotection and immunocamouflage, to physical protection from chemical and mechanical insults makes this an intensely studied field. Modifications are accomplished through numerous pathways such as covalent engraftment, electrostatic interactions, hydrophobic interactions, and antibody/antigen binding. Here, we explore the utility of a novel modification strategy that utilizes specific antigen binding for immobilization of a photoinitiator to subsequently encapsulate target cells in a thin hydrogel film. We explore applications in rare cell detection/isolation for cancer screening by protection against chemical lysis, as well as mechanical protection for tissue and organ printing through membrane reinforcement.

First, in Chapter 4 we establish a metric for cancer associated surface markers for potential targets in isolation. Isolation purity from a heterogeneous population using surface markers is largely dependent on relative expression of target markers. Quantification of antigen surface density relative to PBMCs gives us great insight into potential new targets, as well as highlights the shortcomings of current isolation strategies. Evaluation of the expression of commonly targeted markers on cancer cells relative to PBMCs indicates a lack of distinction, especially in the highly invasive cells lines. This indicates new and/or multiple markers will be necessary for the required selectivity of conventional and emerging sorting techniques. This information will greatly help current and future CTC isolation methods by revealing target markers that have the highest specificity relative to PBMCs.

For the greatest utility in a clinical setting, highly standardized procedures are most desired. Chapters 5 and 6 explore standardization of isolation through commercially available reagents and procedural parameters for scaling to relevant batch sizes. Previously, studies comparing xanthene photosensitizers have shown that eosin Y (EITC, in our study) greatly out performs fluorescein (FITC, in our study) in radical generation and polymerization ability. However, these studies were not done under the cytocompatible conditions required for hydrogel encapsulation. We showed that even though FITC has a greater spectral mismatch to our LED lamp than ETIC, significant film generation was achieved on both micro array slides and living cell surfaces. These findings suggest the plausible use of FITC which is a very common fluorophore and therefore, commercially sold conjugated to a range of biorecognition molecules. Commercial availability eliminates the need for a custom SA-EITC conjugate further standardizing our isolation system. We next sought to determine the key parameters associated with scaling the system to relevant batch sizes. Optical studies were performed on micro array slides for highly controlled experiments with quantitative information on film generation. Profilometry data of polymerizations using various conditions reveal that monomer fluid depth and incidence angle of radiation have large effects on film generation. This suggests that scaling processed volume through increased surface area and choosing a solution chamber that ensures minimizes presence of a meniscus is important in moving forward.

Finally, we look to the application of physical protection from mechanical stimuli of our protective hydrogel. Organ printing has potential to save thousands of lives every year by increasing the supply of viable organs for transplant. 3D bioprinting has already been used to print cells and tissues for *in vivo* use and is rapidly approaching organ printing.

High shear stress accompanies commercial extrusion printers which try to attain both the required resolution and throughput. Here, we demonstrated that encapsulation in thin hydrogel coatings has the ability to reinforce the cellular membrane preventing lysis in high shear fluid flow. Polymers possessing a modulus similar to that of PEGDA 700, 1000, and 2000, while possessing the same cytocompatibility of gelMA/3400 may possess the ability to protect cells form lysis while preserving high functionality. Further, we decoupled the parameters of rapid pressure drop and high shear forces associated with flow and determined that shear forces of flow are primarily responsible for the hindering of printed cell viability.

These studies along with previously published works in our lab demonstrate the versatility, feasibility, and high clinical impact that this technology possess in the field of cellular surface modifications for isolation, immunoprotection, and mechanical reinforcement. A future direction of this technology is in the degradation of the polymer coating. While the gelMA/3400 coating is biodegradable, efforts in a controlled degradation could have a high impact on clinical translation. Through the incorporation of photocleavable moieties, or enzymatically cleavable peptide sequences, coating removal could either be done so on-demand, or tune for give time scales or surrounding environments. As research has been done in photocleavable and enzymatically cleavable hydrogels, the unique polymerization process for our technology would allow for incorporation of such abilities with minimal change in the current system. ASL technology presents an exciting future with robust yet versatile applications.

Future directions within the application of mechanical protection include the incorporation of branched polymer systems. As it is known that the shorter PEG chains

have higher cytotoxicity and we have shown that polymer modulus plays a key role in protection from shear forces, incorporation of branched PEG acrylates is a potential solution. Larger molecular weight branched PEG molecules possess similar bioinert properties to that of linear PEG, but with a higher functionality for polymerization. Higher functionality will decrease the molecular weight between crosslinks increasing the modulus while limiting cytotoxicity associated with low molecular weights. Incorporation of these branched polymers could be the key to protection from shear lysis while maintaining high cell functionality.

REFERENCES

1. Goosen, M.F., et al., *Optimization of microencapsulation parameters: semipermeable microcapsules as a bioartificial pancreas.* Biotechnology and bioengineering, 1985. **27**(2): p. 146-150.
2. Chick, W.L., A.A. Like, and V. Lauris, *Beta cell culture on synthetic capillaries: an artificial endocrine pancreas.* Science, 1975. **187**(4179): p. 847-849.
3. Lim, F. and A.M. Sun, *Microencapsulated islets as bioartificial endocrine pancreas.* Science, 1980. **210**(4472): p. 908-910.
4. Wang, D., W.M. Toyofuku, and M.D. Scott, *The potential utility of methoxypoly (ethylene glycol)-mediated prevention of rhesus blood group antigen RhD recognition in transfusion medicine.* Biomaterials, 2012. **33**(10): p. 3002-3012.
5. Wang, D., et al., *Induction of immunotolerance via mPEG grafting to allogeneic leukocytes.* Biomaterials, 2011. **32**(35): p. 9494-9503.
6. Lim, F. and R.D. Moss, *Microencapsulation of living cells and tissues.* Journal of pharmaceutical sciences, 1981. **70**(4): p. 351-354.
7. Abbina, S., et al., *Surface Engineering for Cell-Based Therapies: Techniques for Manipulating Mammalian Cell Surfaces.* ACS Biomaterials Science & Engineering, 2017.
8. Chapanian, R., et al., *Therapeutic cells via functional modification: influence of molecular properties of polymer grafts on in vivo circulation, clearance, immunogenicity, and antigen protection.* Biomacromolecules, 2013. **14**(6): p. 2052-2062.
9. Lee, J., et al., *Cytoprotective silica coating of individual mammalian cells through bioinspired silicification.* Angewandte Chemie International Edition, 2014. **53**(31): p. 8056-8059.
10. Lee, J., et al., *Chemical sporulation and germination: cytoprotective nanocoating of individual mammalian cells with a degradable tannic acid–Fe III complex.* Nanoscale, 2015. **7**(45): p. 18918-18922.
11. Clafshenkel, W.P., et al., *The effect of covalently-attached ATRP-synthesized polymers on membrane stability and cytoprotection in human erythrocytes.* PloS one, 2016. **11**(6): p. e0157641.
12. Fliervoet, L.A. and E. Mastrobattista, *Drug delivery with living cells.* Advanced drug delivery reviews, 2016. **106**: p. 63-72.
13. Anselmo, A.C. and S. Mitragotri, *Cell-mediated delivery of nanoparticles: taking advantage of circulatory cells to target nanoparticles.* Journal of Controlled Release, 2014. **190**: p. 531-541.
14. Chambers, E. and S. Mitragotri, *Long circulating nanoparticles via adhesion on red blood cells: mechanism and extended circulation.* Experimental biology and medicine, 2007. **232**(7): p. 958-966.
15. Anselmo, A.C., et al., *Delivering nanoparticles to lungs while avoiding liver and spleen through adsorption on red blood cells.* ACS nano, 2013. **7**(12): p. 11129-11137.
16. Gribova, V., R. Auzely-Velty, and C. Picart, *Polyelectrolyte multilayer assemblies on materials surfaces: from cell adhesion to tissue engineering.* Chemistry of Materials, 2011. **24**(5): p. 854-869.

17. Myler, H., et al., *Anti-PEG antibody bioanalysis: a clinical case study with PEG-IFN-λ-1a and PEG-IFN-α2a in naive patients.* Bioanalysis, 2015. **7**(9): p. 1093-1106.
18. Batrakova, E.V., H.E. Gendelman, and A.V. Kabanov, *Cell-mediated drug delivery.* Expert opinion on drug delivery, 2011. **8**(4): p. 415-433.
19. Wu, P.-J., et al., *Hydrogel Patches on Live Cells through Surface-Mediated Polymerization.* Langmuir, 2017. **33**(27): p. 6778-6784.
20. Restifo, N.P., M.E. Dudley, and S.A. Rosenberg, *Adoptive immunotherapy for cancer: harnessing the T cell response.* Nature Reviews Immunology, 2012. **12**(4): p. 269.
21. Cahall, C.F., et al., *A Quantitative Perspective on Surface Marker Selection for the Isolation of Functional Tumor Cells.* Breast Cancer: Basic and Clinical Research, 2015. **9**(Suppl 1): p. 1.
22. Stevens, M.M. and J.H. George, *Exploring and engineering the cell surface interface.* Science, 2005. **310**(5751): p. 1135-1138.
23. Kalluri, R. and R.A. Weinberg, *The basics of epithelial-mesenchymal transition.* The Journal of clinical investigation, 2009. **119**(6): p. 1420-1428.
24. Hanahan, D. and R.A. Weinberg, *Hallmarks of cancer: the next generation.* Cell, 2011. **144**(5): p. 646-74.
25. Hayes, D.F. and J.B. Smerage, *Circulating tumor cells.* Progress in molecular biology and translational science, 2009. **95**: p. 95-112.
26. Wicha, M.S. and D.F. Hayes, *Circulating tumor cells: not all detected cells are bad and not all bad cells are detected.* Journal of Clinical Oncology, 2011. **29**(12): p. 1508-1511.
27. Gorges, T.M., et al., *Circulating tumour cells escape from EpCAM-based detection due to epithelial-to-mesenchymal transition.* BMC cancer, 2012. **12**(1): p. 178.
28. Bonnomet, A., et al., *A dynamic in vivo model of epithelial-to-mesenchymal transitions in circulating tumor cells and metastases of breast cancer.* Oncogene, 2012. **31**(33): p. 3741.
29. Cristofanilli, M., et al., *Circulating tumor cells: a novel prognostic factor for newly diagnosed metastatic breast cancer.* Journal of Clinical Oncology, 2005. **23**(7): p. 1420-1430.
30. de Bono, J.S., et al., *Circulating tumor cells predict survival benefit from treatment in metastatic castration-resistant prostate cancer.* Clinical Cancer Research, 2008. **14**(19): p. 6302-6309.
31. Cohen, S.J., et al., *Relationship of circulating tumor cells to tumor response, progression-free survival, and overall survival in patients with metastatic colorectal cancer.* Journal of clinical oncology, 2008. **26**(19): p. 3213-3221.
32. Allard, W.J., et al., *Tumor cells circulate in the peripheral blood of all major carcinomas but not in healthy subjects or patients with nonmalignant diseases.* Clinical Cancer Research, 2004. **10**(20): p. 6897-6904.
33. Romero, G., et al., *Protective Polymer Coatings for High-Throughput, High-Purity Cellular Isolation.* ACS Applied Materials & Interfaces, 2015. **7**(32): p. 17598-17602.

34. Anderson, S.B., et al., *The performance of human mesenchymal stem cells encapsulated in cell-degradable polymer-peptide hydrogels.* Biomaterials, 2011. **32**(14): p. 3564-3574.
35. Nicodemus, G.D. and S.J. Bryant, *Cell encapsulation in biodegradable hydrogels for tissue engineering applications.* Tissue Engineering Part B: Reviews, 2008. **14**(2): p. 149-165.
36. Drury, J.L. and D.J. Mooney, *Hydrogels for tissue engineering: scaffold design variables and applications.* Biomaterials, 2003. **24**(24): p. 4337-4351.
37. Cadet, J., E. Sage, and T. Douki, *Ultraviolet radiation-mediated damage to cellular DNA.* Mutation Research/Fundamental and Molecular Mechanisms of Mutagenesis, 2005. **571**(1): p. 3-17.
38. Encinas, M., et al., *Xanthene dyes/amine as photoinitiators of radical polymerization: a comparative and photochemical study in aqueous medium.* Polymer, 2009. **50**(13): p. 2762-2767.
39. Avens, H.J. and C.N. Bowman, *Mechanism of cyclic dye regeneration during eosin-sensitized photoinitiation in the presence of polymerization inhibitors.* Journal of Polymer Science Part A: Polymer Chemistry, 2009. **47**(22): p. 6083-6094.
40. Kızılel, S., V.H. Pérez-Luna, and F. Teymour, *Mathematical model for Surface-Initiated photopolymerization of poly (ethylene glycol) diacrylate.* Macromolecular theory and simulations, 2006. **15**(9): p. 686-700.
41. Wong, J., et al., *A quantitative analysis of peroxy-mediated cyclic regeneration of eosin under oxygen-rich photopolymerization conditions.* Polymer, 2015. **69**: p. 169-177.
42. Yagci, Y., S. Jockusch, and N.J. Turro, *Photoinitiated polymerization: advances, challenges, and opportunities.* Macromolecules, 2010. **43**(15): p. 6245-6260.
43. Avens, H.J. and C.N. Bowman, *Development of fluorescent polymerization-based signal amplification for sensitive and non-enzymatic biodetection in antibody microarrays.* Acta biomaterialia, 2010. **6**(1): p. 83-89.
44. Avens, H.J., et al., *Sensitive Immunofluorescent Staining of Cells via Generation of Fluorescent Nanoscale Polymer Films in Response to Biorecognition.* Journal of Histochemistry & Cytochemistry, 2011. **59**(1): p. 76-87.
45. Avens, H.J., T.J. Randle, and C.N. Bowman, *Polymerization behavior and polymer properties of eosin-mediated surface modification reactions.* Polymer, 2008. **49**(22): p. 4762-4768.
46. Mavili, M.E., et al., *Use of three-dimensional medical modeling methods for precise planning of orthognathic surgery.* Journal of Craniofacial Surgery, 2007. **18**(4): p. 740-747.
47. Knox, K., et al., *Rapid prototyping to create vascular replicas from CT scan data: making tools to teach, rehearse, and choose treatment strategies.* Catheterization and cardiovascular interventions, 2005. **65**(1): p. 47-53.
48. Murphy, S.V. and A. Atala, *3D bioprinting of tissues and organs.* Nature biotechnology, 2014. **32**(8): p. 773.
49. Bajaj, P., et al., *3D biofabrication strategies for tissue engineering and regenerative medicine.* Annual review of biomedical engineering, 2014. **16**: p. 247-276.

50. Zorlutuna, P., et al., *Microfabricated biomaterials for engineering 3D tissues.* Advanced materials, 2012. **24**(14): p. 1782-1804.
51. Hockaday, L., et al., *Rapid 3D printing of anatomically accurate and mechanically heterogeneous aortic valve hydrogel scaffolds.* Biofabrication, 2012. **4**(3): p. 035005.
52. Mannoor, M.S., et al., *3D printed bionic ears.* Nano letters, 2013. **13**(6): p. 2634-2639.
53. Park, J.Y., et al., *Development of a 3D cell printed structure as an alternative to autologs cartilage for auricular reconstruction.* Journal of Biomedical Materials Research Part B: Applied Biomaterials, 2017. **105**(5): p. 1016-1028.
54. Gaetani, R., et al., *Cardiac tissue engineering using tissue printing technology and human cardiac progenitor cells.* Biomaterials, 2012. **33**(6): p. 1782-1790.
55. Bhise, N.S., et al., *Organ-on-a-chip platforms for studying drug delivery systems.* Journal of Controlled Release, 2014. **190**: p. 82-93.
56. Wagner, I., et al., *A dynamic multi-organ-chip for long-term cultivation and substance testing proven by 3D human liver and skin tissue co-culture.* Lab on a Chip, 2013. **13**(18): p. 3538-3547.
57. D'Urso, P.S., et al., *Custom cranioplasty using stereolithography and acrylic.* British Journal of Plastic Surgery, 2000. **53**(3): p. 200-204.
58. Singare, S., et al., *Individually prefabricated prosthesis for maxilla reconstruction.* Journal of Prosthodontics, 2008. **17**(2): p. 135-140.
59. Mandrycky, C., et al., *3D bioprinting for engineering complex tissues.* Biotechnology advances, 2016. **34**(4): p. 422-434.
60. Billiet, T., et al., *The 3D printing of gelatin methacrylamide cell-laden tissue-engineered constructs with high cell viability.* Biomaterials, 2014. **35**(1): p. 49-62.
61. Zhao, Y., et al., *Three-dimensional printing of Hela cells for cervical tumor model in vitro.* Biofabrication, 2014. **6**(3): p. 035001.
62. Chung, J.H., et al., *Bio-ink properties and printability for extrusion printing living cells.* Biomaterials Science, 2013. **1**(7): p. 763-773.
63. Zhu, K., et al., *Gold nanocomposite bioink for printing 3D cardiac constructs.* Advanced functional materials, 2017. **27**(12): p. 1605352.
64. Blaeser, A., et al., *Controlling shear stress in 3D bioprinting is a key factor to balance printing resolution and stem cell integrity.* Advanced healthcare materials, 2016. **5**(3): p. 326-333.
65. Colosi, C., et al., *Microfluidic bioprinting of heterogeneous 3D tissue constructs using low-viscosity bioink.* Advanced Materials, 2016. **28**(4): p. 677-684.
66. Hansen, R.R., H.D. Sikes, and C.N. Bowman, *Visual detection of labeled oligonucleotides using visible-light-polymerization-based amplification.* Biomacromolecules, 2007. **9**(1): p. 355-362.
67. Massagué, J. and A.C. Obenauf, *Metastatic colonization by circulating tumour cells.* Nature, 2016. **529**(7586): p. 298.
68. Ashworth, T., *A case of cancer in which cells similar to those in the tumours were seen in the blood after death.* Aust Med J, 1869. **14**(3): p. 146-149.
69. Smith, R.A., et al., *Cancer screening in the United States, 2017: a review of current American Cancer Society guidelines and current issues in cancer screening.* CA: a cancer journal for clinicians, 2017. **67**(2): p. 100-121.

70. Siegel, R., C. DeSantis, and A. Jemal, *Colorectal cancer statistics, 2014.* CA: a cancer journal for clinicians, 2014. **64**(2): p. 104-117.
71. Jones, S., et al., *Comparative lesion sequencing provides insights into tumor evolution.* Proceedings of the National Academy of Sciences, 2008. **105**(11): p. 4283-4288.
72. Kalluri, R. and R.A. Weinberg, *The basics of epithelial-mesenchytnal transition (vol 119, pg 1420, 2009).* Journal of Clinical Investigation, 2010. **120**(5): p. 1786-1786.
73. Aktas, B., et al., *Stem cell and epithelial-mesenchymal transition markers are frequently overexpressed in circulating tumor cells of metastatic breast cancer patients.* Breast cancer res, 2009. **11**(4): p. R46.
74. Bonnomet, A., et al., *Epithelial-to-mesenchymal transitions and circulating tumor cells.* Journal of mammary gland biology and neoplasia, 2010. **15**(2): p. 261-273.
75. Bhagat, A.A.S., et al., *Microfluidics for cell separation.* Medical & biological engineering & computing, 2010. **48**(10): p. 999-1014.
76. Nagrath, S., et al., *Isolation of rare circulating tumour cells in cancer patients by microchip technology.* Nature, 2007. **450**(7173): p. 1235-1239.
77. Choi, S., J.M. Karp, and R. Karnik, *Cell sorting by deterministic cell rolling.* Lab on a Chip, 2012. **12**(8): p. 1427-1430.
78. Miltenyi, S., et al., *High gradient magnetic cell separation with MACS.* Cytometry: The Journal of the International Society for Analytical Cytology, 1990. **11**(2): p. 231-238.
79. Owen, C.S. and N.L. Sykes, *Magnetic labeling and cell sorting.* Journal of immunological methods, 1984. **73**(1): p. 41-48.
80. Königsberg, R., et al., *Detection of EpCAM positive and negative circulating tumor cells in metastatic breast cancer patients.* Acta oncologica, 2011. **50**(5): p. 700-710.
81. Osta, W.A., et al., *EpCAM is overexpressed in breast cancer and is a potential target for breast cancer gene therapy.* Cancer research, 2004. **64**(16): p. 5818-5824.
82. Jain, J., G. Veggiani, and M. Howarth, *Cholesterol loading and ultrastable protein interactions determine the level of tumor marker required for optimal isolation of cancer cells.* Cancer research, 2013. **73**(7): p. 2310-2321.
83. Eccles, S.A., *The role of c-erbB-2/HER2/neu in breast cancer progression and metastasis.* Journal of mammary gland biology and neoplasia, 2001. **6**(4): p. 393-406.
84. Deroo, B.J. and K.S. Korach, *Estrogen receptors and human disease.* The Journal of clinical investigation, 2006. **116**(3): p. 561.
85. Perl, A.-K., et al., *A causal role for E-cadherin in the transition from adenoma to carcinoma.* Nature, 1998. **392**(6672): p. 190-193.
86. Hajra, K.M., X. Ji, and E.R. Fearon, *Extinction of E-cadherin expression in breast cancer via a dominant repression pathway acting on proximal promoter elements.* Oncogene, 1999. **18**(51): p. 7274-7279.
87. Hazan, R.B., et al., *Exogenous expression of N-cadherin in breast cancer cells induces cell migration, invasion, and metastasis.* The Journal of cell biology, 2000. **148**(4): p. 779-790.

88. Yilmaz, M. and G. Christofori, *EMT, the cytoskeleton, and cancer cell invasion.* Cancer and Metastasis Reviews, 2009. **28**(1-2): p. 15-33.
89. Afify, A., P. Purnell, and L. Nguyen, *Role of CD44s and CD44v6 on human breast cancer cell adhesion, migration, and invasion.* Experimental and molecular pathology, 2009. **86**(2): p. 95-100.
90. Toole, B.P., *Hyaluronan promotes the malignant phenotype.* Glycobiology, 2002. **12**(3): p. 37R-42R.
91. Jin, H. and J. Varner, *Integrins: roles in cancer development and as treatment targets.* British Journal of Cancer, 2004. **90**(3): p. 561-565.
92. Hood, J.D. and D.A. Cheresh, *Role of integrins in cell invasion and migration.* Nature Reviews Cancer, 2002. **2**(2): p. 91.
93. Beer, A.J., et al., *Patterns of {alpha} v {beta} 3 expression in primary and metastatic human breast cancer as shown by 18F-galacto-RGD PET.* Journal of Nuclear Medicine, 2008. **49**(2): p. 255.
94. O'hanlon, D., et al., *Soluble adhesion molecules (E-selectin, ICAM-1 and VCAM-1) in breast carcinoma.* European Journal of Cancer, 2002. **38**(17): p. 2252-2257.
95. Budinsky, A.C., et al., *Decreased expression of ICAM-1 and its induction by tumor necrosis factor on breast-cancer cells in vitro.* International journal of cancer, 1997. **71**(6): p. 1086-1090.
96. Liu, S., et al., *Expression of intercellular adhesion molecule 1 by hepatocellular carcinoma stem cells and circulating tumor cells.* Gastroenterology, 2013. **144**(5): p. 1031-1041. e10.
97. Bhargava, R., et al., *EGFR gene amplification in breast cancer: correlation with epidermal growth factor receptor mRNA and protein expression and HER-2 status and absence of EGFR-activating mutations.* Modern pathology, 2005. **18**(8): p. 1027-1033.
98. Harris, A.L., et al., *Epidermal growth factor receptors in breast cancer: association with early relapse and death, poor response to hormones and interactions with neu.* Journal of steroid biochemistry, 1989. **34**(1): p. 123-131.
99. Chavez, K.J., S.V. Garimella, and S. Lipkowitz, *Triple negative breast cancer cell lines: one tool in the search for better treatment of triple negative breast cancer.* Breast disease, 2010. **32**(1): p. 35-48.
100. Holliday, D.L. and V. Speirs, *Choosing the right cell line for breast cancer research.*
101. Maheswaran, S., et al., *Detection of mutations in EGFR in circulating lung-cancer cells.* New England Journal of Medicine, 2008. **359**(4): p. 366-377.
102. Yang, J., et al., *Dielectric properties of human leukocyte subpopulations determined by electrorotation as a cell separation criterion.* Biophysical journal, 1999. **76**(6): p. 3307-3314.
103. Evans, E. and A. Yeung, *Apparent viscosity and cortical tension of blood granulocytes determined by micropipet aspiration.* Biophysical journal, 1989. **56**(1): p. 151.
104. Yu, M., et al., *Circulating breast tumor cells exhibit dynamic changes in epithelial and mesenchymal composition.* Science, 2013. **339**(6119): p. 580-584.

105. Lecharpentier, A., et al., *Detection of circulating tumour cells with a hybrid (epithelial/mesenchymal) phenotype in patients with metastatic non-small cell lung cancer.* British Journal of Cancer, 2011. **105**(9): p. 1338-1341.
106. McCabe, A., et al., *Automated quantitative analysis (AQUA) of in situ protein expression, antibody concentration, and prognosis.* Journal of the National Cancer Institute, 2005. **97**(24): p. 1808-1815.
107. Livasy, C.A., et al., *Phenotypic evaluation of the basal-like subtype of invasive breast carcinoma.* Modern Pathology, 2006. **19**(2): p. 264-271.
108. Yang, J. and R.A. Weinberg, *Epithelial-mesenchymal transition: at the crossroads of development and tumor metastasis.* Developmental cell, 2008. **14**(6): p. 818-829.
109. Ali, S. and R.C. Coombes, *Estrogen receptor alpha in human breast cancer: occurrence and significance.* Journal of mammary gland biology and neoplasia, 2000. **5**(3): p. 271-281.
110. Thiery, J.P. and C.T. Lim, *Tumor dissemination: an EMT affair.* Cancer cell, 2013. **23**(3): p. 272-273.
111. Kawata, M., et al., *TGF-β-induced epithelial-mesenchymal transition of A549 lung adenocarcinoma cells is enhanced by pro-inflammatory cytokines derived from RAW 264.7 macrophage cells.* Journal of biochemistry, 2012. **151**(2): p. 205-216.
112. Liu, X., *Inflammatory cytokines augments TGF-β1-induced epithelial-mesenchymal transition in A549 cells by up-regulating TβR-I.* Cell motility and the cytoskeleton, 2008. **65**(12): p. 935-944.
113. Sun, J.-J., et al., *Invasion and metastasis of liver cancer: expression of intercellular adhesion molecule 1.* Journal of cancer research and clinical oncology, 1999. **125**(1): p. 28-34.
114. Sununliganon, L. and W. Singhatanadgit, *Highly osteogenic PDL stem cell clones specifically express elevated levels of ICAM1, ITGB1 and TERT.* Cytotechnology, 2012. **64**(1): p. 53-63.
115. Strakova, Z., et al., *Multipotent properties of myofibroblast cells derived from human placenta.* Cell and tissue research, 2008. **332**(3): p. 479-488.
116. Cruise, G.M., et al., *A sensitivity study of the key parameters in the interfacial photopolymerization of poly(ethylene glycol) diacrylate upon porcine islets.* Biotechnology and Bioengineering, 1998. **57**(6): p. 655-665.
117. Kaastrup, K. and H. Sikes, *Investigation of dendrimers functionalized with eosin as macrophotoinitiators for polymerization-based signal amplification reactions.* RSC Advances, 2015. **5**(20): p. 15652-15659.
118. Bahney, C., et al., *Visible light photoinitiation of mesenchymal stem cell-laden bioresponsive hydrogels.* Eur Cell Mater, 2011. **22**: p. 43-55.
119. Avens, H.J. and C.N. Bowman, *Mechanism of Cyclic Dye Regeneration During Eosin-Sensitized Photoinitiation in the Presence of Polymerization Inhibitors.* Journal of Polymer Science Part a-Polymer Chemistry, 2009. **47**(22): p. 6083-6094.
120. Sikes, H.D., et al., *Using polymeric materials to generate an amplified response to molecular recognition events.* Nature Materials, 2008. **7**(1): p. 52-56.

121. Hansen, R.R., et al., *Quantitative evaluation of oligonucleotide surface concentrations using polymerization-based amplification.* Analytical and Bioanalytical Chemistry, 2008. **392**(1-2): p. 167-175.
122. Hansen, R.R., L.M. Johnson, and C.N. Bowman, *Visual, base-specific detection of nucleic acid hybridization using polymerization-based amplification.* Analytical Biochemistry, 2009. **386**(2): p. 285-287.
123. Johnson, L.M., et al., *Characterization of the Assaying Methods in Polymerization-Based Amplification of Surface Biomarkers.* Australian Journal of Chemistry, 2009. **62**(8): p. 877-884.
124. Lilly, J.L., et al., *Characterization of molecular transport in ultrathin hydrogel coatings for cellular immunoprotection.* Biomacromolecules, 2015. **16**(2): p. 541-549.
125. Cruise, G.M., et al., *Poly(ethylene glycol) based encapsulation of islets of Langerhans.* Cell Transplantation, 1996. **5**(5 SUPPL. 2): p. 52-52.
126. Heather J. Avens, T.J.R., Christopher N. Bowman, *Polymerization behavior and polymer properties of eosin-mediated surface modification reactions.* Polymer, 2008. **49**: p. 4762-4768.
127. Kizilel, S., V.H. Perez-Luna, and F. Teymour, *Photopolymerization of poly(ethylene glycol) diacrylate on eosin-functionalized surfaces.* Langmuir, 2004. **20**(20): p. 8652-8658.
128. Sawhney, A.S., C.P. Pathak, and J.A. Hubbell, *Interfacial Photopolymerization of Poly(ethylene glycol)-Based Hydrogels Upon Alginate Poly(L-Lysine) Microcapsules for Enhanced Biocompatibility.* Biomaterials, 1993. **14**(13): p. 1008-1016.
129. Cruise, G.M., D.S. Scharp, and J.A. Hubbell, *Characterization of permeability and network structure of interfacially photopolymerized poly(ethylene glycol) diacrylate hydrogels.* Biomaterials, 1998. **19**(14): p. 1287-1294.
130. Lee, J.K., B.W. Heimer, and H.D. Sikes, *Systematic study of fluorescein-functionalized macrophotoinitiators for colorimetric bioassays.* Biomacromolecules, 2012. **13**(4): p. 1136-1143.
131. Liu, G., et al., *Cytotoxicity study of polyethylene glycol derivatives.* RSC Advances, 2017. **7**(30): p. 18252-18259.
132. Lilly, J.L. and B.J. Berron, *The Role of Surface Receptor Density in Surface-Initiated Polymerizations for Cancer Cell Isolation.* Langmuir, 2016. **32**(22): p. 5681-5689.
133. Piran, U. and W.J. Riordan, *Dissociation rate constant of the biotin-streptavidin complex.* Journal of immunological methods, 1990. **133**(1): p. 141-143.
134. Lilly, J.L. and B.J. Berron, *The Role of Surface Receptor Density in Surface-Initiated Polymerizations for Cancer Cell Isolation.* Langmuir, 2016. **32**(22): p. 5681-9.
135. Lilly, J.L., et al., *Characterization of Molecular Transport in Ultrathin Hydrogel Coatings for Cellular Immunoprotection.* Biomacromolecules, 2015.
136. Shih, H. and C.-C. Lin, *Visible-Light-Mediated Thiol-Ene Hydrogelation Using Eosin-Y as the Only Photoinitiator.* Macromolecular Rapid Communications, 2013. **34**(3): p. 269-273.

137. Siegel, R.L., K.D. Miller, and A. Jemal, *Cancer statistics, 2017.* CA: a cancer journal for clinicians, 2017. **67**(1): p. 7-30.
138. Myers, E.R., et al., *Benefits and harms of breast cancer screening: a systematic review.* Jama, 2015. **314**(15): p. 1615-1634.
139. Singh, A. and J. Settleman, *EMT, cancer stem cells and drug resistance: an emerging axis of evil in the war on cancer.* Oncogene, 2010. **29**(34): p. 4741.
140. Miller, M.C., G.V. Doyle, and L.W. Terstappen, *Significance of circulating tumor cells detected by the CellSearch system in patients with metastatic breast colorectal and prostate cancer.* Journal of oncology, 2010. **2010**.
141. W. R. Kim, J.R.L., J. M. Smith, D. P. Schladt, M. A. Skeans, A. M. Harper, J. L. Wainright, J. J. Snyder, A. K. Israni, B. L. Kasiske., *OPTN/SRTR Annual Data Report 2016.* American Journal of Transplantation, 2018. **18**(S1): p. 1-503.
142. Abouna, G.M. *Organ shortage crisis: problems and possible solutions*. in *Transplantation proceedings*. 2008. Elsevier.
143. Rengier, F., et al., *3D printing based on imaging data: review of medical applications.* International journal of computer assisted radiology and surgery, 2010. **5**(4): p. 335-341.
144. Ozbolat, I.T. and Y. Yu, *Bioprinting toward organ fabrication: challenges and future trends.* IEEE Transactions on Biomedical Engineering, 2013. **60**(3): p. 691-699.
145. KHATIWALA, C., et al., *3D cell bioprinting for regenerative medicine research and therapies.* Gene Therapy and Regulation, 2012. **7**(01): p. 1230004.
146. Shim, J.-H., et al., *Bioprinting of a mechanically enhanced three-dimensional dual cell-laden construct for osteochondral tissue engineering using a multi-head tissue/organ building system.* Journal of Micromechanics and Microengineering, 2012. **22**(8): p. 085014.
147. Lee, J.-S., et al., *3D printing of composite tissue with complex shape applied to ear regeneration.* Biofabrication, 2014. **6**(2): p. 024103.
148. Chang, R., J. Nam, and W. Sun, *Direct cell writing of 3D microorgan for in vitro pharmacokinetic model.* Tissue Engineering Part C: Methods, 2008. **14**(2): p. 157-166.
149. Nair, K., et al., *Characterization of cell viability during bioprinting processes.* Biotechnology Journal: Healthcare Nutrition Technology, 2009. **4**(8): p. 1168-1177.
150. Augenstein, D., A. Sinskey, and D. Wang, *Effect of shear on the death of two strains of mammalian tissue cells.* Biotechnology and bioengineering, 1971. **13**(3): p. 409-418.
151. Kong, H.J., M.K. Smith, and D.J. Mooney, *Designing alginate hydrogels to maintain viability of immobilized cells.* Biomaterials, 2003. **24**(22): p. 4023-4029.
152. Welty, J.R., et al., *Fundamentals of momentum, heat, and mass transfer*. 2009: John Wiley & Sons.
153. Chen, C.R. and G.I. Makhatadze, *Molecular determinant of the effects of hydrostatic pressure on protein folding stability.* Nature communications, 2017. **8**: p. 14561.

154. Hillson, N., J.N. Onuchic, and A.E. García, *Pressure-induced protein-folding/unfolding kinetics.* Proceedings of the National Academy of Sciences, 1999. **96**(26): p. 14848-14853.
155. Moonschi, F.H., et al., *Mammalian Cell-derived Vesicles for the Isolation of Organelle Specific Transmembrane Proteins to Conduct Single Molecule Studies.* The Journal of Biological Chemistry, 2017.

CALVIN FRANK CAHALL VITA

EDUCATION

B. S. Chemistry, and Chemical Physics, Centre College Danville, KY 2009-2013

Minor: Physics

EXPERIENCE

University of Kentucky, Lexington, KY
Graduate Research Assistant, Aug 2014 – Dec 2018.

Patheon Pharmaceuticals Inc., Cincinnati, OH.
Associate Analytical Chemist, Dec 2013 - Mar 2014.

HONORS

Halcomb Fellowship in Engineering and Medecine, University of Kentucky 2016-2017, 2017-2018

Gill Engineering Excellence Fellowship, University of Kentucky 2015-2016.

Graduate Student Academic Year Fellowship, University of Kentucky 2014-2015.

Founders Scholarship, Centre College 2009-2013.

PUBLICATIONS

Cahall, C.F., et al., *A Quantitative Perspective on Surface Marker Selection for the Isolation of Functional Tumor Cells.* Breast Cancer: Basic and Clinical Research, 2015. **9**(Suppl 1): p. 1

Lilly, J.L., Anuhya Gottipati, Calvin F. Cahall, Mohamed Agoub, Brad J. Berron Comparison *of eosin and fluorescein conjugates for the photoinitiation of cell-compatible polymer coatings.* PloS one, 2018. **13**(1): p. e0190880.